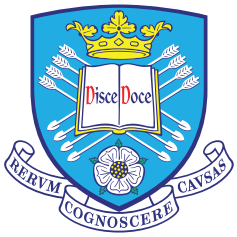

The University Of Sheffield.

III-V Semiconductor Quantum Nano-Photonic Circuits

Christopher Bentham

Submitted for the degree of Doctor of Philosophy

Department of Physics and Astronomy
University of Sheffield

September 2016

Abstract

This thesis describes the optical spectroscopic measurements of III-V nano-photonic circuit elements with integrated self-assembled quantum dot single-photon sources, as a step towards achieving an on-chip quantum optical circuit.

An electrically controllable optical router consisting of an embedded quantum dot within a photonic crystal cavity which is selectively coupled to separate waveguides is presented. By tuning the voltage, the quantum dot emission can be directed into either waveguide. This is experimentally demonstrated with spatially resolved microphotoluminescence measurements.

An electrically driven single-photon source monolithically integrated with nano-photonic circuitry is investigated. In this device, electroluminescent emission from a single quantum dot is channelled through a suspended nanobeam waveguide. The emission is shown to be highly coherent with coherence properties which are sufficient to observe non-classical interference. Correlation and cross-correlation measurements are used to confirm the single-photon nature of the source and the propagation of the single photons.

A detailed investigation of the on-chip two-photon interference of two dissimilar sources is presented. Photons emitted by a quantum dot embedded in one arm of a directional coupler are combined with photons originating from an external laser. The occurrence of Hong-Ou-Mandel interference is confirmed with cross-correlation measurements.

Acknowledgements

It has been a privilege to be able to study as part of the Low Dimensional Structures and Devices group at the University of Sheffield. I have been fortunate enough to study alongside many talented individuals. Although some of you I have not been fortunate enough to work with, your contributions to making the office and Friday nights interesting is much appreciated.

I would like to thank my supervisor Luke Wilson, Maurice Skolnick and Igor Itskevich for the help and guidance they have provided over the years. I would also like to thank Nikola Prtljaga and John O'Hara who contributed substantially to the work in this thesis.

Finally, I thank my friends and family for all their support.

(Also, thank you tea.)

Publications

Aspects of the work presented in this thesis have appeared in or at the following journals and conferences.

Articles

C. Bentham, D. Hallett, N. Prtljaga, B. Royall, D. Vaitiekus, R. J. Coles, E. Clarke, A. M. Fox, M. S. Skolnick, I. E. Itskevich and L. R. Wilson, "Single-photon electroluminescence for on-chip quantum networks", Applied Physics Letters **109**, 161101 (2016).

N. Prtljaga, **C. Bentham**, J. O'Hara, B. Royall, E. Clarke, L. R. Wilson, M. S. Skolnick and A. M. Fox, "On-chip interference of single photons from an embedded quantum dot and an external laser", Applied Physics Letters **108**, 251101 (2016).

C. Bentham, I. E. Itskevich, R. J. Coles, B. Royall, E. Clarke, J. O'Hara, N. Prtljaga, a. M. Fox, M. S. Skolnick and L. R. Wilson, "On-chip electrically controlled routing of photons from a single quantum dot", Applied Physics Letters **106**, 221101 (2015).

A. Brash, L. Martins, R. Manson, F. Liu, R. Coles, **C. Bentham**, B. Royall, L. R. Wilson, S. Hughes, M. Skolnick and A. Fox, "Enhanced rabi oscillation and exciton-phonon coupling in a qd-cavity system", In preparation, 2016.

L. Martins, A. Brash, F. Liu, **C. Bentham**, R. Coles, B. Royall, L. R. Wilson, M. Skolnick and A. Fox, "Ultrafast optical control of light scattering in a weakly coupled qd-cavity system", In preparation, 2016.

Conferences

C. Bentham, D. Hallett, N. Prtljaga, R. J. Coles, B. Royall, D. Vaitiekus, E. Clarke, A. M. Fox, L. R. Wilson, M. S. Skolnick and I. E. Itskevich, "Single-photon electroluminescence for on-chip quantum networks", Poster Presentation, ICPS 33, 2016.

J. O'Hara, N. Prtljaga, **C. Bentham**, B. Royall, E. Clarke, L. R. Wilson, M. S. Skolnick and A. M. Fox, "On-chip interference of single photons from an embedded quantum dot and a laser", Oral Presentation, ICPS 33, 2016.

J. O'Hara, N. Prtljaga, **C. Bentham**, B. Royall, E. Clarke, L. R. Wilson, M. S. Skolnick and A. M. Fox, "On-chip interference of single photons from an embedded quantum dot and a laser", Oral Presentation, PECS XII, 2016.

J. P. Bradley, I. E. Itskevich, B. Royall, **C. Bentham**, N. Prtljaga, E. Clarke, A. M. Fox, M. S. Skolnick and L. R. Wilson, "Stark tuning of single quantum dots in an on-chip beam splitter device", Oral Presentation, UK Semiconductors, 2015.

C. Bentham, I. E. Itskevich, R. J. Coles, N. Prtljaga, B. Royall, M. S. Skolnick and L. R. Wilson, "Electrical Control of On-Chip Single-Photon Routing", Oral Presentation, ICPS 32, 2014.

C. Bentham, I. E. Itskevich, R. J. Coles, B. Royall, E. Clarke, J. O'Hara, N. Prtljaga, A. M. Fox, M. S. Skolnick and L. R. Wilson, "Electrically Controllable On-Chip Single-Photon Router", Oral Presentation, UK Semiconductors, 2014.

Contents

Acronyms

CAD Computer aided design

CCD Charge-coupled device

CMOS Complementary metal-oxide-semiconductor

cQED Cavity quantum electrodynamics

CW Continuous wave

DMM Digital multimeter

EBL Electron beam lithography

EL Electroluminescence

FDTD Finite-difference time-domain

FOV Field of view

FPI Fabry-Perot Interferometer

FSS Fine structure splitting

FWHM Full width at half maximum

HAL Hardware abstraction layer

HBT Hanbury Brown and Twiss

HMDS Hexamethyldisilane

HOM Hong-Ou-Mandel

ICP Inductively coupled plasma

IV Current-voltage

KF Klein flange

LCC Leadless chip carrier

LDSD Low Dimensional Structures & Devices

LO Longitudinal optical

LOQC Linear optical quantum computing

MBE Molecular beam epitaxy

MEMS Microelectromechanical systems

MOVPE Metalorganic vapour phase epitaxy

NA Numerical aperture

PCB Printed circuit board

PhC Photonic crystal

PhCC Photonic crystal cavity

PL Photoluminescence

PLE Photoluminescence excitation

QCSE Quantum-confined Stark effect

QD Quantum dot

QIP Quantum information processing

RF Radio frequency

RTA Rapid thermal anneal

SAQD Self-assembled quantum dot

SEM Scanning electron microscope

SNR Signal-to-noise ratio

SNSPD Superconducting nanowire single photon detector

SPAD Single-photon avalanche diode

SPC Single photon counter

SPCM Single photon counting module

TCSPC Time-correlated single photon counting

TE Transverse-electric

μPL Micro-photoluminescence

Chapter 1

Introduction and Motivation

The quantum computer was first proposed by Richard Feynman in 1982 as a method of simulating quantum mechanical systems efficiently[1]. Since then the idea of a quantum computer has been reinforced with the development of quantum algorithms able to solve certain problems exponentially faster than a classical computer with the most well known being Shor's algorithm for prime factorisation[2] and Grover's algorithm for searching unordered lists[3].

Steps towards a physical implementation of a universal quantum computer have been made with several architectures showing promise[4–8]. Of these, encoding information into the polarisation, time bin or path of single photons has shown great promise thanks to photons being easy to manipulate and free from the decoherence issues that plague other systems[9]. It was originally assumed that an optical implementation of a quantum computer would require strong optical non-linearities to realise even the simplest logic elements[9]. In 2001 however it was shown that a quantum computer can be built with linear optics, only requiring single photons, beamsplitters, phase shifters, and single photon detectors[10]. This scheme is commonly referred to as linear optical quantum computing (LOQC). Experimental demonstrations of LOQC are currently limited to performing operations with an external single photon source connected to either bulk optics[11, 12] or waveguide circuits[13, 14]. As devices scale to larger photon numbers, full integration of the single-photon source and circuitry is required[15].

Alternative easier to implement non-universal quantum computing schemes based upon boson sampling have also been suggested and demonstrated[16–19]. Currently this method appears to only be faster than classical computers for the

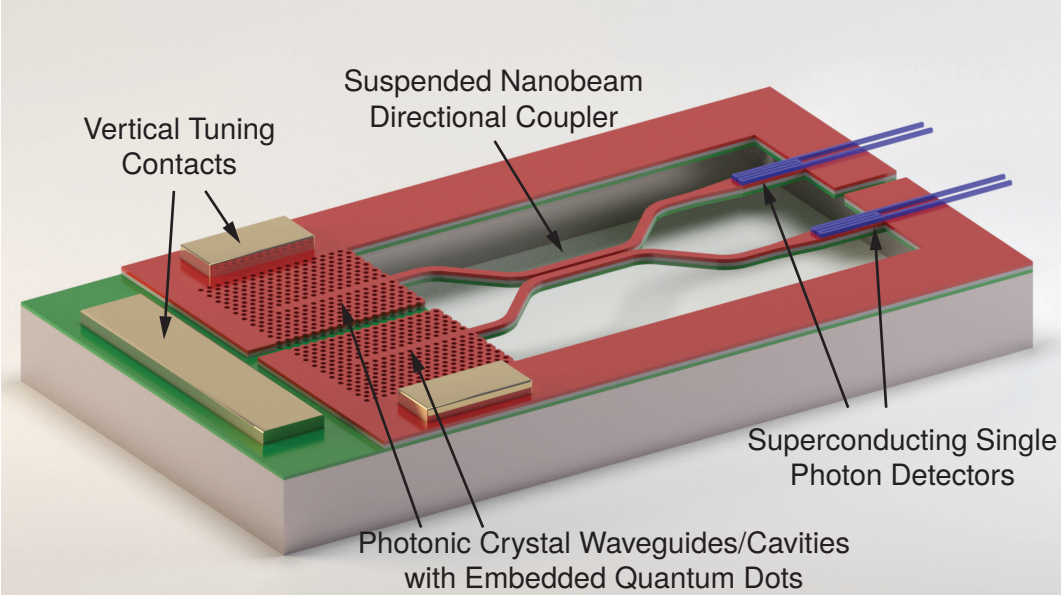

Figure 1.1 – Proposed design of a III-V semiconductor on-chip circuit in which two single-photons are generated, interfered and then detected. The p-type, n-type and intrinsic layers are shown in red, green and grey respectively. Quantum dots (QDs) located in each arm are used as single-photon sources. A break in the p-type layer allows independent electrical tuning via the quantum-confined Stark effect.

boson sampling problem[20].

A proposed demonstration circuit is illustrated in Figure 1.1 which is the current focus of research within the Low Dimensional Structures & Devices (LDSD) group at the University of Sheffield. If realised, the device will be the first demonstration of a Hong-Ou-Mandel (HOM) interferometer[21] with the generation of two photons, their interference and detection of the resulting state occurring entirely on-chip. The device consists of directional coupler with a self-assembled quantum dot (SAQD) single-photon source embedded within each arm. The SAQD sources are located within a photonic crystal to utilise slow light effects to provide Purcell enhancement of the emission. The p-i-n structure and etched notches allow a vertical electric field to be applied to each SAQD independently to tune their emission via the quantum-confined Stark effect (QCSE). Also on the chip are two superconducting nanowire single photon detectors (SNSPDs) to detect the resulting photon state from the interferometer.

1.1 Outline and Scope of this Thesis

This thesis focuses on the steps towards achieving the goal of a fully integrated quantum optical circuit. This includes the detailed study of electrically driven single-photon sources, integrated interferometers, and photon routers.

In Chapter 2 the basic concepts and background information on quantum dots, cavity quantum electrodynamics, photonic crystals, and the HOM effect are presented.

Chapter 3 describes the computational and experimental methods used to design, produce, and measure the devices presented in the subsequent chapters.

Chapter 4 presents the on-chip electrically controlled routing of photons emitted from a single quantum dot. A quantum dot is located within a H1 cavity with two W1 waveguides. The emission from a single quantum dot is electrically tuned across the cavity modes. By tuning voltage the emission is shown to be selectively directed into either waveguide, enabling voltage controlled optical routing. This proof of concept device provides the basis for scalable integrated single-photon routers.

Chapter 5 demonstrates an electrically driven single-photon source monolithically integrated with nano-photonic circuitry. The electroluminescence from a quantum dot (QD) is coupled to a nanobeam waveguide. With careful design and fabrication, a small excitation area is achieved and emission from a single QD is observed. Correlation and cross-correlation measurements are used to verify the single-photon nature of the source, the propagation of the single-photons, and that emission originates from the same QD. Additionally the source is shown to be highly coherent with coherence properties which should be sufficient to observe non-classical interference, a key requirement for linear optical quantum computing.

Chapter 6 presents work on the monolithic integration of a single-photon source with a directional coupler. Photons emitted from a QD integrated with a beamsplitter are combined with photons originating from an external laser demonstrating Hong-Ou-Mandel interference. The observed interference visibility is explained via modelling of non-ideal source parameters and beamsplitter ratio.

Finally, Chapter 7 provides a summary of the experimental chapters and an overview of potential future work.

References

[1]R. P. Feynman, "Simulating physics with computers", International journal of theoretical physics **21**, 467–488 (1982) (see p. 1).

[2]P. W. Shor, "Algorithms for quantum computation: Discrete logarithms and factoring", in Foundations of Computer Science, 1994 Proceedings., 35th Annual Symposium on (1994), pp. 124–134 (see p. 1).

[3]L. K. Grover, "A fast quantum mechanical algorithm for database search", in Proceedings of the twenty-eighth annual ACM symposium on Theory of computing (1996), pp. 212–219 (see p. 1).

[4]J. I. Cirac and P. Zoller, "Quantum computations with cold trapped ions", Physical review letters **74**, 4091 (1995) (see p. 1).

[5]N. A. Gershenfeld and I. L. Chuang, "Bulk spin-resonance quantum computation", science **275**, 350–356 (1997) (see p. 1).

[6]Y. Nakamura, Y. A. Pashkin and J. S. Tsai, "Coherent control of macroscopic quantum states in a single-Cooper-pair box", Nature **398**, 786–788 (1999) (see p. 1).

[7]C. H. W. Barnes, J. M. Shilton and A. M. Robinson, "Quantum computation using electrons trapped by surface acoustic waves", Physical Review B **62**, 8410 (2000) (see p. 1).

[8]T. D. Ladd, F. Jelezko, R. Laflamme, Y. Nakamura, C. Monroe and J. L. O'Brien, "Quantum computers", Nature **464**, 45–53 (2010) (see pp. 1, 73).

[9]J. L. O'Brien, "Optical quantum computing", Science **318**, 1567–1570 (2007) (see p. 1).

[10]E. Knill, R. Laflamme and G. J. Milburn, "A scheme for efficient quantum computation with linear optics", Nature **409**, 46–52 (2001) (see pp. 1, 73, 93).

[11]T. B. Pittman, M. J. Fitch, B. C. Jacobs and J. D. Franson, "Experimental controlled-NOT logic gate for single photons in the coincidence basis", Physical Review A **68** (2003) 10.1103/PhysRevA.68.032316 (see p. 1).

[12]J. L. O'Brien, G. J. Pryde, A. G. White, T. C. Ralph and D. Branning, "Demonstration of an all-optical quantum controlled-NOT gate", Nature **426**, 264–267 (2003) (see p. 1).

[13] A. Politi, M. J. Cryan, J. G. Rarity, S. Yu and J. L. O'Brien, "Silica-on-Silicon Waveguide Quantum Circuits", Science **320**, 646–649 (2008) (see p. 1).

[14] M. A. Pooley, D. J. P. Ellis, R. B. Patel, A. J. Bennett, K. H. A. Chan, I. Farrer, D. A. Ritchie and A. J. Shields, "Controlled-NOT gate operating with single photons", Applied Physics Letters **100**, 211103 (2012) (see p. 1).

[15] J. L. O'Brien, A. Furusawa and J. Vučković, "Photonic quantum technologies", Nature Photonics **3**, 687–695 (2009) (see pp. 1, 73, 93).

[16] A. Crespi, R. Osellame, R. Ramponi, D. J. Brod, E. F. Galvão, N. Spagnolo, C. Vitelli, E. Maiorino, P. Mataloni and F. Sciarrino, "Integrated multimode interferometers with arbitrary designs for photonic boson sampling", Nature Photonics **7**, 545–549 (2013) (see p. 1).

[17] M. Tillmann, B. Dakić, R. Heilmann, S. Nolte, A. Szameit and P. Walther, "Experimental boson sampling", Nature Photonics **7**, 540–544 (2013) (see p. 1).

[18] M. A. Broome, A. Fedrizzi, S. Rahimi-Keshari, J. Dove, S. Aaronson, T. C. Ralph and A. G. White, "Photonic boson sampling in a tunable circuit", Science **339**, 794–798 (2013) (see p. 1).

[19] J. B. Spring, B. J. Metcalf, P. C. Humphreys, W. S. Kolthammer, X.-M. Jin, M. Barbieri, A. Datta, N. Thomas-Peter, N. K. Langford, D. Kundys et al., "Boson sampling on a photonic chip", Science **339**, 798–801 (2013) (see p. 1).

[20] B. T. Gard, K. R. Motes, J. P. Olson, P. P. Rohde and J. P. Dowling, "An Introduction to Boson-Sampling", in *From Atomic to Mesoscale: The Role of Quantum Coherence in Systems of Various Complexities.* Edited by S. A. Malinovskaya and Novikova, I (World Scientific Publishing Co, June 2015), pp. 167–192 (see p. 2).

[21] C. K. Hong, Z. Y. Ou and L. Mandel, "Measurement of subpicosecond time intervals between two photons by interference", Physical Review Letters **59**, 2044 (1987) (see pp. 2, 18, 93).

Chapter 2

Background

2.1 Semiconductor Quantum Dots

Quantum dots (QDs) are nanometre scale structures within which charge carriers are confined in all three spatial dimensions on the order of their de Brogile wavelength[22]. Many fabrication techniques exist to produce quantum dots[22–28], each with their own advantages and disadvantages. Of these methods it is epitaxial self-assembly that produces QDs with properties most suited for quantum information processing (QIP). Further details of QD growth are given in Section 3.2.1. Self-assembled quantum dots (SAQDs) have been successfully produced in many different semiconductor material systems including groups II-VI[25, 29, 30], III-V and IV[31]. Of these material systems, indium arsenide (InAs) SAQDs in a gallium arsenide (GaAs) matrix is the most studied. InAs QDs are excellent single-photon sources with a near zero multi-photon emission probability[32–38]. Additionally, standard mature fabrication technologies can be used with GaAs, allowing the creation of photonic circuits with monolithically integrated single-photon sources. The entirety of the work presented in this thesis utilises InAs SAQDs in a GaAs matrix.

2.1.1 Electronic and Optical Properties of InAs Quantum Dots

An InAs quantum dot consists of a nanometre scale island of nominally InAs surrounded by GaAs. In their pure forms gallium arsenide and indium arsenide

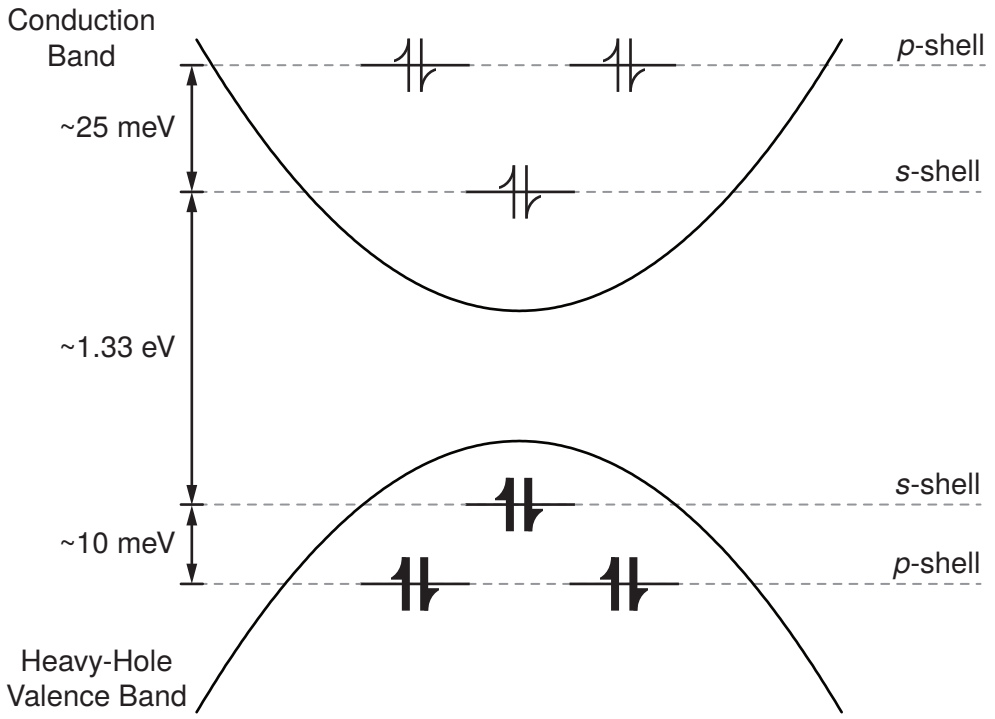

Figure 2.1 – Energy level diagram of the s and p-shells within a QD. Energy level spacing is not to scale. Exact energy level spacing depends upon QD growth parameters.

have bandgaps of 1.42 eV and 0.35 eV (both at 300 K) respectively. The large step-like difference in bandgap between the two materials creates a three-dimensional potential well which is able to confine charge carriers in quantised states[39]. In QDs the difference between the two bandgaps is not as large due to strain effects[40] which change the InAs band structure to be more complex as well as increasing its bandgap to be closer to that of GaAs[41]. Additionally, during the growth process gallium is able to diffuse from the surrounding GaAs into the QD resulting in a gradient of gallium in the structure, thereby further decreasing the difference in bandgap energies[42]. In addition the lowest energy levels are offset from the band edge due to confinement effects by approximately 400–500 meV and 70–100 meV for conduction and valence bands respectively[43]. As a result of these effects the typical lowest level energy separation for electrons and holes of 1.34 eV is observed for the quantum dots studied here. The emission energy can be controlled by changing growth conditions. A schematic diagram of the energy levels within a QD are shown in Figure 2.1.

Several properties of InAs QDs make them ideal for integration with photonic circuitry. Firstly, InAs is a direct bandgap semiconductor[44] and therefore efficient radiative relaxation is possible. Furthermore since the energy of the emitted photons are below the bandgap of the surrounding GaAs, the photons may propagate through the GaAs without reabsorption. This, along with the high refractive index of GaAs, allows the creation of low loss waveguides. Additionally the three dimensional quantisation of energy levels within a QD leads to a discrete electron/hole density of states. At low temperatures ($<50\,\mathrm{K}$) the energy separation of the discrete levels is greater than the thermal energy of electrons, k_BT, so the addition of a single electron or hole to the QD will populate only the lowest level state in the conduction band and valence band respectively. This allows the band structure to be well approximated by a two level system and gives the QD atom-like optical behaviour[45]. Because of this, QDs are often referred to as "artificial atoms" and makes them ideal for QIP applications.

Electrons and holes trapped within a QD form bound excitonic states. As each QD only contains one or two energy levels for electrons and holes[46] there is a relatively small number of excitonic states that can exist within a QD. The simplest of these is the neutral exciton which consists of a single electron and hole. The electron in the conduction band has an angular momentum of $l = 0$ (s-type) and spin $s = 1/2$ whereas the hole in the valence band has an angular momentum of $l = 1$ (p-type) and spin $s = 1/2$. In InAs QDs, the degeneracy of light ($m_j = \pm 1/2$) and heavy hole ($m_j = \pm 3/2$) states is lifted due to the strain present in the system from the lattice mismatch between GaAs and InAs. The energy levels of light holes and heavy holes are split by around 30 meV. As a result the light hole states are normally ignored when discussing the lower energy level states of a QD. Therefore the lowest energy level exciton states have total angular momentum projections of $m_j = \pm 1, \pm 2$. The states with $m_j = 2$ are dark states as they cannot recombine optically as an angular momentum transfer of twice that of a photon is required ($2\hbar$) to conserve angular momentum. Emission from exciton states with $m_j = \pm 1$ are allowed according to the dipole selection rules. These states are therefore known as bright excitons. The asymmetry of QDs results in the electron-hole exchange interaction lifting the degeneracy between the two bright states, known as fine structure splitting (FSS). The two bright states emit light that is orthogonally polarised to one another and aligned with the $[1\,1\,0]$ and

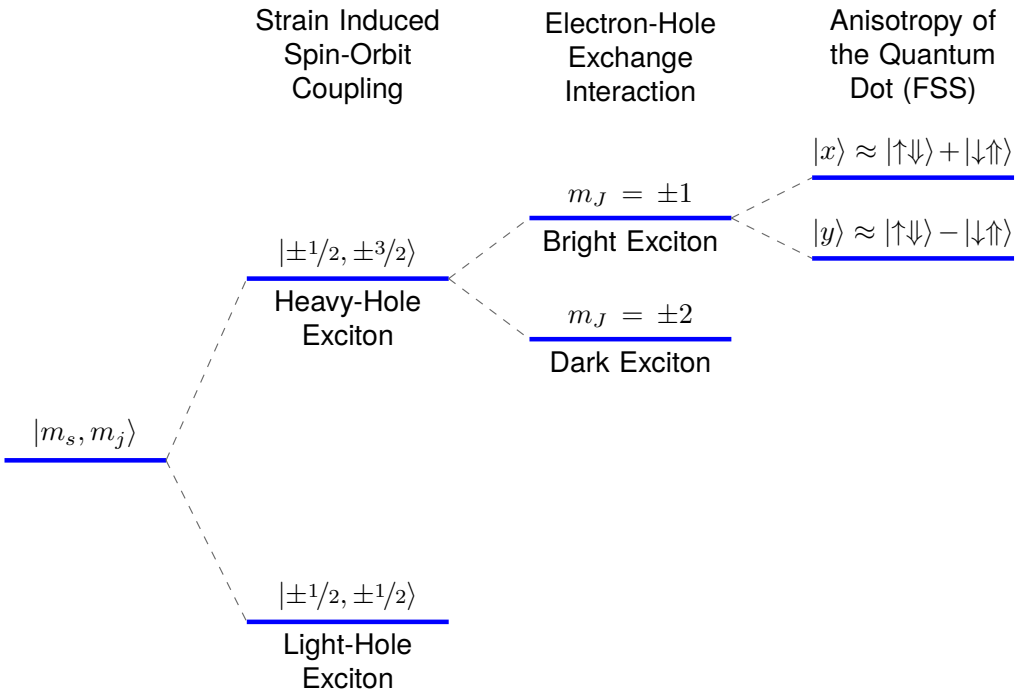

Figure 2.2 – Energy level diagram of neutral exciton states within a QD.

$[1\,\bar{1}\,0]$ crystal axes. A schematic diagram of the neutral exciton states are shown in Figure 2.2.

Other states can exist within the system such as the biexciton where the QD is populated by two electron-hole pairs. The biexciton is able to radiatively combine, emitting two photons successively[46]. The two photons differ in energy due to the Coulomb interaction between the charge carriers. Proposals and demonstrations have been made to use the biexciton cascade as a source of entangled photons[47–49] in quantum teleportation experiments[50]. Charged exciton states can also be formed when the QD contains a different number of electrons and holes. These states are optically active but have a different energy to the neutral exciton, again due to Coulomb interactions between the carriers.

2.2 Quantum-Confined Stark Effect

The wavelength of the light emitted upon recombination of the electron and hole is determined by the energy difference between the electron and hole states as well as the exciton energy. A simplified schematic of a quantum dot populated by a

single electron and hole forming an exciton is shown in Figure 2.3a. Applying an electric field to the device results in a modification of the band structure (Figure 2.3b). The exciton is still confined to the QD due to the band gap difference between the InAs QD and surrounding GaAs. The bending of the bands reduces the energy separation between the electron and hole thereby decreasing the energy of the photon emitted upon recombination. This change of the emission energy with electric field is known as the quantum-confined Stark effect (QCSE). The first observation of this effect in a semiconductor material was by Miller et al. in 1984[51]. The shift in emission energy, ΔE, as a function of electric field, F, is given by

$$\Delta E = pF + \beta F^2$$

where the linear coefficient p, is the electric dipole moment and the quadratic coefficient and β, the polarisability. The tuning range achievable in photoluminescence (PL) is the limited by the electron and hole tunnelling out of the QD before radiative recombination can occur. Tuning ranges of up to 25 meV have been to shown to be achievable with careful wafer design[52]. QCSE tuning is of great interest for QIP as it provides a scalable method of tuning the emission from a QD source. Previous experiments have confirmed this with the demonstration of two-photon interference of emission originating from two remote quantum dots[53].

2.3 Cavity Quantum Electrodynamics

An optical cavity is a system within which light is confined into standing wave modes by an arrangement of optical components. A rather simple example of this is a Fabry-Perot cavity which consists of two facing parallel mirrors. If we only consider the propagation of light in the direction perpendicular to the plane of the mirrors, the light is strongly confined within the cavity, repeatedly reflecting off the end mirrors. Consequently constructive and destructive interference occurs resulting in some frequencies having a highly increased amplitude whilst others are strongly suppressed. The amplified frequencies are known as the resonant frequencies of the optical cavity, ω_{cav}, and are dependent upon the cavity geometry. These correspond to modifications of the density of states from free-space to have

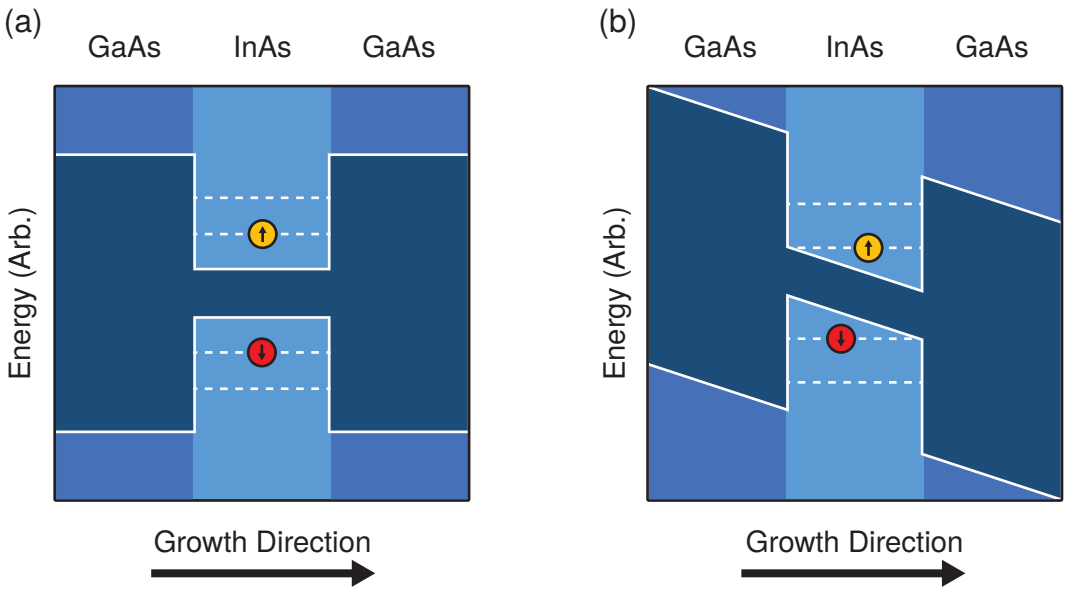

Figure 2.3 – Illustration of a quantum dot under a) flat-band conditions (i.e. zero electric field) and b) non-zero electric field. The energy of the exciton state has decreased relative to flat band. The electron and hole are shown in yellow and red, respectively.

a higher density at the resonant modes and a strong reduction off resonance.

For an ideal cavity without losses, the resonant modes would take the form of delta functions. However in a real optical cavity, the reflectors are never perfectly reflective. This results in the photons within the cavity having a finite lifetime and leads to lifetime spectral broadening of the cavity modes. The photon loss rate, κ, is commonly referred to in terms of the Q-factor of the cavity which is defined as

$$Q = \frac{\omega_{cav}}{\kappa}$$

Whilst the Q-factor characterises the cavity spectrally, the effective mode volume, V, describes the spatial extent. The mode volume is defined as the integral of the normalised electric field energy density over the cavity volume. The effective mode volume is typically referred to in units of cubic wavelengths $(\lambda/n)^3$.

Upon placing a quantum emitter such as a QD within a cavity, a modification of the photon emission process occurs due to interactions between the emitter and the cavity. The interaction that occurs is known as cavity quantum electrodynamics (cQED). It can be characterised with three parameters: the photon loss

rate, κ; the non-resonant emission rate, γ; and the emitter-photon coupling rate, g_0.

The non-resonant emission rate is the rate of emission into modes that are not supported by the cavity. This includes both emission into modes that are not resonant with the cavity as well as any non-radiative recombination processes. For InAs QDs at 5 K, the non-radiative recombination rate is negligible[54]. Careful cavity design can help reduce the emission into non-resonant cavity modes.

The emitter-photon coupling rate determines the rate of energy transfer between the emitter and cavity mode. This quantity is defined as

$$g_0 = \sqrt{\frac{\mu^2 \omega}{2\varepsilon_0 \hbar V}}$$

where μ is the electric dipole matrix element for the emitter transition and ε_0 is the permittivity of free space. The matrix element is determined by the size of the QD and the effective volume of the optical cavity.

The coupling of the emitter and cavity can be classified into two operating regimes: the weak coupling regime when photons are typically lost from the cavity before the emitter is able to absorb them i.e. $g_0 \ll (\kappa, \gamma)$, and strong coupling where, in a simplified picture, the photons are absorbed and re-emitted several times before leaving the cavity i.e. $g_0 \gg (\kappa, \gamma)$.

2.3.1 Weak Coupling

As the cavity modifies the density of states from free-space, and Fermi's golden rule states that the transition rate is proportional to the density of final states, a change in emission rate occurs for an emitter in a cavity. This effect is known as the Purcell effect, first observed by Edward Mills Purcell in 1946 with atoms in a resonant cavity[55]. The effect can be quantified with the Purcell factor which is defined as the ratio of the emission rate within the cavity, Γ_{cav}, and in the absence of a cavity, Γ_{free}:

$$F_P = \frac{\Gamma_{cav}}{\Gamma_{free}} = \frac{3}{4\pi^2} \left(\frac{\lambda}{n}\right)^3 \left(\frac{Q}{V}\right) \xi^2 L(\omega)$$

where λ/n is the wavelength within the material, Q is the quality factor, V is the effective mode volume, and $L(\omega)$ the lineshape of the cavity. ξ is the normalised

dipole orientation factor which represents the alignment of the emitter and cavity modes both spatially and in polarisation. It is defined as $\xi = {}^{|\mathbf{p}\cdot\mathbf{E}|}/_{|\mathbf{p}||\mathbf{E}|}$ where $\mathbf{p}$ is the emitter's dipole moment and $\mathbf{E}$ is the cavity's electric field. The lineshape of the cavity is a Lorentzian. If the emitter is on resonance with a cavity mode and at the antinode of the cavity, then $F_P > 1$ and a Purcell enhancement is observed. If however the emitter is sufficiently off-resonance, or not located close enough to the antinode, then the Purcell factor can be less than one resulting in Purcell suppression of the emission. The Purcell factor can be observed experimentally by measuring the change in lifetime of the emitter although care must be taken obtain an accurate lifetime for the emitter in the absence of a cavity.

2.3.2 Strong Coupling

In the strong coupling regime the emission of a photon from the emitter and into the cavity mode is a reversible process. For two-level emitters, such as QDs, the system is described by the Jaynes-Cummings model[56]. In a simplified picture, the photons emitted are held in the cavity long enough to be reabsorbed by the emitter and then re-emitted again. The oscillations between a cavity photon and exciton within the emitter are known as vacuum Rabi oscillations[57]. The cavity photon and exciton form a quasi-particle known as an exciton-polariton[58]. Quantum emitters strongly coupled to cavities exhibit very high extraction efficiencies[59, 60]. Experimentally strong coupling is confirmed by the presence of a splitting between the cavity mode and emission wavelength at resonance. If one is tuned through the resonance of the other an anticrossing will be observed[61–64].

2.3.3 Photonic Crystal Cavities

Photonic crystals (PhCs) consist of periodic variation in dielectric constant. Similar to an electronic bandgap arising from the periodic arrangement of atoms in a semiconductor, the periodic variation in dielectric constant leads to the formation of an optical bandgap. These structures were first suggested by Yablonovitch[65] and John[66] in 1987 as a method of controlling the optical modes of a material. Fabrication of a photonic crystal is challenging; the lattice constant of the photonic crystal must be comparable to the wavelength of the light. For the work presented in this thesis with light at 930 nm, a lattice constant of around 230 nm

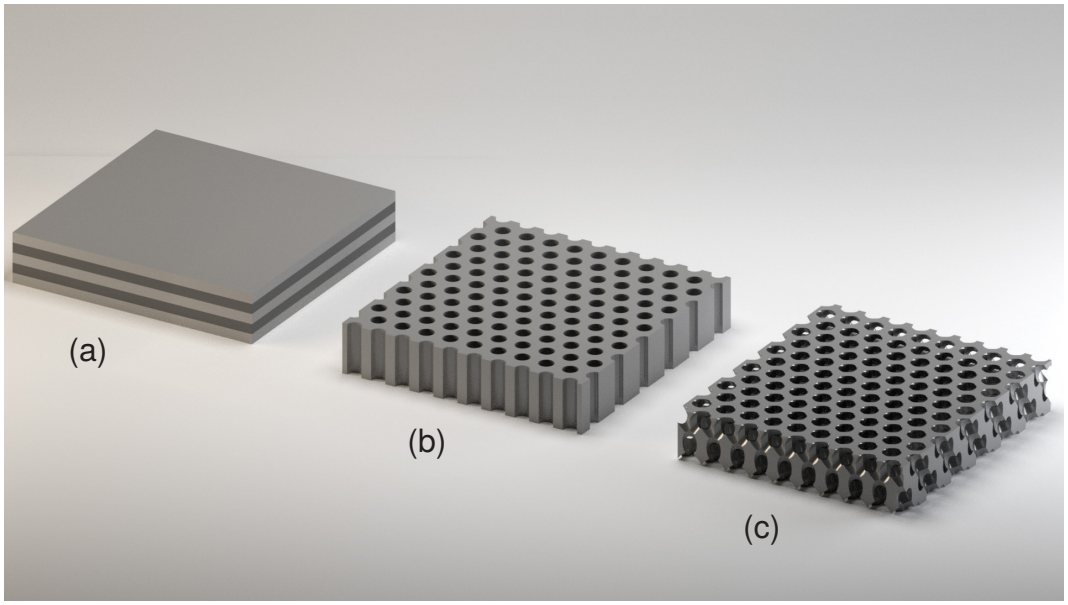

Figure 2.4 – Schematic of different PhCs designs. a) One-dimensional photonic crystal formed with alternating layers of two materials with different refractive index. b) Two-dimensional and c) three-dimensional photonic crystals formed by a periodic lattice of holes.

is used. At this scale state of the art fabrication techniques, such as electron beam lithography (EBL), are needed. Any defects introduced from errors in fabrication can create defect states within the photonic band gap. Defects can be purposely introduced to the PhC to create confined states within the crystal for use as photonic crystal cavities (PhCCs) or waveguides.

The most common form of PhC is a 1D photonic crystal where alternating layers of two materials of differing refractive index are stacked upon each other (e.g. molecular beam epitaxy (MBE) grown of layers of AlGaAs and GaAs). The periodicity of the system results in the formation of a bandgap at the edge of the Brillouin zone in this spatial direction. This system was first studied in 1887 by Lord Rayleigh[67]. An example of a 1D photonic crystal is shown in Figure 2.4a

Surprisingly the proposal to extend this to two and three-dimensional photonic crystals was not made until 100 years later. In a two dimensional photonic crystal the refractive index varies periodically along a plane while is constant perpendicular to the plane. For these devices a photonic bandgap occurs for light propagating in the plane. Typically these devices are fabricated by etching periodic arrays of holes into a substrate, illustrated in Figure 2.4b. The periodic variation in dielec-

tric constant is then provided by the difference in refractive index between bulk material and air/vacuum.

In three-dimensional photonic crystals the refractive index periodically varies in all three spatial directions leading to the formation of a full 3D photonic bandgap. Although such a system could in theory provide a method to produce a perfect lossless cavity, in practice the difficulty associated with fabricating such a structure limits its usefulness. The first three-dimensional photonic crystal was produced by Yablonovitch in 1991 by drilling three sets of holes along $\{1\,1\,0\}$ directions in a triangular lattice[68]. This structure is illustrated in Figure 2.4c.

The photonic bandgap of photonic crystals makes them ideally suited to the creation of high-Q optical cavities. By introducing a defect into an otherwise regular photonic crystal, a localised state within the photonic bandgap can be created. Additionally since the dimensions of the crystal are on the order of the wavelength of the light, very small mode volumes are achievable producing a large Purcell enhancement even for cavities with a modest Q-factor. As a three dimensional photonic crystal is limited by scattering from fabrication imperfections, most work relies upon using the photonic band gap to provide confinement in one or two dimensions and total internal reflection at the semiconductor-vacuum/air interface in the remaining spatial directions.

For the work presented in this thesis, two-dimensional photonic crystal membranes with a triangular lattice are used. In these devices a periodic array of holes are etched into a semiconductor membrane. The photonic bandgap provides confinement in plane and out-of-plane by total internal reflection. With these systems Q-factors up-to 9×10^6 have been observed experimentally in silicon[69]. The simplest cavity in this system, known as a H1 cavity, is formed by the omission of single hole (Figure 2.5a). Typically the holes nearest the cavity are also modified to maximise the Q-factor by preventing leaking to the vacuum mode. With this system Q-factors of up-to 2.5×10^4 have been reported with mode volumes as small as $0.47\,(\lambda/n)^3$ have been reported in GaAs at 950 nm[70]. Another commonly studied defect is an L3 cavity created by the omission of three holes in a line (Figure 2.5b). Again the holes nearest to the cavity are modified to maximise the Q-factor giving experimental Q-factors of up to 3×10^4 with a mode volume of $\sim 1\,(\lambda/n)^3$ in GaAs at 950 nm[64]. Omitting an entire line of holes can be used to create a W1 line defect which acts as a waveguide (Figure 2.5c). These systems

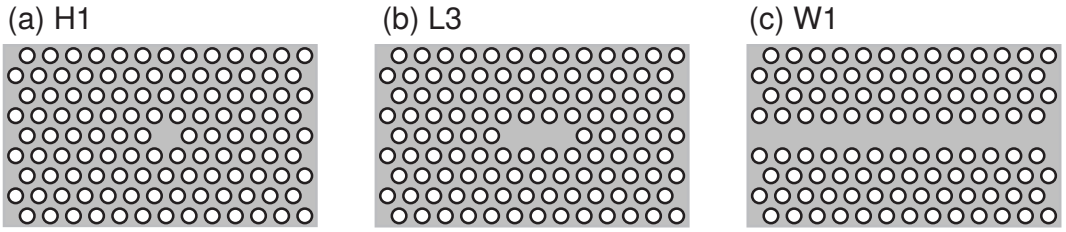

Figure 2.5 – Types of photonic crystal cavity. a) H1 cavity formed by removing a hole. b) L3 cavity formed by removing 3 holes. c) W1 waveguide created by removed a line of holes.

are attractive for the creation of on-chip photonic circuits due to ability to have sharp bends with low loss rates[71] and the relative ease to integrate with cavities and more traditional waveguide designs such as nano-beam, ridge, and polymer waveguides[72–76].

2.4 The Hong-Ou-Mandel Effect

The Hong-Ou-Mandel (HOM) effect is an important two-photon intensity interference effect which has proposed uses as the entangling mechanism in linear optical quantum computing (LOQC)[77]. The HOM effect occurs when two identical photons enter each input port of a beamsplitter. There are four possible paths that the photons may take, each of which is illustrated in Figure 2.6. In braket notation the output states can be represented by $|t, b\rangle$ where t and b are the number of photons exiting the top and bottom ports respectively. The four possible output states are when: one photon is reflected and the other transmitted ($|2, 0\rangle$ and $|0, 2\rangle$), or both photons are reflected or transmitted ($|1, 1\rangle$). The overall output state is:

$$|0, 2\rangle - |1, 1\rangle + |1, 1\rangle - |2, 0\rangle$$

since a phase shift of $e^{i\pi} = -1$ is introduced whenever a photon is reflected from the top surface of the beamsplitter. As the input photons are identical, the two $|1, 1\rangle$ states are indistinguishable from each other resulting in interference. One of these states involves a photon reflecting off the top surface of the beamsplitter and thus has a phase factor of -1 causing the interference to be destructive. The output state can be simplified to:

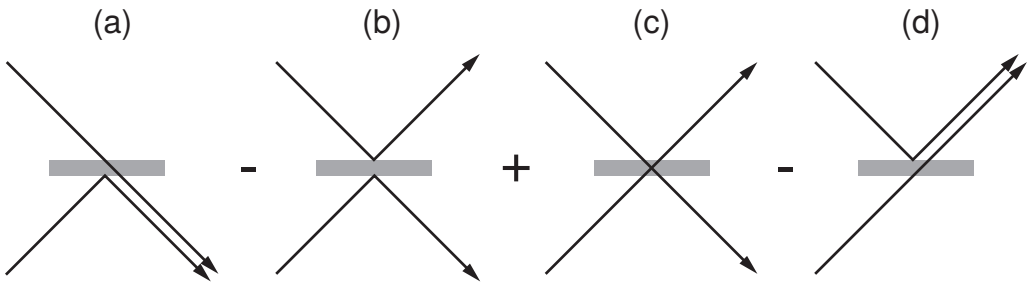

Figure 2.6 – The four possible paths for two photons incident on a beamsplitter: a) the top photon is transmitted and the bottom reflected, b) both photons are reflected, c) both photons are transmitted, and d) the top photon is reflected and the bottom transmitted. A π phase shift occurs upon reflection off the top surface introducing a minus sign.

$$|0,2\rangle - |2,0\rangle$$

Therefore identical photons will always exit the same side of the beamsplitter, they will never exit from separate output ports. This resulting photon state is known as a two photon N00N state. The effect was first observed by Chung Ki Hong, Zhe Yu Ou and Leonard Mandel in 1987[21].

References

[21]C. K. Hong, Z. Y. Ou and L. Mandel, "Measurement of subpicosecond time intervals between two photons by interference", Physical Review Letters **59**, 2044 (1987) (see pp. 2, 18, 93).

[22]M. A. Reed, "Spatial quantization in GaAs-AlGaAs multiple quantum dots", Journal of Vacuum Science & Technology B: Microelectronics and Nanometer Structures **4**, 358 (1986) (see p. 7).

[23]D. Leonard, M. Krishnamurthy, C. M. Reaves, S. P. Denbaars and P. M. Petroff, "Direct formation of quantum-sized dots from uniform coherent islands of InGaAs on GaAs surfaces", Applied Physics Letters **63**, 3203–3205 (1993) (see p. 7).

[24]J. Y. Marzin, J. M. Gerard, a. Izrael, D. Barrier and G. Bastard, "Photoluminescence of Single Inas Quantum Dots Obtained by Self- Organized Growth on Gaas", Physical Review Letters **73**, 716–719 (1994) (see pp. 7, 73).

[25]B. Lounis, H. Bechtel, D. Gerion, P. Alivisatos and W. Moerner, "Photon antibunching in single CdSe/ZnS quantum dot fluorescence", Chemical Physics Letters **329**, 399–404 (2000) (see p. 7).

[26]G. Chen, T. H. Stievater, E. T. Batteh, X. Li, D. G. Steel, D. Gammon, D. S. Katzer, D. Park and L. J. Sham, "Biexciton quantum coherence in a single quantum dot.", Physical review letters **88**, 117901 (2002) (see p. 7).

[27]W. Izumida, O. Sakai and S. Tarucha, "Tunneling through a quantum dot in local spin singlet-triplet crossover region with Kondo effect.", Physical review letters **87**, 216803 (2001) (see p. 7).

[28]Q. Xie, A. Madhukar, P. Chen and N. Kobayashi, "Vertically Self-Organized InAs Quantum Box Islands on GaAs(100)", Physical Review Letters **75**, 2542–2545 (1995) (see p. 7).

[29]K. Sebald, P. Michler, T. Passow, D. Hommel, G. Bacher and a. Forchel, "Single-photon emission of CdSe quantum dots at temperatures up to 200 K", Applied Physics Letters **81**, 2920–2922 (2002) (see p. 7).

[30]F. Tinjod, B. Gilles, S. Moehl, K. Kheng and H. Mariette, "II-VI quantum dot formation induced by surface energy change of a strained layer", Applied Physics Letters **82**, 4340–4342 (2003) (see p. 7).

[31]K. Brunner, "Si/Ge nanostructures", Reports on Progress in Physics **65**, 27 (2002) (see p. 7).

[32]P. Michler, A. Kiraz, C. Becher, W. V. Schoenfeld, P. M. Petroff, L. Zhang, E. Hu and A. İmamoğlu, "A Quantum Dot Single-Photon Turnstile Device", Science **290**, 2282–2285 (2000) (see pp. 7, 73).

[33]V. Zwiller, H. Blom, P. Jonsson, N. Panev, S. Jeppesen, T. Tsegaye, E. Goobar, M.-E. Pistol, L. Samuelson and G. Björk, "Single quantum dots emit single photons at a time: Antibunching experiments", Applied Physics Letters **78**, 2476 (2001) (see p. 7).

[34]Z. Yuan, B. E. Kardynal, R. M. Stevenson, A. J. Shields, C. J. Lobo, K. Cooper, N. S. Beattie, D. A. Ritchie and M. Pepper, "Electrically Driven Single-Photon Source", Science **295**, 102–105 (2002) (see pp. 7, 73).

[35]M. Pelton, C. Santori, J. Vučković, B. Zhang, G. S. Solomon, J. Plant and Y. Yamamoto, "Efficient Source of Single Photons: A Single Quantum Dot in a Micropost Microcavity", Physical Review Letters **89** (2002) 10.1103/PhysRevLett.89.233602 (see pp. 7, 73).

[36]C. Santori, D. Fattal, J. Vuckovic, G. S. Solomon and Y. Yamamoto, "Single-photon generation with InAs quantum dots", New Journal of Physics **6**, 89–89 (2004) (see p. 7).

[37]W.-H. Chang, W.-Y. Chen, H.-S. Chang, T.-P. Hsieh, J.-I. Chyi and T.-M. Hsu, "Efficient Single-Photon Sources Based on Low-Density Quantum Dots in Photonic-Crystal Nanocavities", Physical Review Letters **96** (2006) 10.1103/PhysRevLett.96.117401 (see pp. 7, 73).

[38]S. Strauf, N. G. Stoltz, M. T. Rakher, L. A. Coldren, P. M. Petroff and D. Bouwmeester, "High-frequency single-photon source with polarization control", Nature Photonics **1**, 704–708 (2007) (see pp. 7, 73).

[39]A. P. Alivisatos, "Semiconductor clusters, nanocrystals, and quantum dots", Science **271**, 933 (1996) (see p. 8).

[40]S. Guha, A. Madhukar and K. C. Rajkumar, "Onset of incoherency and defect introduction in the initial stages of molecular beam epitaxical growth of highly strained InxGa1=xAs on GaAs(100)", Applied Physics Letters **57**, 2110 (1990) (see p. 8).

[41]G. A. Narvaez, G. Bester and A. Zunger, "Dependence of the electronic structure of self-assembled (In, Ga)As/GaAs quantum dots on height and composition", Journal of Applied Physics **98**, 043708 (2005) (see p. 8).

[42]W. Sheng and J.-P. Leburton, "Electron-hole alignment in InAs/GaAs self-assembled quantum dots: Effects of chemical composition and dot shape", Physical Review B **63** (2001) 10.1103/PhysRevB.63.161301 (see p. 8).

[43]P. Michler, *Single Quantum Dots: Fundamentals, Applications and New Concepts*, Vol. 90 (Springer Science & Business Media, 2003) (see p. 8).

[44] A. Milnes and A. Polyakov, "Indium arsenide: a semiconductor for high speed and electro-optical devices", Materials Science and Engineering: B **18**, 237–259 (1993) (see p. 9).

[45] A. Zrenner, "A close look on single quantum dots", The journal of chemical physics **112**, 7790–7798 (2000) (see pp. 9, 28).

[46] R. Thompson, R. Stevenson, A. Shields, I. Farrer, C. Lobo, D. Ritchie, M. Leadbeater and M. Pepper, "Single-photon emission from exciton complexes in individual quantum dots", Physical Review B **64**, 201302 (2001) (see pp. 9, 10).

[47] O. Benson, C. Santori, M. Pelton and Y. Yamamoto, "Regulated and entangled photons from a single quantum dot", Physical review letters **84**, 2513 (2000) (see pp. 10, 78).

[48] R. M. Stevenson, R. J. Young, P. Atkinson, K. Cooper, D. A. Ritchie and A. J. Shields, "A semiconductor source of triggered entangled photon pairs", Nature **439**, 179–182 (2006) (see p. 10).

[49] A. J. Hudson, R. M. Stevenson, A. J. Bennett, R. J. Young, C. A. Nicoll, P. Atkinson, K. Cooper, D. A. Ritchie and A. J. Shields, "Coherence of an Entangled Exciton-Photon State", Physical Review Letters **99** (2007) 10.1103/PhysRevLett.99.266802 (see p. 10).

[50] M. Ward, M. Dean, R. Stevenson, A. Bennett, D. Ellis, K. Cooper, I. Farrer, C. Nicoll, D. Ritchie and A. Shields, "Coherent dynamics of a telecom-wavelength entangled photon source", Nature Communications **5** (2014) 10.1038/ncomms4316 (see p. 10).

[51] D. a. B. Miller, D. S. Chemla, T. C. Damen, a. C. Gossard, W. Wiegmann, T. H. Wood and C. a. Burrus, "Band-edge electroabsorption in quantum well structures: The quantum-confined stark effect", Physical Review Letters **53**, 2173–2176 (1984) (see p. 11).

[52] A. J. Bennett, R. B. Patel, J. Skiba-Szymanska, C. A. Nicoll, I. Farrer, D. A. Ritchie and A. J. Shields, "Giant Stark effect in the emission of single semiconductor quantum dots", Applied Physics Letters **97**, 1–4 (2010) (see pp. 11, 60).

[53]R. Patel, A. Bennett, I. Farrer, C. Nicoll, D. A. Ritchie and A. J. Shields, "Two-photon interference of the emission from electrically tunable remote quantum dots", Nature Photonics **4**, 632–635 (2010) (see pp. 11, 118).

[54]P. Lodahl, S. Mahmoodian and S. Stobbe, "Interfacing single photons and single quantum dots with photonic nanostructures", Reviews of Modern Physics **87**, 347 (2015) (see p. 13).

[55]E. M. Purcell, "Spontaneous emission probabilities at radio frequencies", Physical Review B **69**, 681 (1946) (see pp. 13, 64).

[56]E. T. Jaynes and F. W. Cummings, "Comparison of quantum and semiclassical radiation theories with application to the beam maser", Proceedings of the IEEE **51**, 89–109 (1963) (see p. 14).

[57]I. I. Rabi, "Space quantization in a gyrating magnetic field", Physical Review **51**, 652 (1937) (see p. 14).

[58]J. Hopfield, "Theory of the contribution of excitons to the complex dielectric constant of crystals", Physical Review **112**, 1555 (1958) (see p. 14).

[59]G. Cui and M. G. Raymer, "Quantum efficiency of single-photon sources in the cavity-QED strong-coupling regime", Optics express **13**, 9660–9665 (2005) (see p. 14).

[60]D. Press, S. Götzinger, S. Reitzenstein, C. Hofmann, A. Löffler, M. Kamp, A. Forchel and Y. Yamamoto, "Photon antibunching from a single quantum-dot-microcavity system in the strong coupling regime", Physical Review Letters **98**, 117402 (2007) (see p. 14).

[61]A. Kiraz, P. Michler, C. Becher, B. Gayral, A. İmamoğlu, L. Zhang, E. Hu, W. V. Schoenfeld and P. M. Petroff, "Cavity-quantum electrodynamics using a single InAs quantum dot in a microdisk structure", Applied Physics Letters **78**, 3932–3934 (2001) (see pp. 14, 56).

[62]T. Yoshie, A. Scherer, J. Hendrickson, G. Khitrova, H. Gibbs, G. Rupper, C. Ell, O. Shchekin and D. Deppe, "Vacuum Rabi splitting with a single quantum dot in a photonic crystal nanocavity", Nature **432**, 200–203 (2004) (see p. 14).

[63]J. P. Reithmaier, G. Sęk, A. Löffler, C. Hofmann, S. Kuhn, S. Reitzenstein, L. V. Keldysh, V. D. Kulakovskii, T. L. Reinecke and A. Forchel, "Strong coupling in a single quantum dot–semiconductor microcavity system", Nature **432**, 197–200 (2004) (see p. 14).

[64]K. Hennessy, A. Badolato, M. Winger, D. Gerace, M. Atatüre, S. Gulde, S. Fält, E. L. Hu and A. İmamoğlu, "Quantum nature of a strongly coupled single quantum dot–cavity system", Nature **445**, 896–899 (2007) (see pp. 14, 16).

[65]E. Yablonovitch, "Inhibited spontaneous emission in solid-state physics and electronics", Physical review letters **58**, 2059 (1987) (see p. 14).

[66]S. John, "Strong localization of photons in certain disordered dielectric superlattices", Physical review letters **58**, 2486 (1987) (see p. 14).

[67]L. Rayleigh, "XVII. On the maintenance of vibrations by forces of double frequency, and on the propagation of waves through a medium endowed with a periodic structure", The London, Edinburgh, and Dublin Philosophical Magazine and Journal of Science **24**, 145–159 (1887) (see p. 15).

[68]E. Yablonovitch, T. Gmitter, R. Meade, A. Rappe, K. Brommer and J. Joannopoulos, "Donor and acceptor modes in photonic band structure", Physical Review Letters **67**, 3380 (1991) (see p. 16).

[69]H. Sekoguchi, Y. Takahashi, T. Asano and S. Noda, "Photonic crystal nanocavity with a Q-factor of̃ 9 million", Optics express **22**, 916–924 (2014) (see p. 16).

[70]H. Takagi, Y. Ota, N. Kumagai, S. Ishida, S. Iwamoto and Y. Arakawa, "High Q H1 photonic crystal nanocavities with efficient vertical emission", Optics express **20**, 28292–28300 (2012) (see p. 16).

[71]A. Mekis, J. Chen, I. Kurland, S. Fan, P. R. Villeneuve and J. Joannopoulos, "High transmission through sharp bends in photonic crystal waveguides", Physical Review Letters **77**, 3787 (1996) (see p. 17).

[72]S. J. McNab, N. Moll and Y. A. Vlasov, "Ultra-low loss photonic integrated circuit with membrane-type photonic crystal waveguides", Optics express **11**, 2927–2939 (2003) (see p. 17).

[73]Y. A. Vlasov, M. O'Boyle, H. F. Hamann and S. J. McNab, "Active control of slow light on a chip with photonic crystal waveguides", Nature **438**, 65–69 (2005) (see p. 17).

[74]S. McNab and Y. Vlasov, "Coupling into the slow light mode in slab-type photonic crystal waveguides", Optics letters: A publication of the Optical Society of America, 50–52 (2006) (see p. 17).

[75]M. Banaee, A. Pattantyus-Abraham, M. McCutcheon, G. Rieger and J. F. Young, "Efficient coupling of photonic crystal microcavity modes to a ridge waveguide", Applied physics letters **90**, 193106 (2007) (see p. 17).

[76]J.-P. Hugonin, P. Lalanne, T. P. White and T. F. Krauss, "Coupling into slow-mode photonic crystal waveguides", Optics letters **32**, 2638–2640 (2007) (see p. 17).

[77]P. Kok, W. J. Munro, K. Nemoto, T. C. Ralph, J. P. Dowling and G. J. Milburn, "Linear optical quantum computing with photonic qubits", Reviews of Modern Physics **79**, 135–174 (2007) (see p. 17).

Chapter 3

Methods

This chapter outlines the computational and experimental methods used throughout the subsequent chapters. It begins with a brief overview of the computational techniques used. Following this, details of sample fabrication are discussed with an overview of molecular beam epitaxy (MBE) growth of quantum dots (QDs) and the fabrication techniques used to create electronic and photonic structures. Electrical characterisation methods and data are also presented along with the issues discovered in the current fabrication process. Subsequently, the spectral and temporal optical measurement techniques used are presented. Finally, the chapter concludes with an overview of the two cryogenic systems used to study QDs.

3.1 Computational Methods

All of the devices discussed and developed in the following chapters were first studied using computational methods. These tools allowed the behaviour of the devices to be investigated and optimised prior to fabrication. Two techniques were used: finite-difference time-domain (FDTD) methods[78–80] to study the temporal response of the photonic devices, and a frequency-domain eigenmode solver to study the properties of propagating modes[81, 82]. From the combination of the two techniques a complete picture of the device can be built up with expected losses, Q-factors and expected yields as well as whether the device is feasible to fabricate. All simulations were performed by Dr Rikki Coles and Dr Nikola Prtljaga.

3.2 Device Growth and Fabrication

In this section, the techniques used to fabricate the self-assembled QDs, photonic structures and diodes are presented. First MBE growth of a typical QD wafer is discussed before moving on to the lithographic techniques used to produce diodes and photonic structures.

For all the devices presented in this thesis the wafer growth was performed by Dr Edmund Clarke and any further processing of the wafers by Dr Benjamin Royall, Dr Deivis Vaitiekus and myself.

3.2.1 Quantum Dot Growth

In order to grow semiconductor QDs within a slab structure, the ability to deposit layers of semiconductor material monolayer by monolayer is required. Additionally, the ability to produce abrupt changes in material composition whilst maintaining a high degree of control over growth conditions is needed. Several epitaxial growth techniques are able to satisfy these criteria such as MBE and metalorganic vapour phase epitaxy (MOVPE)[83]. All of the samples presented here were grown using MBE.

A simplified schematic diagram of an MBE reaction chamber is shown in Figure 3.1a. The reactor consists of a high to ultra-high vacuum chamber (up to 10^{-12} mbar) with several effusion cells. To grow a wafer, ultra-pure solid elements, such as gallium or arsenic, within the cells are heated until the element sublimes. A shutter in front of the cells is opened, allowing the gaseous elements to enter the chamber, condense, and react on a pre-cleaned epi-ready wafer. Compound semiconductors such as GaAs can be grown by opening shutters to two sources so the beams will react at the wafer surface. The beams of gasses only interact at the wafer surface due to the atoms' long mean free path length. The wafer is held at an elevated temperature so that annealing can occur. Using this technique high purity wafers with very few defects can be produced[84].

Self-assembled quantum dots (SAQDs) are produced using the Stranski-Krastanov method[85–87] which relies upon an instability in epitaxial growth where there is a lattice mismatch known as the Asaro-Tiller-Grinfield instability[88, 89]. As a lattice mismatched layer is grown, elastic energy builds up in the film. After reaching a critical thickness it becomes energetically favourable to form discrete islands.

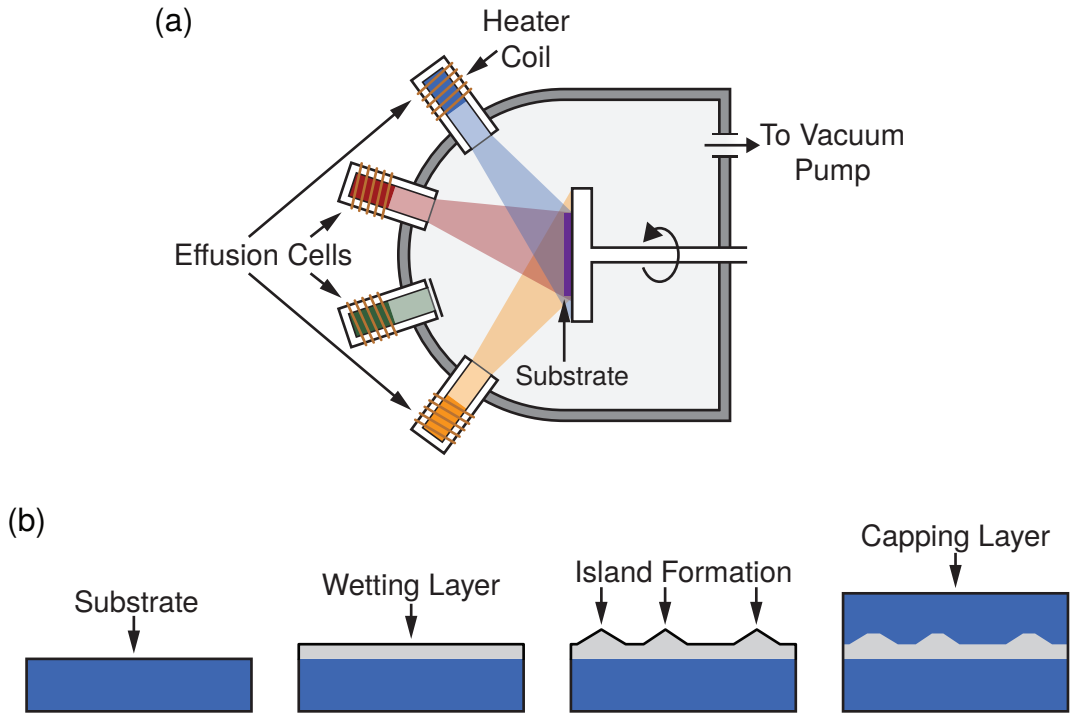

Figure 3.1 – a) Simplified diagram of an MBE chamber. b) Diagram of the Stranski-Krastanov growth method of InAs QDs (grey) on a GaAs substrate (blue).

This process is depicted in Figure 3.1b. For the InAs QDs presented here, layers of InAs are grown upon a [1 0 0] GaAs substrate. A lattice mismatch of approximately 7 % exists between the two. After growth of approximately two monolayers, the InAs relaxes into 3D islands with a diameter and height of 20 nm and 5 nm respectively. Exact dimensions can vary depending upon growth conditions[45, 90]. The wafer is then capped with another GaAs layer to move the air-substrate interface further from the QDs. This helps improve the optical quality of the QDs because if the surface is close, dangling bonds at the interface provide efficient non-radiative recombination pathways quenching the emission of the QD. As the structure is grown on a [1 0 0] wafer, it can be easily cleaved along its crystal axes using standard scribe and break techniques.

For diode samples, a doped layer is grown above and below the QD layer. The electrical samples presented in this thesis use beryllium as the p-type dopant and silicon as the n-type dopant.

3.2.2 Fabrication of Diodes

The fabrication of diodes is performed using three separate photolithography steps to create a mesa structure and define the contacted areas. First, the mesa structure is created as follows. The sample is cleaned using n-butyl acetate, acetone, and isopropyl alcohol and prebaked to remove any surface contaminants. The sample is then spin coated with a layer of SPR350 photoresist at 4000 rpm for 30 s to create a layer approximately 1 µm thick in the centre. The photoresist is then prebaked at 90 °C for 60 s. After spin coating, the resulting layer is non-uniform due to the surface tension of the resist. This causes the edges of the resist to bead up which can result in issues with mask alignment/exposure as close contact with the mask cannot be achieved across the entire sample. To prevent these issues, the edge bead is removed with acetone applied to the edge of the wafer only.

A UV mask aligner is used to expose the sample with a predefined mesa pattern. The photoresist is then developed in MF26a for approximately 1 min or until development is complete. SPR350 is a positive photoresist so all exposed areas are removed leaving a re-entrant profile where the bottom is wider than the top. The sample is then wet etched using either sulphuric acid (H_2SO_4 : 8 H_2O_2 : 80 H_2O) or phosphoric acid (H_3PO_4 : 4 H_2O_2 : 45 H_2O) (for 30 % H_2O_2) with periodic etch depth testing performed using a stylus profilometer. This entire process is

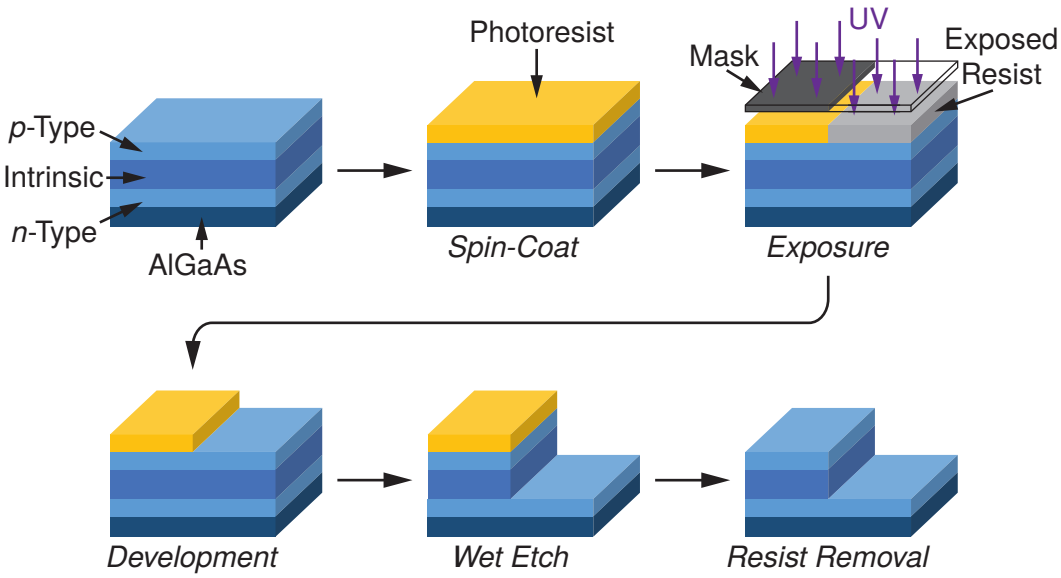

Figure 3.2 – Schematic of the fabrication process used to etch a mesa structure. A layer of photoresist is spin-coated onto the sample. The sample is exposed to ultraviolet light in a mask aligner. The resist is then developed, removing the exposed areas. A wet etch is perfomed to reach the n-type layer before finally the photoresist is removed with acetone.

depicted in Figure 3.2.

This process is then repeated twice for the addition of n-type and p-type ohmic contacts with a few changes. A bi-layer lift-off process is used with two photoresists spun onto the sample; the first is PMGI (5000 rpm, 30 s then baked for 5 min at 150 °C) and the second is a SPR350 layer as before. The PMGI is used as an undercut layer to increase the reliability of the lift-off process. After exposure and development, the surface oxide is removed using an ammonia solution (1 NH_3 : 30 H_2O). Exposure to the atmosphere and H_2O_2 present in the etchant, creates an oxide layer on the surface of the sample. If this layer remains on the surface, the diode's current-voltage (IV) properties will be degraded. Although regrowth of the layer begins to occur within seconds of removal, good IVs are achievable by quickly loading the sample into a thermal evaporator after removal. For the p-type layer a Ti/Au contact is used with thicknesses of 20 nm/200 nm. The n-type contact is Ni/GeAu/Ni/Au with thickness of 5 nm/20 nm/20 nm/200 nm. Lift-off was performed by placing the sample in an acetone bath overnight to swell the photoresist and remove it from the wafer. A three solvent clean is then performed to clean the wafer. The n-type contact undergoes a rapid thermal anneal (RTA)

at 360 °C for 3 s. The wafer is cleaved and mounted with gold epoxy to either a 12 pin TO-5 header or a 20 pin open-cavity ceramic leadless chip carrier (LCC) depending upon sample requirements. The electrical connections to the package are then made using a gold wire ball bonder.

3.2.3 Fabrication of Photonic Structures

To achieve the resolution needed to fabricate photonic structures, electron beam lithography (EBL) is used instead of photolithography. As with photolithography, the wafer is first cleaned and baked to remove any surface contaminants. In order to improve the adhesion of the photoresist to the surface, the surface is treated with hexamethyldisilane (HMDS), an adhesion promoter. ZEP520A is then spun onto the sample at 5000 rpm for 30 s. ZEP520A is a positive electron beam resist which can allow feature sizes down to approximately 10 nm. The resist is baked onto the sample at 180 °C for 5 min.

Computer aided design (CAD) software is used to design a pattern which is then produced in the resist by exposing the sample with a scanning electron beam. The resist is then developed in xylene, leaving a mask for subsequent etching. The mask is transferred to the GaAs wafer by an inductively coupled plasma (ICP) etch. ICP etching is a highly anisotropic etching process capable of producing extremely vertical sidewalls[91]. A typical ICP reactor consists of a vacuum chamber within which a gas is fed in and a plasma formed via the application of a strong radio frequency (RF) field. A secondary RF field is applied which causes the electrons to accelerate to high velocities (due to their lower mass) and collide with the chamber. This results in a negative self-biasing of the walls and wafer plater. The walls are grounded and therefore have no net change in charge whereas the wafer plater is floating allowing a large voltage to build up. The large voltage difference causes the ions to drift towards the plater colliding with the wafer to be etched. Due to the (mostly) vertical movement of the ions the etching is anisotropic. For the process here a mixture of silicon tetrachloride, $SiCl_4$, and argon is used. Within the mixture chlorine is the etchant reacting with the gallium arsenide as follows:

$$GaAs + 3\,Cl_2 \longrightarrow GaCl_3 + AsCl_3$$

During this process $GaCl_3$ accumulates upon the surface of the sample due

to its low volatility masking the surface from reacting with chlorine ions. This micromasking can increase surface roughness significantly[92, 93]. By bombarding the material with ions the volatility increases[94] however with chlorine ions this process is fairly inefficient and so argon is used instead[92, 93]. Argon has the additional advantage of not reacting with the wafer itself[95].

Adding silicon to the mixture of gases can further improve the degree of anisotropy. The silicon results in the deposition of silicone dioxide and silicon dichloride radicals upon the wafer[96, 97]. These products do not react with chlorine however they can be effectively sputtered by the bombardment of argon atoms. Since the argon atoms are travelling almost vertically they only remove the silicon compounds at the bottom of the etched features and not the side walls. This passivates the side walls and produces extremely vertical side walls[91].

After ICP etching the ZEP520A mask is removed by first exposing to ultraviolet light to decompose the polymers within the resist, then soaking in n-methyl-2-pyrrolidinone for 4 min at 100 °C. It is then soaked in isopropyl alcohol and a low energy oxygen plasma etch is performed to remove any remaining resist.

To form a free standing structure clad by air/vacuum on either side, the $Al_{0.6}Ga_{0.4}As$ sacrificial layer is selectively removed using hydrofluoric acid. A selectivity ratio of over $10^5 : 1$ between $Al_{0.6}Ga_{0.4}As$ and GaAs can be achieved[98]. A typical under etch involves etching 1–2 µm of $Al_{0.6}Ga_{0.4}As$ which will result in an etch of less than 1 nm of the GaAs photonic structure.

When drying suspended nano-structures the effects of the surface tension of the rinsing agent can become significant. As the rinsing agent underneath the structures dries, the surface tension pulls the structures downwards towards the substrate. This can often break suspended structures, especially those with large aspect ratios. The solution to this problem is to use supercritical point drying with CO_2[99]. A supercritical fluid has no surface tension and makes it possible to dry the sample without passing through a phase boundary, allowing large suspended structures to be made.

The critical point drying procedure is outlined in Figure 3.3. First acetone is used to remove any water from the sample as it is completely miscible with both water and liquid CO_2. The chamber is then pressurised and liquid CO_2 added, dissolving the acetone. The chamber pressure and temperature are increased causing the CO_2 to transition into a supercritical fluid. The pressure is then dropped

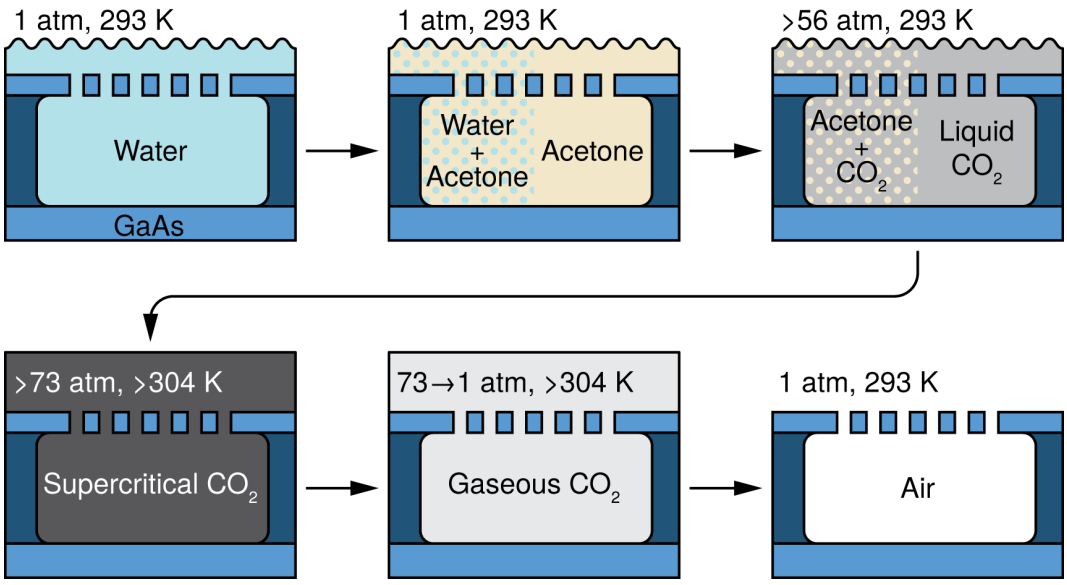

Figure 3.3 – Schematic of the critical point drying process. A sample immersed in water is purged with acetone. The chamber is then pressurised and liquid CO_2 is added. The chamber conditions are changed to cause the CO_2 to become supercritical. By then dropping the pressure the CO_2 become gaseous, leaving a dry sample.

by venting the chamber, allowing the supercritical fluid to transition into a gas. The end result is a dry sample which has not been exposed to the liquid-gas phase boundary. Scanning electron microscope (SEM) image of devices dried with and without supercritical drying is presented in Figure 3.4. Carbon dioxide is used for this process as it does not react with the sample and the critical point is below the damage threshold of the sample. Alternative fluids require either high temperatures, e.g. water, or react with the sample, e.g. nitrous oxide.

Quality control of the sample fabrication procedure is provided by frequent optical imaging throughout the process as well as SEM imaging at key stages. By analysing the resulting images statistical information on device fabrication can be obtained. The information can be fed back into the device design and fabrication processes to iteratively improve device performance. Additionally, structural information about the fabricated devices can be obtained to better compare theoretical and experimentally obtained data.

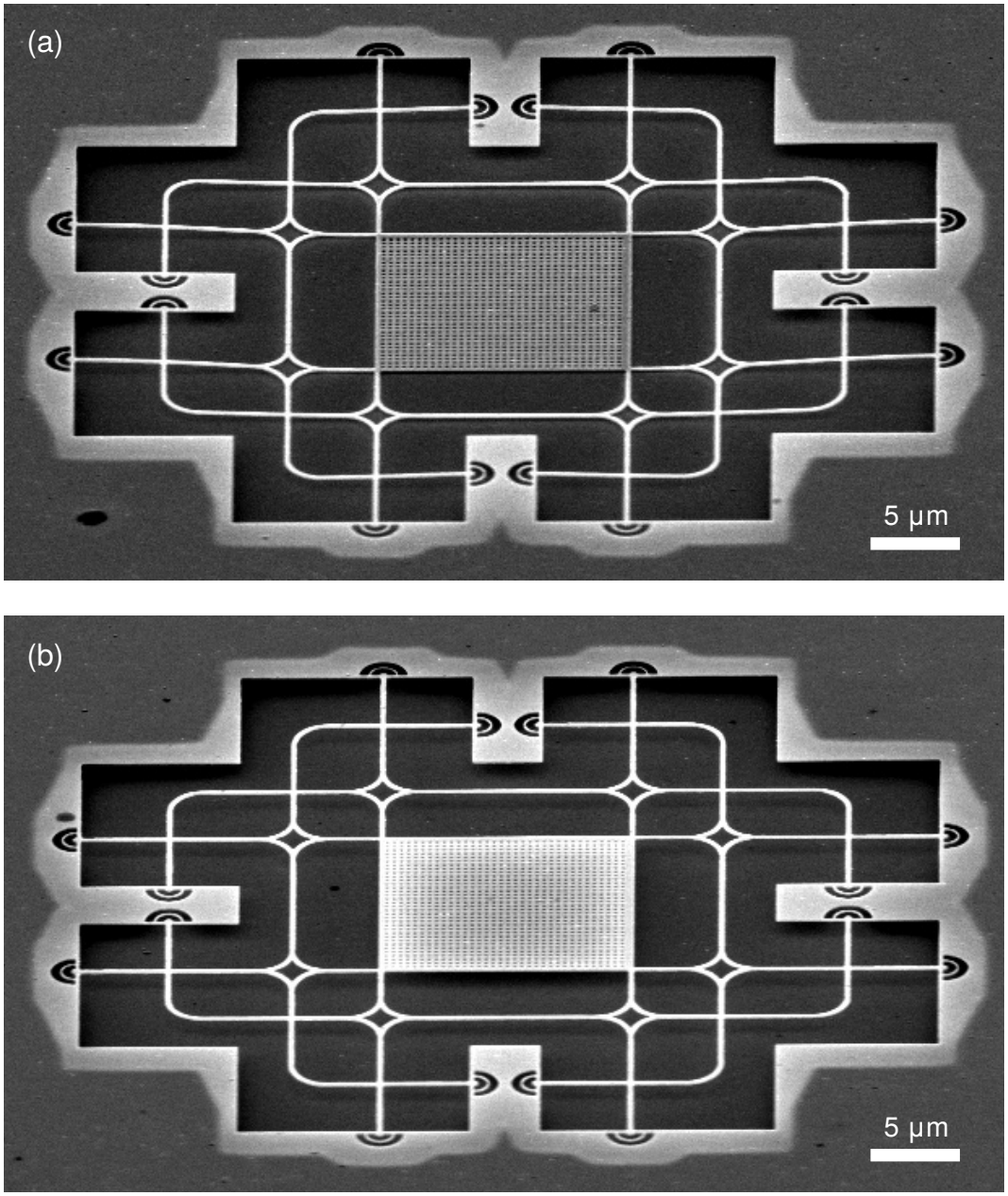

Figure 3.4 – SEM images of a free standing membrane structure a) dried without and b) with critical point drying. Devices and images were produced by Dr Benjamin Royall.

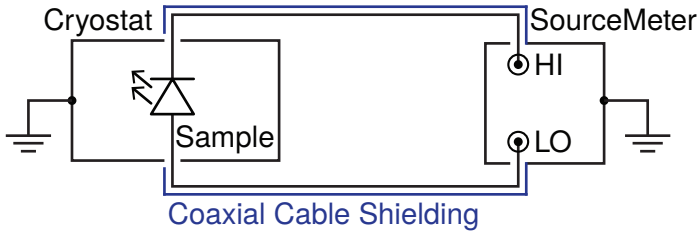

Figure 3.5 – Schematic diagram of the electrical testing setup. The blue lines represent the shield layer of the coaxial cable.

3.3 Electrical Device Characterisation

After device fabrication, all diode samples were electrically characterised to verify proper device operation. IV characteristics were recorded at 300 K, 77 K and 5 K using a source-measure unit (Keithley 6487 or 2400). A schematic of the circuit is presented in Figure 3.5. The measurement circuit was designed to reduce noise from external interference and ground loops. To achieve this, signal lines were routed along separate coaxial cables with earthed shields. A single common earthing point on the source-meter was used for all cabling, with the exception of the cryostat which was earthed to the optical table. A break in the shielding prevented any current flow due to the two different earth points.

Inside the cryostat the electrical connections varied depending upon the package used. For samples packaged inside a TO-5 can, the can was held in place with a clamping ring and electrically connected with individual socket connectors on the package's legs. The LCC package required the production of a printed circuit board (PCB) with a socket for the package to clip into (Figure 3.6). This design allowed rapid sample changes with minimal risk of damage to the sample.

3.3.1 Parasitic Diode

Electrical characterisation revealed a significant change in IV characteristics between devices produced before and after January 2014 (Figure 3.7). To obtain more information into the cause of the lower turn-on voltage, IV and differential conductance measurements were performed over a large current range on the newer diodes (Figure 3.8a). The two step-like features observed in the differential conductance is indicative of the presence of two parallel diodes with limiting resistors in series. Comparing the IV curves with photoluminescence (PL) and electroluminescence

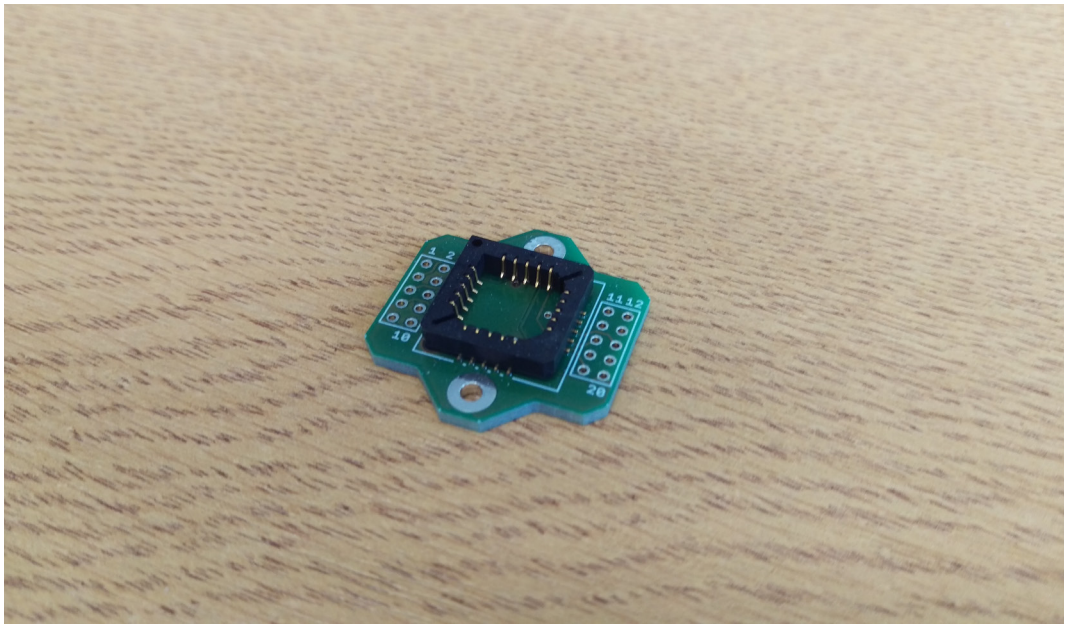

Figure 3.6 – Photograph of the mount for samples within an LCC package.

(EL) measurements shows the second turn-on corresponds to the onset of EL (Figure 3.8b). Therefore the first turn-on must correspond to a different current path through the device which does not pass through the QDs as otherwise EL emission would be observed. Figure 3.9 shows the proposed circuit diagram of the diode.

In order to determine the cause of the extra current path, a systematic set of tests were performed on every change made to the diode fabrication procedure. These included: testing etch depth, contact type, contact deposition method, bonding and annealing. Out of these only annealing after contact deposition affected the IVs significantly. This indicates that the source of the parasitic diode may be the diffusion of gold atoms from the contact into the diode. The issue is present in all of the devices presented in this thesis resulting in higher than expected biases needed for device operation.

3.4 Optical Device Characterisation

The samples were optically characterised at 5 K using a variety of techniques. These include micro-photoluminescence (μPL) spectroscopy to study the general emissive behaviour of the devices, and time-correlated single photon counting

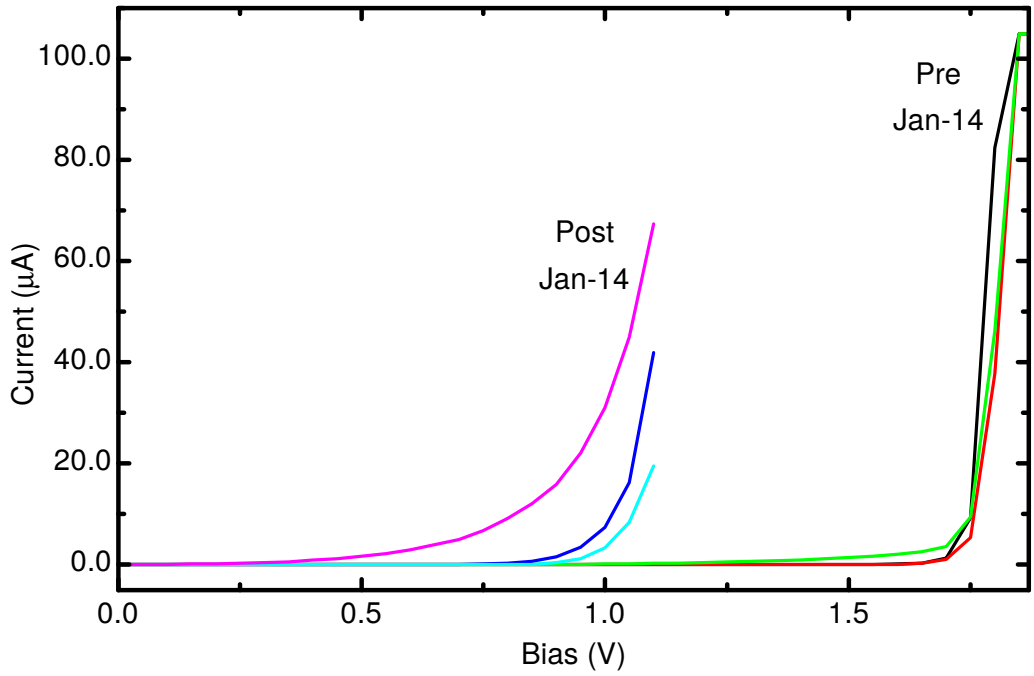

Figure 3.7 – Comparison of IV characteristics before and after January 2014

(TCSPC) measurements to study the temporal evolution of states within the QDs. This section details the automation used, the optical techniques and finally types of cryostat used.

3.4.1 Software Automation

In order to reduce the man-hours that some experiments required they were automated using LabVIEW. The automation allowed measurements to be run over extended times and with a greater level of detail than what would have been possible if a constant presence in the laboratory was required. A hardware abstraction layer (HAL) was used to hide differences in the test equipment such that a single program could be used to perform similar measurements on many experimental setups with varying underlying hardware. The HAL was implemented using an instrument-centric approach where each instrument derives from a common instrument class (Figure 3.10). The base instrument class declares several pure virtual functions and parameters common to all instruments (e.g. `Open`, `Initialise`, and `Close`). Inheriting from this class is an abstract class for each instrument type (e.g. digital multimeter (DMM), single photon counter (SPC) and spectrometer)

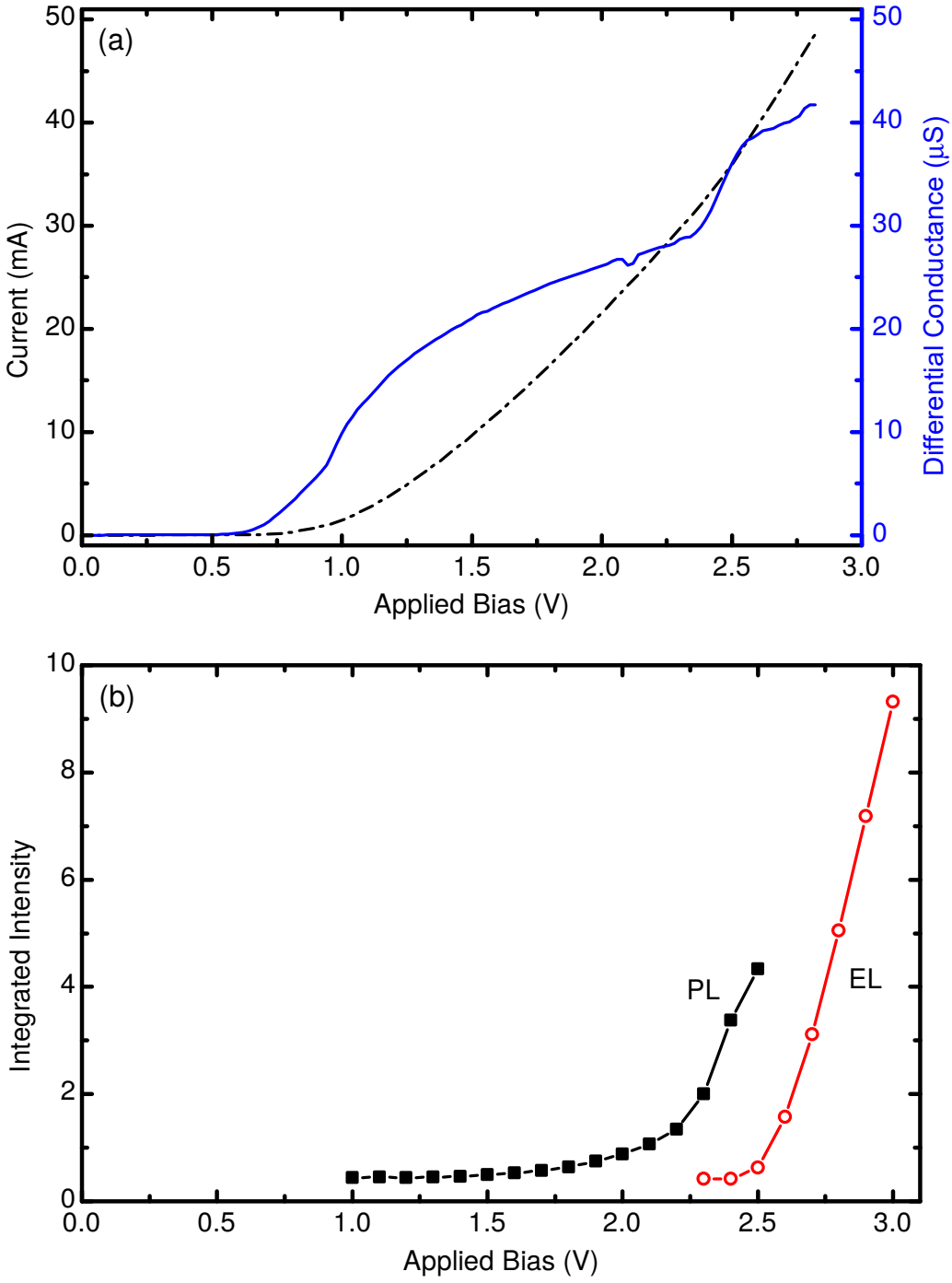

Figure 3.8 – Measured poor behaviour of a recent diode sample. a) IV (black dashed line) and differential conductance (blue line) measurements for the same diode without illumination. Two step-like features are observed in the differential conductance indicating the presence of two diodes. The second step corresponds to the EL onset voltage. b) Integrated intensity of photoluminescence (PL) (black line and squares) and electroluminescence (EL) (red line and circles). EL onset observed at 2.5 V.

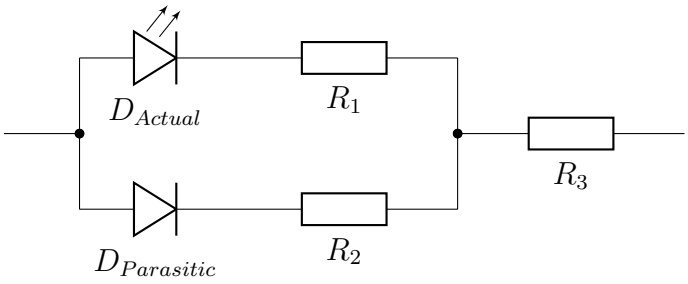

Figure 3.9 – Diagram of equivalent circuit to parasitic diode defects.

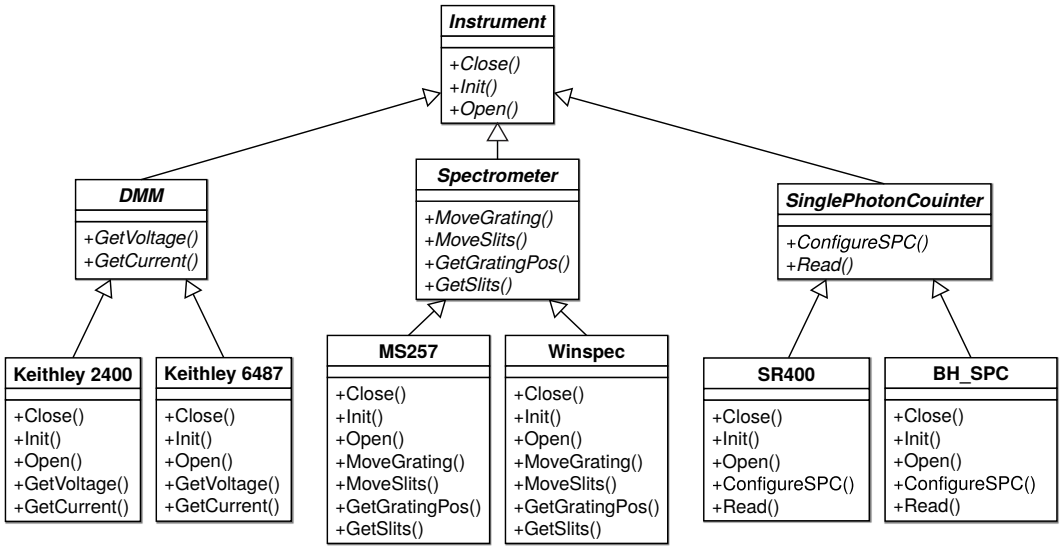

Figure 3.10 – Simplified class diagram of the HAL.

which declare further virtual functions specific to that instrument. A hardware specific class inherits from the instrument type class containing implementations of all inherited virtual functions. The application then only refers to the abstract instrument type classes, utilising polymorphism to select the correct hardware specific implementation. By doing so the application is agnostic to the underlying hardware configuration allowing test equipment to be changed with minimal downtime.

3.4.2 Microphotoluminescence Spectroscopy

Quantum dots can be made to fluoresce with either electrical or optical excitation. EL emission is generated when a large forward bias is applied. Electrons and holes are swept across the device by the applied field and relax into a bound excitonic

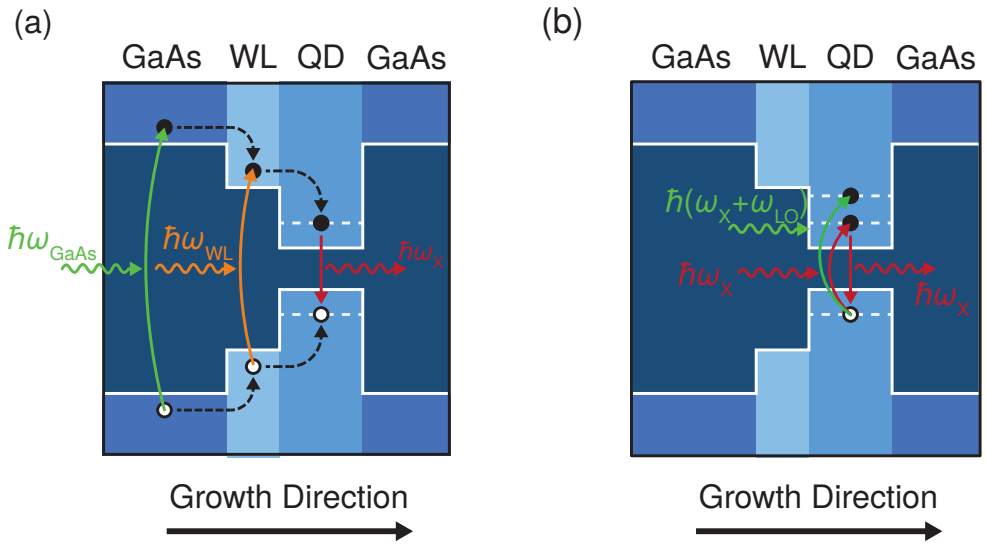

Figure 3.11 – Schematic of a) non-resonant and b) quasi resonant and resonant excitation schemes.

state within the QD via scattering and phonon interactions. The electron and hole then radiatively combine emitting a photon. The devices discussed in Chapter 5 rely upon this process. For the rest of the devices presented in this thesis, PL emission is used. PL is the process in which an electron-hole pair is generated by optical excitation and subsequently radiatively recombines emitting a single photon. Analysis of the fluorescence from the QD can be used to reveal information about the internal electronic structure of the QD and its environment.

For QDs, there are three distinct methods of optical excitation: non-resonant, quasi-resonant and resonant excitation. In non-resonant excitation the incoming photon has an energy: between the bandgap energies of the wetting layer and GaAs (referred to as wetting layer excitation) or above the GaAs bandgap. The generated electron-hole pair then either radiatively recombines emitting a photon at the bandgap energy of GaAs or wetting layer, or may be captured by the QD's 3D potential well. For capture to occur the carriers must relax via scattering or phonon interactions into the discrete QD states. These relaxation processes occur quickly but remove any coherence with the excitation photons. The process of non-resonant excitation is illustrated in Figure 3.11a.

In quasi-resonant excitation the energy of the incident photon is either equal to that of either a p-shell state[100] or a longitudinal optical (LO) phonon-assisted

optical transition[101, 102]. For p-shell excitation a polaron state is generated within the QD which then decays into the s-shell ground state within tens of picoseconds[103, 104]. With LO phonon excitation the incident photon is absorbed and generates an LO phonon, leaving the exciton in the ground state. Resonant excitation directly excites the ground state transition at the Rabi frequency[105, 106]. The main difficulty associated with resonant excitation is due to the incoming photons and emitted photons having the same energy. Separation of incident and emitted light is a challenge that requires careful sample and optical setup design. Unlike non-resonant excitation, both quasi-resonant and resonant excitation maintain some of the coherence of the incoming light due to the relatively small number of non-radiative relaxation processes required. Quasi-resonant and resonant excitation processes are illustrated in Figure 3.11b.

3.4.3 Photoluminescence Excitation Spectroscopy

To excite p-shell and LO phonon-assisted states, knowledge of the internal electronic structure of the QDs is required. Variations in size, shape, and the environment around the QDs cause the electronic structure to differ from dot to dot. The electronic structure can be mapped by performing photoluminescence excitation (PLE) measurements[107–109]. In PLE measurements the excitation energy is scanned whilst recording PL intensity. Peaks in the measured variations of PL intensity correspond to resonances where a photon is absorbed, generating an electron-hole pair which relaxes into the ground state of the QD. An example PLE spectrum is shown in Figure 3.12.

3.4.4 Time-Correlated Single Photon Counting

Although the measurement techniques presented in Section 3.4.2 are able to provide information on the transition energies of optically active excitonic states within the QD, they are unable to provide information into the temporal evolution of the states or the temporal profile of the emitted photons. To perform these measurements time-correlated single photon counting (TCSPC) is used. TCSPC is a statistical method that measures the difference in arrival time between a reference signal and the emitted light. A single photon counting module (SPCM) is used to record the time difference and histogram the data with a configurable bin

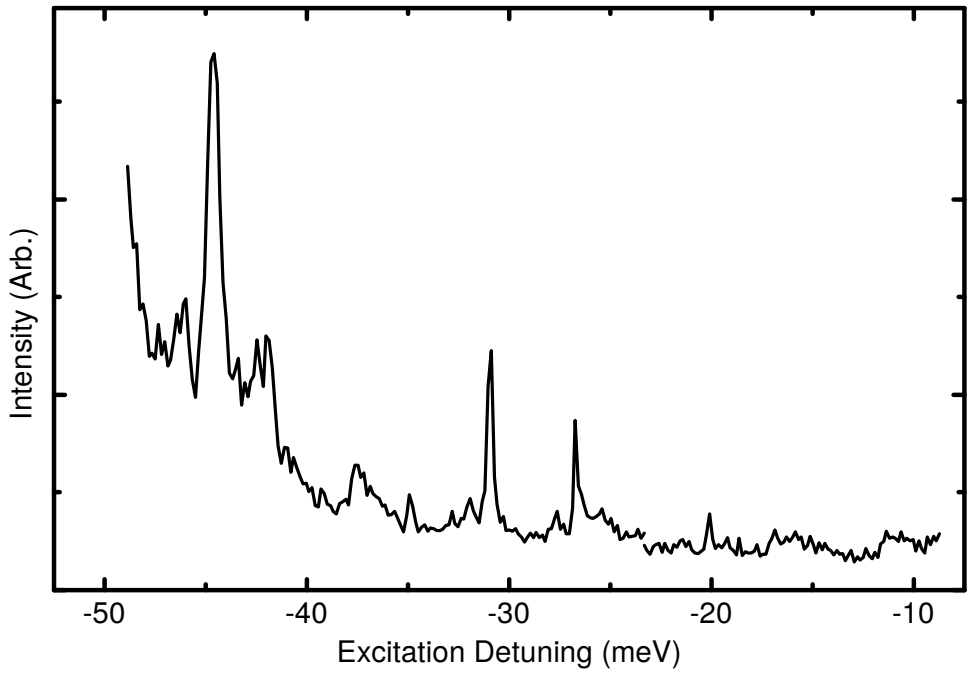

Figure 3.12 – Example spectrum obtained with PLE spectroscopy. Peaks in intensity correspond to resonances with states within the QD which lead to populating the ground state.

size (typically 98 ps or 24 ps). Measurements require high repetition rates in order to accumulate a sufficient number of events so that statistical significance can be achieved.

3.4.4.1 Lifetime Measurements

TCSPC can be used to study the lifetimes of optical active states within a QD. This is achieved by exciting the QD with a femtosecond pulsed Ti:Sapphire laser with a repetition rate of approximately 80 MHz. Since the exciton lifetime in the bulk semiconductor is much shorter than within the QD, a few picoseconds after the end of the pulse only the exciton within the QD remains. The exciton within QD subsequently recombines radiatively. By using a photodiode connected to the output of the laser as a reference signal, the time difference between a laser pulse and QD emission can be recorded. The probability of the exciton occupying the QD as a function of time can be determined by building up a histogram over many events. From the resulting histogram the radiative lifetime can be extracted. For an ideal two level system a single exponential decay is observed, however if there is

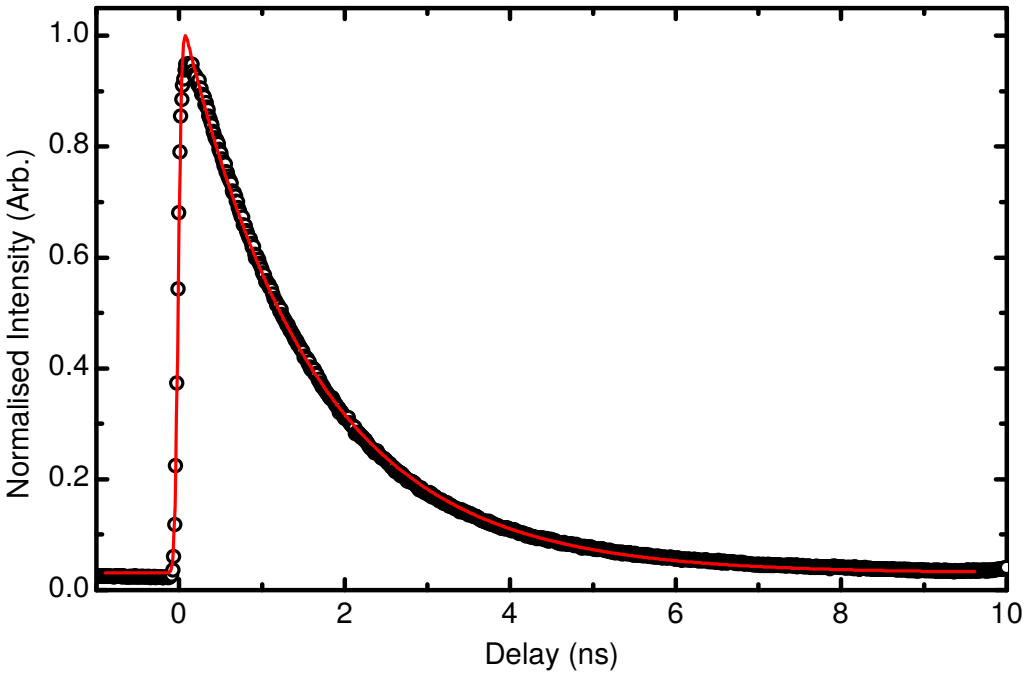

Figure 3.13 – Typical lifetime measurement using time-resolved microphotoluminescence spectroscopy. Experimental data is presented as open black circles and the red line corresponds to a fit using a exponentially modified Gaussian.

a non-radiative decay process it may exhibit double-exponential decay. The results of a typical lifetime measurement for a QD with a lifetime of 1.55 ns is shown in Figure 3.13.

Although the SPCM itself is able to measure time differences down to 12 ps, the single-photon avalanche diodes (SPADs) used to detect single photons have a jitter time of approximately 400 ps. This must be taken into account when fitting the data by using an exponentially modified Gaussian.

Additionally the SPCM has a dead time of 100 ns after receiving a start signal. Since the laser has a repetition rate of 80 MHz, 88 % of start signals will be missed. The majority of these events contain zero photons from the QD as the count rate is typically less than 100 kHz. To avoid this, the module operates in a reversed start-stop mode where the time between a photon arriving and the next excitation pulse is measured instead. This allows the module to operate with a much lower start frequency and is thus able to measure almost all events.

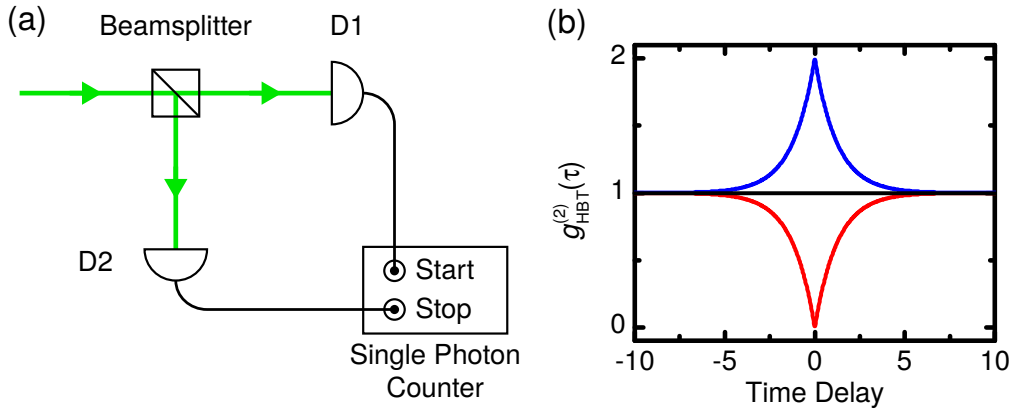

Figure 3.14 – a) Experimental arrangement for a Hanbury Brown and Twiss measurement. b) Example $g^{(2)}_{HBT}$ functions for a coherent source (black), bunched source (blue) and an antibunched source (red).

3.4.4.2 Hanbury Brown and Twiss

Many applications of quantum optics require an antibunched single-photon source i.e. the emission is sub-Poissonian. This differs to laser light and thermal sources which are Poissonian (random interval) and super-Poissonian (bunched) respectively. The degree of bunching or antibunching can be quantified with the second order correlation function $g^{(2)}_{HBT}(\tau)$. The second order correlation function is measured with a Hanbury Brown and Twiss (HBT) experiment, depicted in Figure 3.14a. In a HBT measurement, light is incident upon a 50:50 beamsplitter and directed to two SPADs. The output pulses from the two detectors are used as start and stop signals on the SPCM. A photon arriving at detector D1 starts a timer and a photon at D2 stops it. These events are accumulated by the SPCM which then produces a histogram of the time intervals. For this measurement system the second order correlation function can be written as

$$g^{(2)}_{HBT}(\tau) = \frac{\langle n_1(t)\, n_2(t+\tau)\rangle}{\langle n_1(t)\rangle \langle n_2(t+\tau)\rangle}$$

where $n_i(t)$ is the number of counts registered at detector i at time t. The angled brackets $\langle \dots \rangle$ denote time averaged values.

For antibunched sources, where the incoming stream of photons consists of single photons with a large time interval between them, the photons will be randomly directed to either detector. Since only a single photon is present at a time,

obtaining a start detection event at D1 implies a zero probability of detecting a photon at the stop detector D2. Therefore no coincidences at $\tau = 0$ will be recorded. At longer time scales, the next photon in the stream has a 50 % probability of triggering a stop event at D2. If the photon instead arrives at D1, then nothing happens and the process is repeated until a stop event occurs. Therefore for a perfectly antibunched source $g^{(2)}_{HBT}(\tau = 0) = 0$ and at long timescales $\lim_{\tau\to\infty} g^{(2)}_{HBT}(\tau) = 1$.

Perfectly coherent sources have a random time interval between photons. This means that the probability of obtaining a stop pulse is independent of τ giving $g^{(2)}_{HBT}(\tau) = 1$ for all τ. Bunched sources on the other hand consist of, as the name implies, a stream of photons where the photons are bunched together. Therefore if a photon is detected there is a much higher probability that another photon will be detected on a short timescale than a long timescale. Hence at short timescales $g^{(2)}_{HBT} > 1$, tending towards $g^{(2)}_{HBT} = 1$ at long timescales. An example of the second order correlation function obtained for each of these classifications is shown in Figure 3.14b.

In practice the measured $g^{(2)}_{HBT}(\tau = 0)$ of an antibunched source never reaches zero due to a combination of two factors. One factor is extra counts which originate both from stray light and dark counts, giving rise to a non-zero probability of detecting a stop event at zero delay. The main contribution is due to measurements involving very short timescales which are comparable to the timing jitter of the detection system, effectively smoothing the measurement results.

This measurement technique can also be used to investigate correlations between light from different sources or different lines from a single source[110]. For this type of measurement no beam splitter is needed, instead the two light sources are directed onto separate SPADs and the coincidences recorded as described previously.

3.4.4.3 Jitter Time

Due to the short timescales involved in TCSPC measurements the jitter time of the detection system can have a significant influence upon the measurements. If the jitter time is known, the majority of the effect of the error can be removed by either deconvolving the data or convolving the fitting function with the detector response. Typically the fitting function is convolved with the detector response

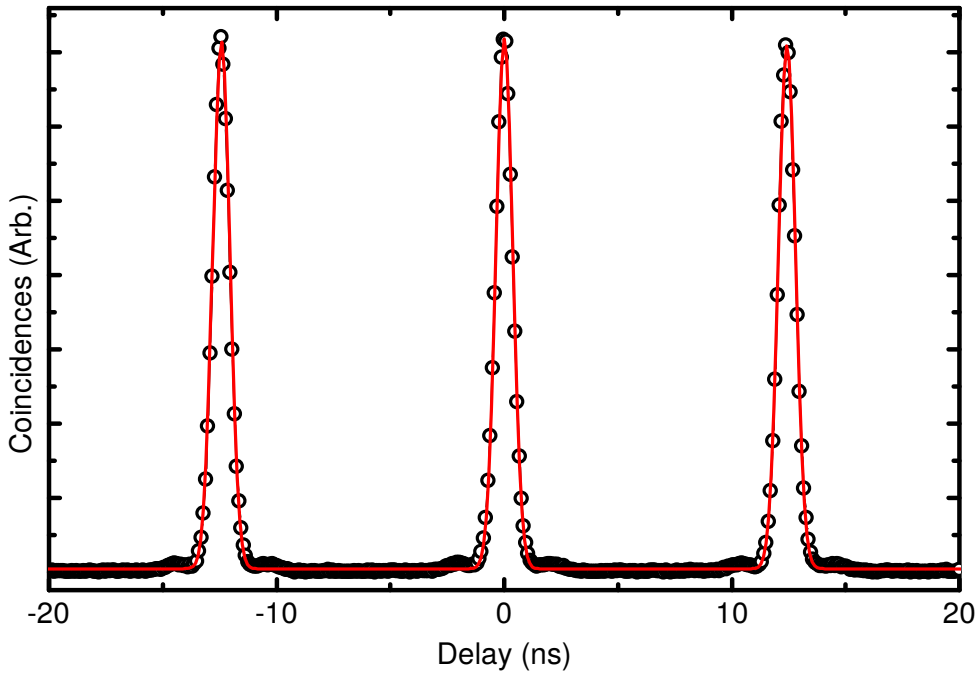

Figure 3.15 – Jitter time measurement for HBT experimental arrangement. The width of the fitted lines corresponds to the jitter time of the system

to avoid the effect of the extra noise present in the measurement data. Although the jitter time is given by the manufacturer of the SPADs, the quoted value is measured under ideal conditions which are difficult to reproduce in the laboratory and cannot factor in temporal broadening due to the optical setup (e.g. multi-mode fibres). Furthermore some have noted a large variance between identical specification SPAD modules[111].

The jitter time can be accurately determined with a femtosecond pulsed laser. For single detector measurements, the optical setup is similar to that of a lifetime measurement but with the SPAD directly detecting laser emission instead of the sample's emission. As the duration of the pulsed laser is significantly shorter than the jitter time it may be considered a delta function. Therefore any broadening of the line in the resulting histogram must be entirely due to the the detector response. For two-channel measurements the detector response can be obtained by performing a pulsed HBT measurement on the laser. An example of a typical HBT type jitter measurement is shown in Figure 3.15.

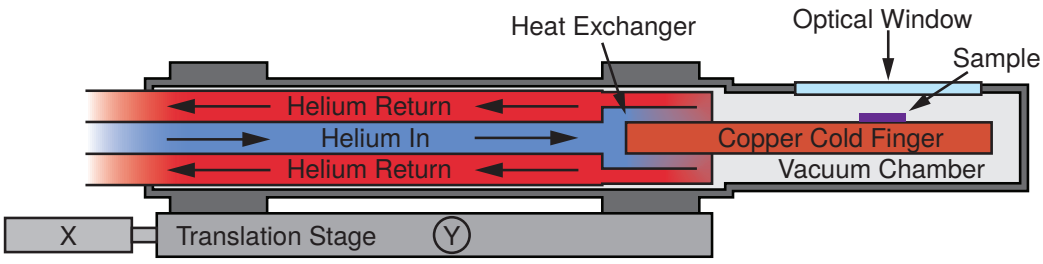

Figure 3.16 – Schematic diagram of a continuous flow cryostat.

3.4.5 Cryostats

All of the experiments presented in this thesis were performed at a temperature of approximately 5 K. To achieve these temperatures the samples were placed within a cryostat cooled by liquid helium. Two different types of cryostat were used for this purpose, each with its own advantages and disadvantages.

3.4.5.1 Continuous Flow Cryostat

Within a continuous flow cryostat, the sample is mounted upon a copper cold finger within a vacuum chamber. The cold finger provides thermal contact between the sample and a heat exchanger. Liquid helium is continuously pumped through the heat exchanger to bring the sample temperature down to approximately 5 K. Typically the temperature is higher than that of liquid helium due to radiative heating from the warm chamber walls. A glass window in the top of the vacuum chamber provides optical access to the sample. Coarse adjustments to sample position can be made with the manual translation stages the cryostat is mounted upon. Finer adjustments, and focus, can be made by moving the optics above. A schematic of the cryostat is shown in Figure 3.16.

The main advantage of a continuous flow cryostat is the ability to rapidly load and measure samples. Any more detailed measurements requiring long integration times and/or high stability cannot be performed due to vibrations (originating from the pump and helium flow) compromising the stability of the system.

The optical arrangement used with the cryostat is shown in Figure 3.17. Emission from a HeNe laser and/or white light lamp source is focused onto the sample with a 50x objective lens. Emission from the sample is collected through the same objective lens and passed into a single mode optical fibre. The emis-

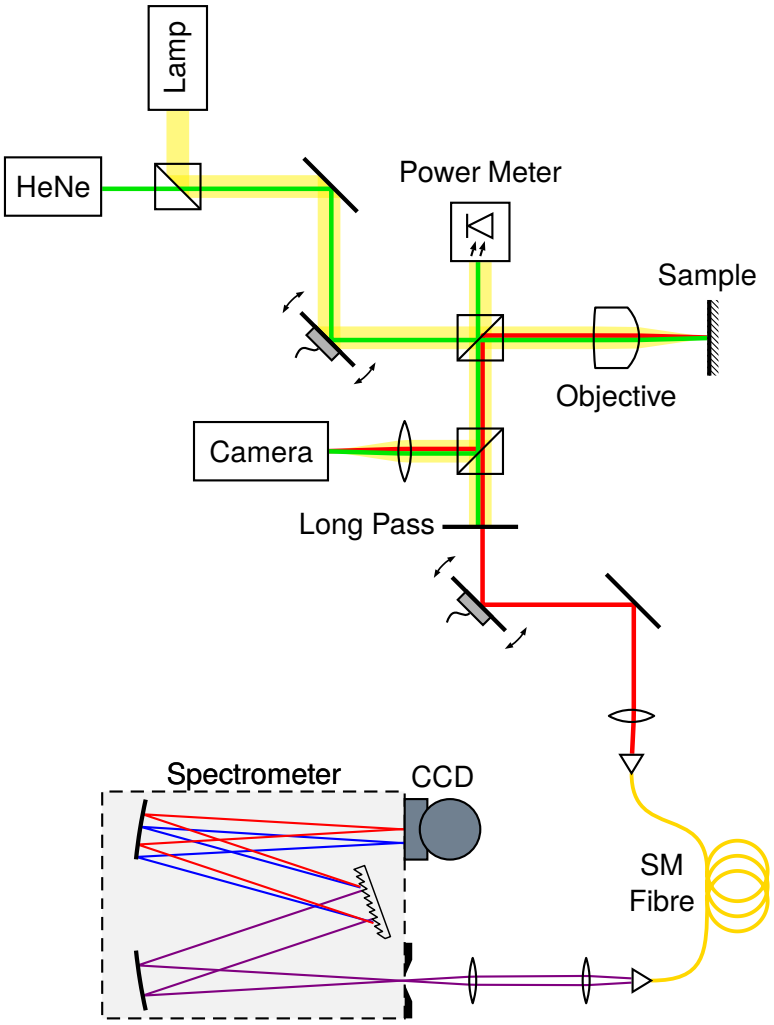

Figure 3.17 – Schematic of the optical setup used for all measurements in a flow-cryostat.

sion is filtered and recorded with a 0.3 m spectrometer and charge-coupled device (CCD) camera. Two servo scanning mirrors allow the excitation and collection spots to be scanned across the sample. An additional complementary metal-oxide-semiconductor (CMOS) camera is used to image the sample.

3.4.5.2 Exchange Gas Cryostat

The long integration times required by many of the experiments in the subsequent chapters presented a considerable experimental challenge. To be able to perform these measurements the ability to maintain alignment and measure a

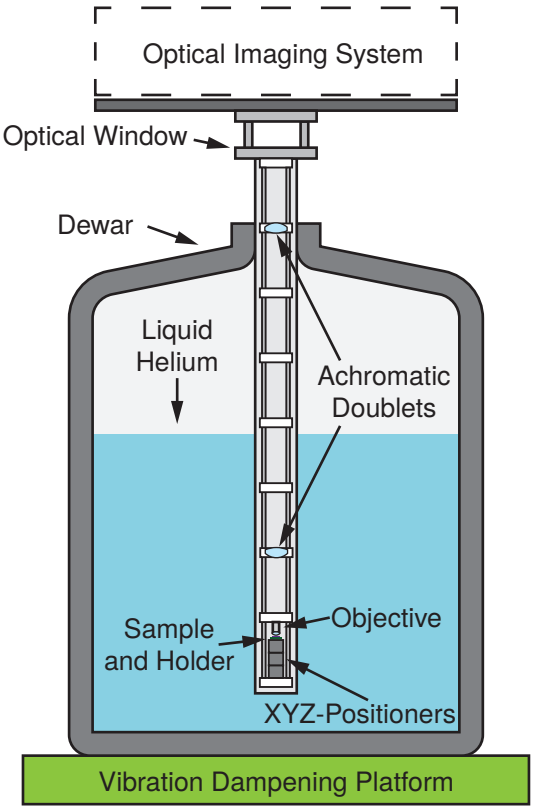

Figure 3.18 – Schematic diagram of the cold lens cryostat.

single quantum dot over a period of (up to) several days was required. This was achieved by designing an exchange gas cryostat system. Using such an approach provided a relatively simple stable mechanical system that allows the use of a standard high numerical aperture lens with a short working distance.

Figure 3.18 shows a schematic of the cryostat. The cryostat reaches low temperatures by immersing an evacuated tube containing the sample into a liquid helium dewar. A small amount of exchange gas is present to thermally couple the sample to the chamber walls and therefore to the liquid helium reservoir. Since the system does not require the use of a pump or any gas flow, no vibrations are generated and the system can maintain alignment on a single QD for two weeks before the helium dewar needs to be refilled.

Within the tube, the sample clips into a socket on a PCB. The PCB is then mounted upon custom machined titanium XYZ slip-stick piezoelectric translation stages with a 5mm travel to provide sample positioning and fine focus control.

Titanium was used as its low thermal expansion coefficient allows both room temperature and 5 K operation.

The lenses and sample holder are held in place with a 1.3 m long 30 mm cage system with several Thorlabs cage plates for stability. The outer anodised aluminium layer was removed from cage plates to reduce outgassing. Slots and clamps to hold electrical wires have been machined into the sides of the plates. At the top of the cage is a stainless steel head with a window for optical access, four 14-pin Fischer connectors for electrical access and a klein flange (KF) 50 vacuum connector. The entire cage system slots into a stainless steel tube sealing against the KF connector. The steel tube also has a KF25 connector to pump the system to vacuum and a pressure safety valve.

The tube is pumped down to below 10^{-5} mbar using a turbo-molecular pump and oil-free backing pump before approximately 50 mbar of helium exchange gas is added. The tube is then dipped into a dewar of liquid helium in order to cool the sample down to 4.2 K. Further stability is provided by standing the dewar on a floating platform in order to isolate the system from any vibrations in the building. The dewar is also overpressured relative to the helium return line to provide isolation from the variations in return gas flow that occur due to other cryostats operating in the building.

The optical arrangement is shown in Figure 3.19. A single, aspheric 0.55 numerical aperture (NA) objective lens is used to focus the excitation laser into a 1–2 µm spot on the sample. Emission from the sample is collected with the same lens. NA requirements prevented the use of an achromatic lens and cost prohibited the use of a low temperature microscope objective. Two 25.4 mm, f =40 cm achromatic doublets mounted in the tube in a $4f$ configuration are used to increase the scanning range of the microscope without beam distortion. On top of the tube, above the optical window, a breadboard is mounted. Upon the breadboard there are four single-mode fibre coupled paths: two excitation and two collection paths. Each of these paths can be independently scanned with servo scanning mirrors. A fifth path is used for white light imaging.

Spectra were recorded by directing each of the output optical fibres into it's own 0.75 m spectrometer and CCD camera (17 µeV/pixel). For TCSPC measurements, the emission was filtered with the spectrometers and detected using two silicon SPADs.

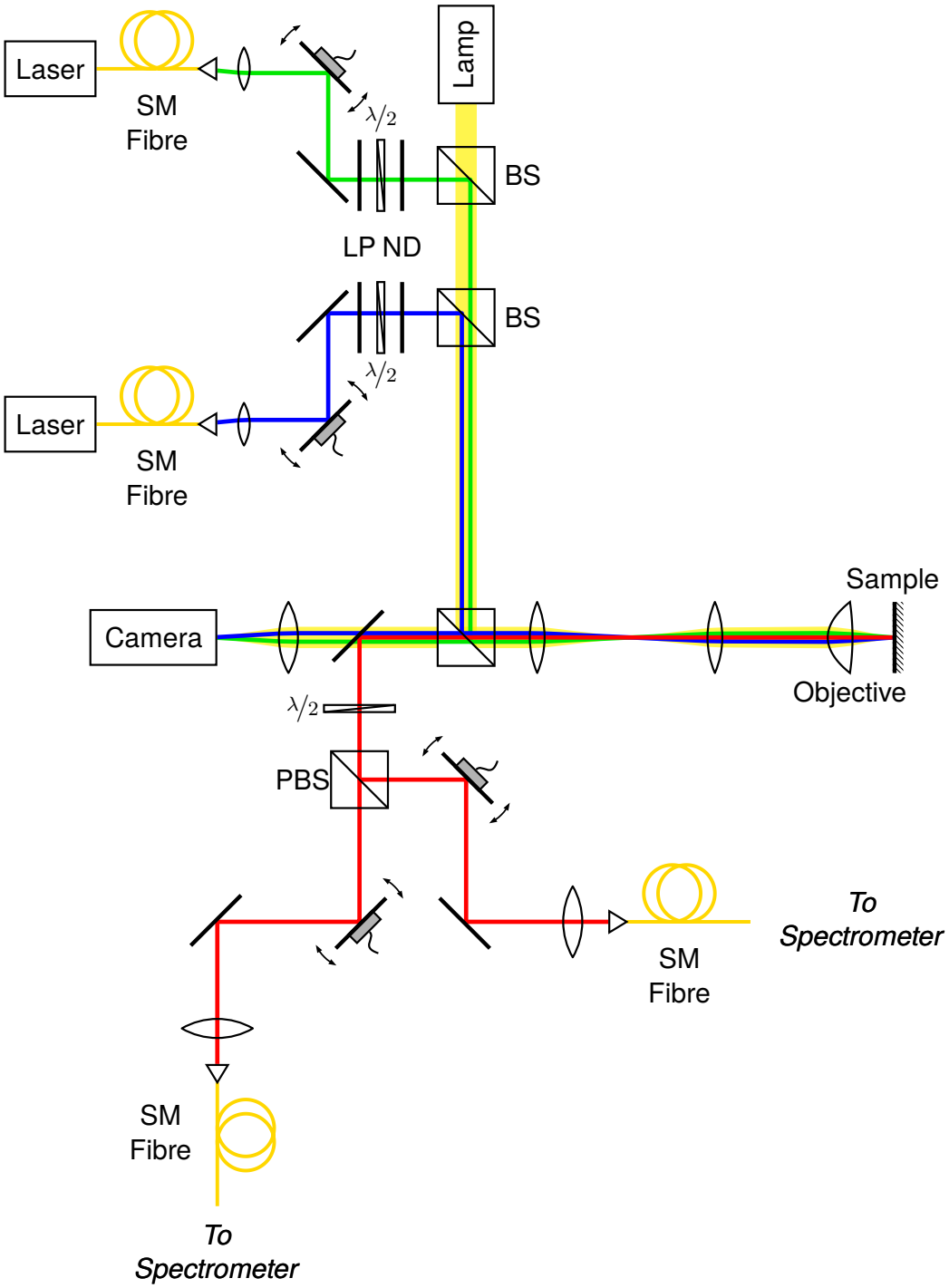

Figure 3.19 – Schematic of the optical setup used for all measurements in the exchange gas cryostat. Lasers are coupled in with SM fibres and polarisation control provided by LP and half-wave plates. The collection polarisation can be varied with the half-plate and PBS. Collected light is coupled to SM fibres and to two spectrometers and CCDs or SPADs.

References

[45] A. Zrenner, "A close look on single quantum dots", The journal of chemical physics **112**, 7790–7798 (2000) (see pp. 9, 28).

[78] A. Taflove, S. C. Hagness et al., "Computational electrodynamics: the finite-difference time-domain method", Norwood, 2nd Edition, MA: Artech House, l995 (1995) (see p. 25).

[79] A. F. Oskooi, D. Roundy, M. Ibanescu, P. Bermel, J. D. Joannopoulos and S. G. Johnson, "Meep: A flexible free-software package for electromagnetic simulations by the FDTD method", Computer Physics Communications **181**, 687–702 (2010) (see pp. 25, 57).

[80] *Lumerical Solutions, Inc. http://www.lumerical.com/tcad-products/fdtd/* (see pp. 25, 79).

[81] S. Johnson and J. D. Joannopoulos, "Block-iterative frequency-domain methods for Maxwell's equations in a planewave basis", Opt. Express **8**, 173–190 (2001) (see p. 25).

[82] *Lumerical Solutions, Inc. http://www.lumerical.com/tcad-products/mode/* (see pp. 25, 95).

[83] R. Nötzel, "Self-organized growth of quantum-dot structures", Semiconductor Science and Technology **11**, 1365 (1996) (see p. 26).

[84] A. Cho and J. Arthur, "Molecular beam epitaxy", Progress in solid state chemistry **10**, 157–191 (1975) (see p. 26).

[85] I. Stranski and L. Krastanow, "Abhandlungen der mathematisch-naturwissenschaftlichen klasse IIb", Akademie der Wissenschaften Wien **146**, 797–810 (1938) (see p. 26).

[86] E. Bauer, "Phänomenologische theorie der kristallabscheidung an oberflächen. II", Zeitschrift für Kristallographie-Crystalline Materials **110**, 395–431 (1958) (see p. 26).

[87] L. Goldstein, F. Glas, J. Y. Marzin, M. N. Charasse and G. Le Roux, "Growth by molecular beam epitaxy and characterization of InAs/GaAs strained-layer superlattices", Applied Physics Letters **47**, 1099 (1985) (see p. 26).

[88]R. Asaro and W. Tiller, "Interface morphology development during stress corrosion cracking: Part I. Via surface diffusion", Metallurgical Transactions **3**, 1789–1796 (1972) (see p. 26).

[89]M. A. Grinfeld, "Instability of the separation boundary between a non-hydrostatically stressed body and a melt", Sov. Phys. Dokl. **31**, 831–834 (1986) (see p. 26).

[90]M. Bayer, G. Ortner, O. Stern, A. Kuther, A. A. Gorbunov, A. Forchel, P. Hawrylak, S. Fafard, K. Hinzer, T. L. Reinecke, S. N. Walck, J. P. Reithmaier, F. Klopf and F. Schäfer, "Fine structure of neutral and charged excitons in self-assembled In(Ga)As/(Al)GaAs quantum dots", Physical Review B **65** (2002) 10.1103/PhysRevB.65.195315 (see p. 28).

[91]S. Golka, C. Pflügl, W. Schrenk and G. Strasser, "Quantum cascade lasers with lateral double-sided distributed feedback grating", Applied Physics Letters **86**, 111103 (2005) (see pp. 30, 31).

[92]R. Shul, G. McClellan, R. Briggs, D. Rieger, S. Pearton, C. Abernathy, J. Lee, C. Constantine and C. Barratt, "High-density plasma etching of compound semiconductors", Journal of Vacuum Science & Technology A **15**, 633–637 (1997) (see p. 31).

[93]R. Braive, L. Le Gratiet, S. Guilet, G. Patriarche, A. Lemaître, A. Beveratos, I. Robert-Philip and I. Sagnes, "Inductively coupled plasma etching of GaAs suspended photonic crystal cavities", Journal of vacuum science & technology B **27**, 1909–1914 (2009) (see p. 31).

[94]M. Balooch, D. Olander and W. Siekhaus, "The thermal and ion-assisted reactions of GaAs (100) with molecular chlorine", Journal of Vacuum Science & Technology B **4**, 794–805 (1986) (see p. 31).

[95]E. Hu and R. Howard, "Reactive ion etching of GaAs in a chlorine plasma", Journal of Vacuum Science & Technology B **2**, 85–88 (1984) (see p. 31).

[96]S. Golka, S. Schartner, W. Schrenk, G. Strasser et al., "Low bias reactive ion etching of GaAs with a SiCl4/N-2/O-2 time-multiplexed process", Journal of Vacuum Science & Technology B **25**, 839–844 (2007) (see p. 31).

[97]S. Golka, M. Arens, M. Reetz, T. Kwapien, S. Bouchoule and G. Patriarche, "Time-multiplexed, inductively coupled plasma process with separate SiCl4 and O2 steps for etching of GaAs with high selectivity", Journal of Vacuum Science & Technology B **27**, 2270–2279 (2009) (see p. 31).

[98]P. Kumar, S. Kanakaraju and D. DeVoe, "Sacrificial etching of AlxGa1-xAs for III–V MEMS surface micromachining", Applied Physics A **88**, 711–714 (2007) (see p. 31).

[99]A. Cohen, "Critical point drying-principles and procedures", Scanning electron microscopy, 303–24 (1979) (see p. 31).

[100]R. Heitz, M. Veit, N. N. Ledentsov, A. Hoffmann, D. Bimberg, V. M. Ustinov, P. S. Kop′ev and Z. I. Alferov, "Energy relaxation by multiphonon processes in InAs/GaAs quantum dots", Physical Review B **56**, 10435 (1997) (see p. 39).

[101]N. H. Bonadeo, J. Erland, D. Gammon, D. Park, D. Katzer and D. Steel, "Coherent optical control of the quantum state of a single quantum dot", Science **282**, 1473–1476 (1998) (see p. 40).

[102]C. Santori, D. Fattal, J. Vučković, G. S. Solomon and Y. Yamamoto, "Indistinguishable photons from a single-photon device", Nature **419**, 594–597 (2002) (see p. 40).

[103]S. Sauvage, P. Boucaud, R. Lobo, F. Bras, G. Fishman, R. Prazeres, F. Glotin, J. Ortega and J.-M. Gérard, "Long polaron lifetime in InAs/GaAs self-assembled quantum dots", Physical review letters **88**, 177402 (2002) (see p. 40).

[104]E. Zibik, L. Wilson, R. Green, G. Bastard, R. Ferreira, P. Phillips, D. Carder, J. R. Wells, M. Skolnick, J. Cockburn et al., "The polaronic nature of intraband relaxation in InAs/GaAs self-assembled quantum dots", Physica E: Low-dimensional Systems and Nanostructures **26**, 408–412 (2005) (see p. 40).

[105]K. Kuroda, T. Kuroda, K. Watanabe, T. Mano, K. Sakoda, G. Kido and N. Koguchi, "Final-state readout of exciton qubits by observing resonantly excited photoluminescence in quantum dots", Applied physics letters **90**, 051909 (2007) (see p. 40).

[106] A. Muller, E. B. Flagg, P. Bianucci, X. Y. Wang, D. G. Deppe, W. Ma, J. Zhang, G. J. Salamo, M. Xiao and C. K. Shih, "Resonance Fluorescence from a Coherently Driven Semiconductor Quantum Dot in a Cavity", Physical Review Letters **99** (2007) 10.1103/PhysRevLett.99.187402 (see p. 40).

[107] E. Siebert, T. Warming, A. Schliwa, E. Stock, M. Winkelnkemper, S. Rodt and D. Bimberg, "Spectroscopic access to single-hole energies in InAs/GaAs quantum dots", Physical Review B **79** (2009) 10.1103/PhysRevB.79.205321 (see p. 40).

[108] T. Warming, E. Siebert, A. Schliwa, E. Stock, R. Zimmermann and D. Bimberg, "Hole-hole and electron-hole exchange interactions in single InAs/GaAs quantum dots", Physical Review B **79** (2009) 10.1103/PhysRevB.79.125316 (see p. 40).

[109] Y. Benny, Y. Kodriano, E. Poem, D. Gershoni, T. A. Truong and P. M. Petroff, "Excitation spectroscopy of single quantum dots at tunable positive, neutral, and negative charge states", Physical Review B **86** (2012) 10.1103/PhysRevB.86.085306 (see p. 40).

[110] H. Nakajima, H. Kumano, H. Iijima, S. Odashima and I. Suemune, "Carrier-transfer dynamics between neutral and charged excitonic states in a single quantum dot probed with second-order photon correlation measurements", Physical Review B **88** (2013) 10.1103/PhysRevB.88.045324 (see pp. 44, 115).

[111] I. Rech, I. Labanca, M. Ghioni and S. Cova, "Modified single photon counting modules for optimal timing performance", Review of Scientific Instruments **77**, 033104 (2006) (see p. 45).

Chapter 4

Waveguide-Coupled H1 Cavities for Single Photon Routing

Individual self-assembled quantum dots (QDs) are ideal as on-demand single-photon sources due to their highly favourable optical properties and ease of integration with existing mature fabrication technology. The ability to distribute QD single-photon emission in a circuit is key to the progression of photonic quantum information technology. Whilst the distribution of quantum light on a semiconductor chip has been reported[112–114], control has not yet been demonstrated. The ability to control photon routing at the point of generation would represent an important step forward in the development of semiconductor-based quantum photonic integrated circuits. As photonic circuits become more complex, requiring many single-photon sources, the advantage of being able to reuse a single source by redirecting its emission to different parts of the circuit becomes apparent.

In this chapter, a proof of concept experimental demonstration of an electrically controllable on-chip optical router using a single self-assembled QD as an emitter is presented. The voltage-controllable routing of emission from a single QD in a photonic crystal (PhC) membrane with an H1 cavity and two W1 waveguides is demonstrated. The membrane is fabricated from a p-i-n diode. By changing voltage, the dot emission can be tuned across the cavity modes due to the quantum-confined Stark effect (QCSE). In doing so, the QD emission can be selectively directed into one of two waveguides, enabling voltage-controllable optical routing. This preferential channelling is observed when, at a specific voltage, the

dot emission is in resonance with the mode coupled to that waveguide.

4.1 Device Design

The approach utilised here to achieve on-chip photon routing is based upon an H1 cavity in a hexagonal PhC membrane, illustrated in Figure 4.1[115]. There are two fundamental dipole modes in an H1 cavity, nominally degenerate, but the degeneracy is lifted due to fabrication imperfections. The small mode volume of H1 cavities facilitates efficient coupling of the emission from incorporated QDs to the cavity modes. In addition, two line-defect W1 waveguides are incorporated in the PhC, providing two distinct propagation channels. Selective coupling of each of the cavity modes to its respective waveguide is accomplished by waveguide orientation in the crystal. In this case, photons can be directed into one of two propagation channels, dependent on which cavity mode they are coupled to.

In Ref. [115], ensemble photoluminescence (PL) from incorporated QDs provided a photon source. For optical quantum information applications however, single-photon emission from individual QDs is needed. For efficient coupling, a single-dot emission line should be on resonance with a cavity mode. In order to control the resonance conditions, tuneability of either the cavity modes or the QD emission, or both, is required. Moreover, the tuneability should be fast, controllable, easily reversible, and achievable at low power without affecting other parts of the electronic and photonic circuitry. Tuning the QD emission by varying the electric field satisfies these criteria, in contrast to other methods, such as gas deposition[116] or temperature variation[61]. In the presence of an electric field, the QD emission energy changes due to the QCSE[117]. The electric field can be varied in a PhC membrane fabricated from a p-i-n diode, which constitutes a technological challenge. However, successful development of PhC membranes with electrically tuneable QD emission has been reported[118].

4.2 Theory

Figure 4.1 shows a schematic diagram of the device design. A hexagonal PhC membrane incorporates an H1 cavity and two W1 waveguides, denoted by X and Y, at 120° to one another. The design was optimised by Dr. Rikki Coles

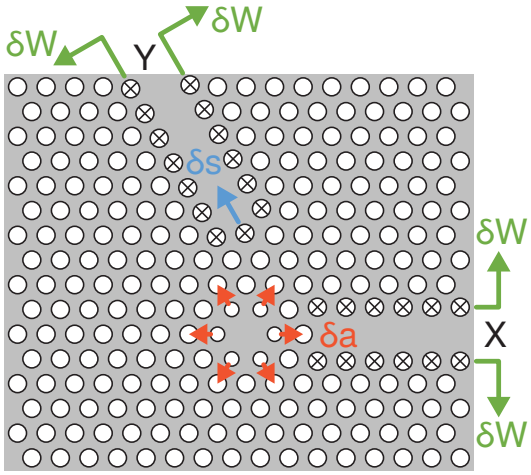

Figure 4.1 – Schematic diagram of the PhC design, showing the H1 cavity and two W1 waveguides, X and Y. In order to optimise device performance, the holes adjacent to the waveguides and cavity are displaced as indicated by arrows. In addition the radius of the holes adjacent to the cavity is reduced.

using finite-difference time-domain (FDTD) computational modelling (details are available in Ref. [115]) with MEEP[79]. The relationship between the PhC slab height, $h = 200\,\mathrm{nm}$, and the period, a, was selected as $h = 0.85a$ (i.e., $a = 236\,\mathrm{nm}$); the hole radius, r, varied between $0.31a$ and $0.34a$ (i.e., between 73 nm and 80 nm). This ensured that the fundamental cavity modes spectrally coincide with the QD ground-state emission. To maximise the cavity Q-factor, the ring of holes adjacent to the cavity centre was displaced by $\delta a = 0.091a$ away from the cavity (shown by arrows in Figure. 4.1) with a reduced hole radii of $0.091a$[119]. The separation between the cavity and the waveguides was chosen to provide efficient selective coupling without significantly compromising the cavity Q-factor. The waveguides were designed such that each of them sustains a single propagating transverse-electric (TE)-like mode in the spectral range of the QD emission. The first rows of holes in each waveguide were displaced laterally by $\delta W = 0.08a$ so that the cavity modes do not coincide with the cut-off region of the waveguides; in addition, the first hole in the Y-waveguide was displaced away from the cavity by $\delta s = 0.08a$.

Figure 4.2 shows the results of FDTD modelling, which illustrate how photon routing is achieved. The modelling was performed for a device with $r = 0.31a$ (73 nm). One should note that for our approach, it is essential that the fundamental modes in the H1 cavity are not degenerate. To lift the degeneracy in the model, an additional vertical displacement of two pairs of holes immediately above and

below the cavity was introduced by $\delta a = 0.02a$ away from the cavity. Figure 4.2a presents the resulting cavity mode spectra, which were calculated from analysis of the decay transients of cavity fields using a method of harmonic inversion of time signals[120]. The unpolarised spectrum reveals two mode peaks split by 2.5 nm shown in Figure 4.2a.

Notations X and Y, which are used for the W1 waveguides, reflect the orientation (at the cavity centre) of the H_z dipole for a cavity mode, which is coupled to a respective waveguide. These modes are referred to as X- and Y-dipole modes. Figures 4.2b and 4.2c show calculated H_z profiles for the non-degenerate X- and Y-dipole modes, respectively. The modes selectively couple to their corresponding waveguides. The polarised spectra in Figure 4.2a, calculated using x- and y-polarised dipole sources, demonstrate that the longer-wavelength (x-polarised) and shorter-wavelength (y-polarised) peaks correspond, respectively, to the Y- and X-dipole modes.

To quantify the strength of the cavity-waveguide coupling, Q-factors were calculated for each mode in three different configurations: an uncoupled cavity (i.e., with no waveguides), Q_U; only a co-polarised waveguide, Q_{Co}; and with only a cross-polarised waveguide present, Q_{Cross}. The Q-factors represent the loss rates in each case[121]. From that the loss rates into each waveguide and the strengths of co-coupling, $\eta_{Co} = (Q_{Co}^{-1}\text{–}Q_U^{-1}) \cdot Q_{Tot}$, and cross-coupling, $\eta_{Cross} = (Q_{Cross}^{-1}\text{–}Q_U^{-1}) \cdot Q_{Tot}$, where $Q_{Tot} = (Q_{Co}^{-1} + Q_{Cross}^{-1}\text{–}Q_U^{-1})^{-1}$ is the Q-factor in case of both waveguides present, can be calculated. The calculated values of η_{Co} and η_{Cross} are, respectively, 89.5% and 2.1% for the X-dipole mode and 87.0% and 0.6% for the Y-dipole mode. The modelling results suggest that the co-coupling strength can be expected to significantly exceed cross-coupling in our structures.

4.3 Experimental Arrangement

4.3.1 Sample Fabrication

A schematic diagram of the sample, grown using molecular beam epitaxy (MBE) on an undoped GaAs substrate, is shown in Figure 4.3a. A 200 nm thick p-i-n diode structure was grown on top of a 1 µm thick n-doped $Al_{0.6}Ga_{0.4}As$ sacrificial layer and a 1 µm thick n-doped GaAs contacting layer. The QD layer was sandwiched

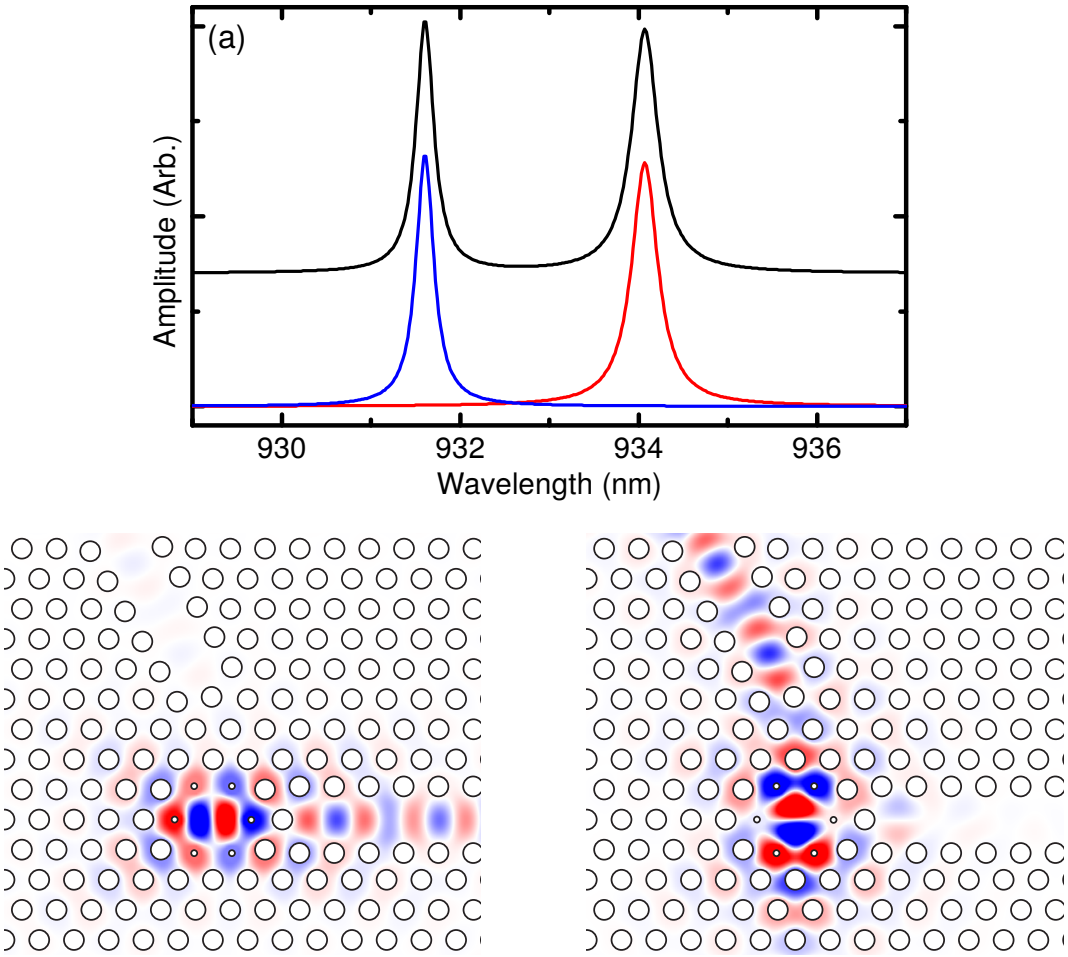

Figure 4.2 – Results of modelling for waveguide-coupled non-degenerate cavity modes. a) Cavity mode spectra for non-polarised, x- and y-polarised dipole sources (black, red, and blue, respectively) b) Normalised H_z profile for the X-dipole mode. A linear red-white-blue colour scale represents field strength in the range from −92 % to 92 %, with positive and negative values shown by red and blue, respectively. Magnitudes below −92 % and above 92 % are shown by saturated colours. c) The same as b) for the Y-dipole mode.

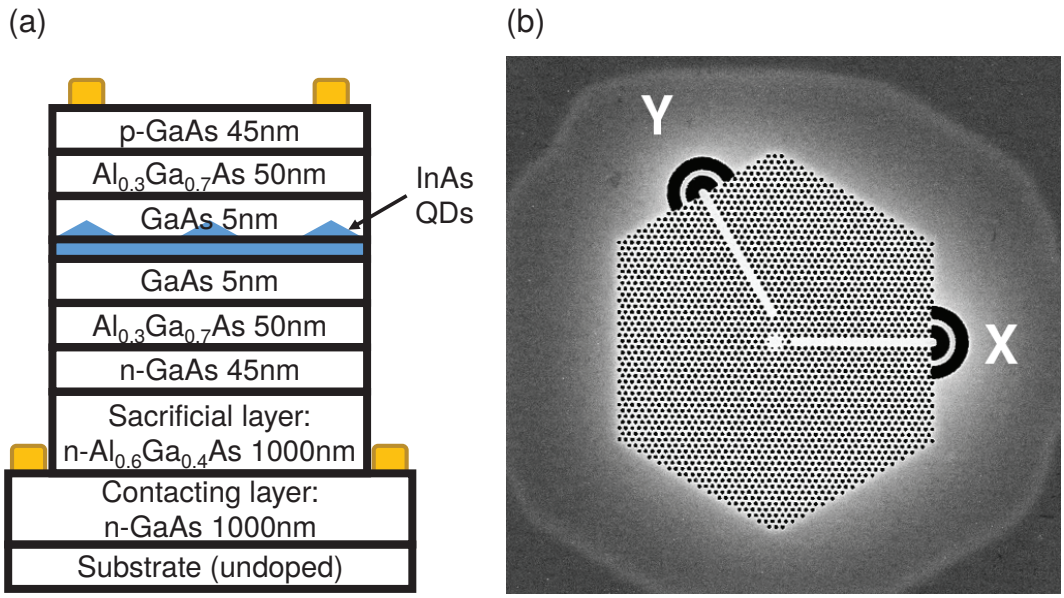

Figure 4.3 – a) Schematic diagram of the wafer layer structure. The contacts are shown by gold circles. b) SEM image of a typical photonic crystal membrane with an H1 cavity. X and Y denote the W1 waveguide terminated by out-couplers.

between 5 nm GaAs spacer layers, 50 nm $Al_{0.3}Ga_{0.7}As$ barriers, and a 45 nm Si-doped n-type GaAs contact layer at the bottom and a Be-doped p-type GaAs contact layer at the top of the diode structure. The barriers were introduced to suppress tunnelling out of carriers, enhancing the voltage tuning range over which QD emission could be observed [52]. The wafer was used to fabricate mesa diode devices of 400 µm diameter. Within each mesa, a number of suspended 200 nm thick PhC cavity membranes were fabricated using electron beam lithography (EBL) and inductively coupled plasma (ICP) etching, followed by etching away of the AlGaAs sacrificial layer in 40% hydrofluoric acid. The fabrication process is described in further detail in Sections 3.2.2 and 3.2.3. Each hexagonal PhC incorporated an H1 cavity and two W1 waveguides at 0° and 120°, which were terminated with Bragg out-couplers to redirect emission out of plane and into the collection optics. A scanning electron microscope (SEM) image of a typical PhC membrane is shown in Figure 4.3b.

The wafer was grown by Dr Edmund Clarke and the sample fabricated by Dr Benjamin Royall.

4.3.2 Experimental Apparatus

Optical characterisation with spatially resolved excitation and collection were performed in a continuous-flow liquid He cryostat using a confocal microscope (described in Section 3.4.5.1). HeNe laser excitation was provided to the cavity using a 50x microscope objective and focused to a spot of 1–2 µm diameter. Emission was collected selectively either from the cavity or from one of the waveguide out-couplers, using the same objective and a single-mode optical fibre of 4.7 µm core diameter. The emission was filtered and imaged by a 30 cm spectrometer and liquid N_2 cooled charge-coupled device (CCD).

4.4 Basic Characterisation

Current-voltage (IV) characteristics at 5 K are typical for a p-i-n diode showing clear rectifying behaviour with the current onset at a forward bias of approximately 1.1 V (Figure 4.4). This voltage is lower than expected for a planar GaAs diode, although in agreement with results reported in Ref. [118] it is most probably caused by the diode defects discussed in Section 3.3.1.

Under reverse bias, or at small forward bias, PL emission from the self-assembled quantum dots is typically not observed because the electric field causes photo-excited electrons and holes to tunnel out of the dot. At higher forward biases tunnelling out is suppressed, which leads to an increase of the QD PL emission. At high excitation power, ensemble dot emission is observed in reference spectra from unprocessed areas of the diodes. In the PhC structures, spectra collected from the cavities are dominated by cavity modes. To obtain information into the quality of the cavities and mode splitting, high power measurements were performed upon all 26 cavities. A typical splitting of the modes by 1–4 nm and a Q-factor of 400–1200 was observed. A histogram of the data is shown in Figure 4.5. Figure 4.6 shows a PL spectrum from one of the cavities at high excitation power. Two well pronounced cavity modes are observed at 899.3 nm and 901.7 nm. This PhC cavity has $r = 0.34a$ (80 nm), resulting in cavity modes that are blue shifted compared to the modelled spectra.

At low excitation power, exciton emission lines from individual QDs can be readily resolved in the cavity collected spectra, as demonstrated in Figure 4.7. As

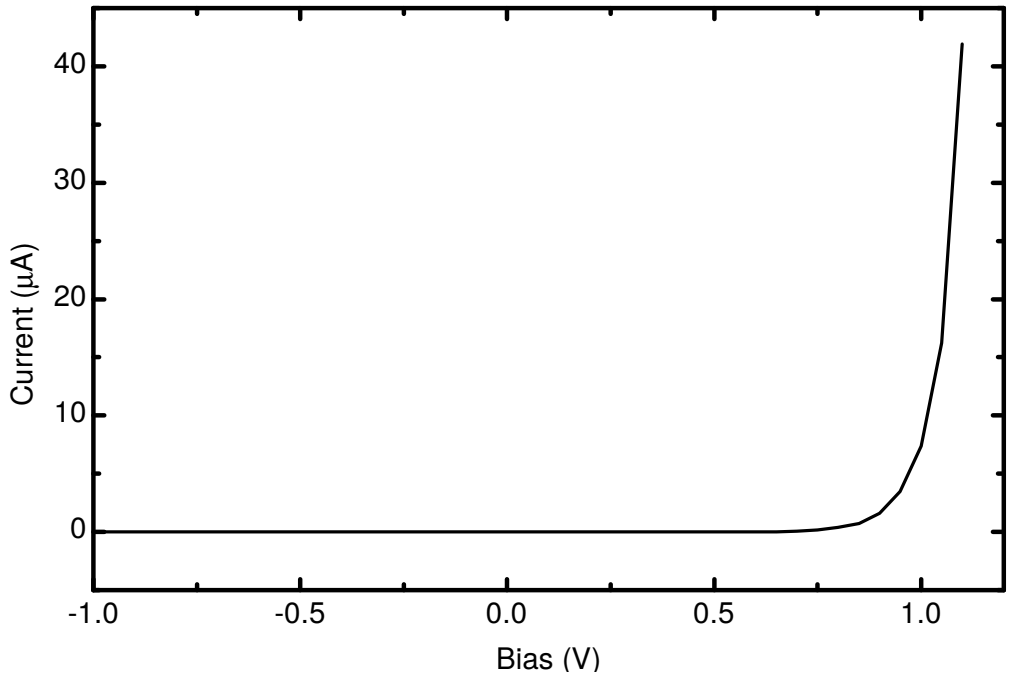

Figure 4.4 – Typical IV characteristic of a single mesa at 5 K.

the voltage is increased up to 1.1 V, the lines are blue shifted due to the QCSE. The typical range of the observed Stark shift is up to 5 nm, i.e., larger than the typical splitting of the cavity modes. It is worth noting that even when no individual dot emission lines are in resonance with the modes, the modes still dominate the cavity spectra at high excitation power due to cavity-feeding effects[122–124].

4.5 Routing of a Single Quantum Dot's Emission

Figure 4.7 shows a series of spectra from the same cavity as in Figure 4.6 at low excitation power at various voltages. For these measurements both the excitation laser and collection are positioned over the cavity. With voltage changing from 0.5 V to 1.0 V, a single-dot line (highlighted in the spectra) undergoes a blue shift from approximately 903 nm to 898 nm, crossing both modes. The width of the line is limited by the spectrometer.

Figures 4.8a and 4.8b show, respectively, the dot line wavelength and intensity as a function of voltage at the same power; horizontal dashed lines indicate wavelengths of the cavity modes, while vertical dashed lines indicate the corres-

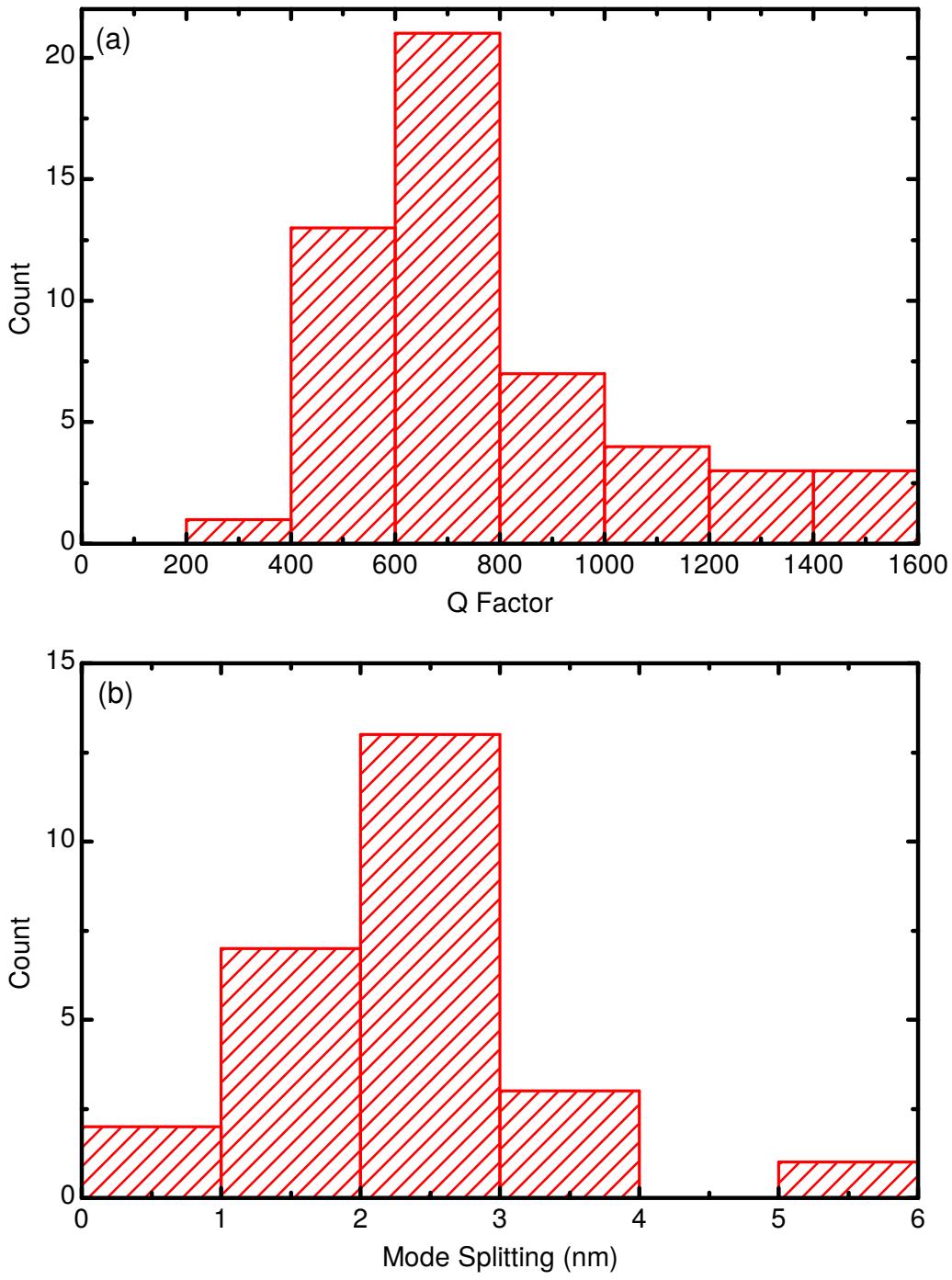

Figure 4.5 – Histograms of a) the cavity Q factor and b) the cavity mode splitting.

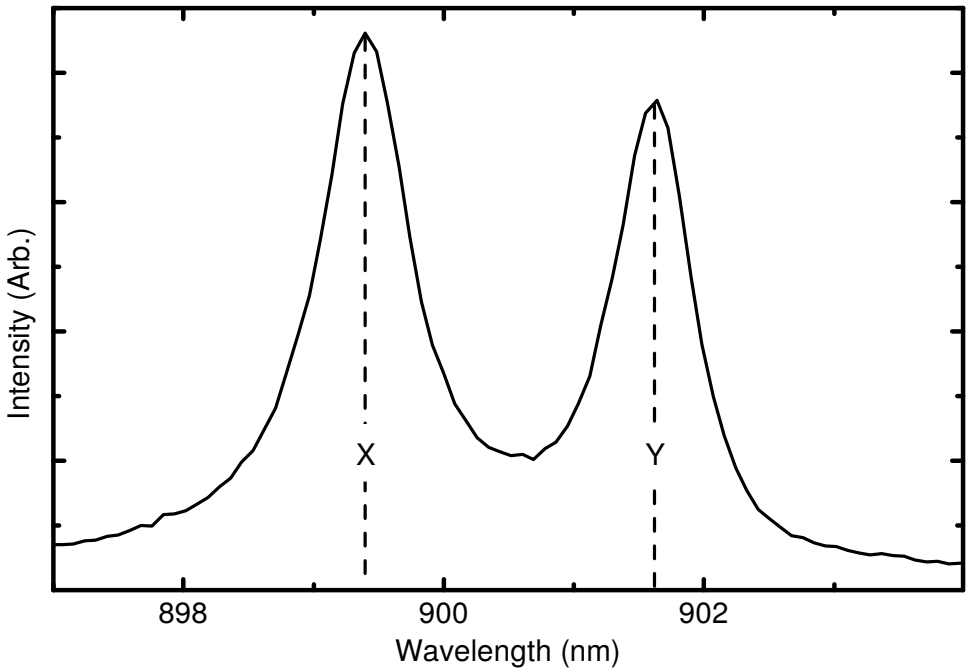

Figure 4.6 – Photoluminescence spectrum from the cavity at high excitation power (35 μW) and bias of 1.1 V. X and Y denote the X and Y dipole modes.

ponding voltages, 0.67 V and 0.88 V, respectively, at which the dot line is in resonance with either mode. One can see that at both resonances, clear intensity peaks are observed. These are due to two factors: a Purcell enhancement of the spontaneous emission[55, 118] and the preferential collection of the far-field emission from the cavity by the PL setup[125], i.e., in both cases due to coupling of the dot emission to the cavity modes in the weak coupling regime. The intensity at the lower-voltage resonance (901.7 nm) is smaller, most likely because a significant fraction of photo-excited carriers tunnel out of the QDs at this voltage, whilst at the higher-voltage resonance (899.3 nm), tunnelling out is suppressed. Although the exact location of the QD cannot be measured, the observation of QD PL and enhancement of the emission indicates the QD is located near to the cavity maximum. If the QD was further from the cavity, emission would be suppressed.

In order to demonstrate routing, the outputs of the out-couplers were measured using the same low excitation power. Emission from the same single dot is observed in the spectra collected from both out-couplers, whilst laser excitation is provided to the cavity. To verify this, the line positions are followed as a function of voltage in the spectra collected both from the cavity and each of

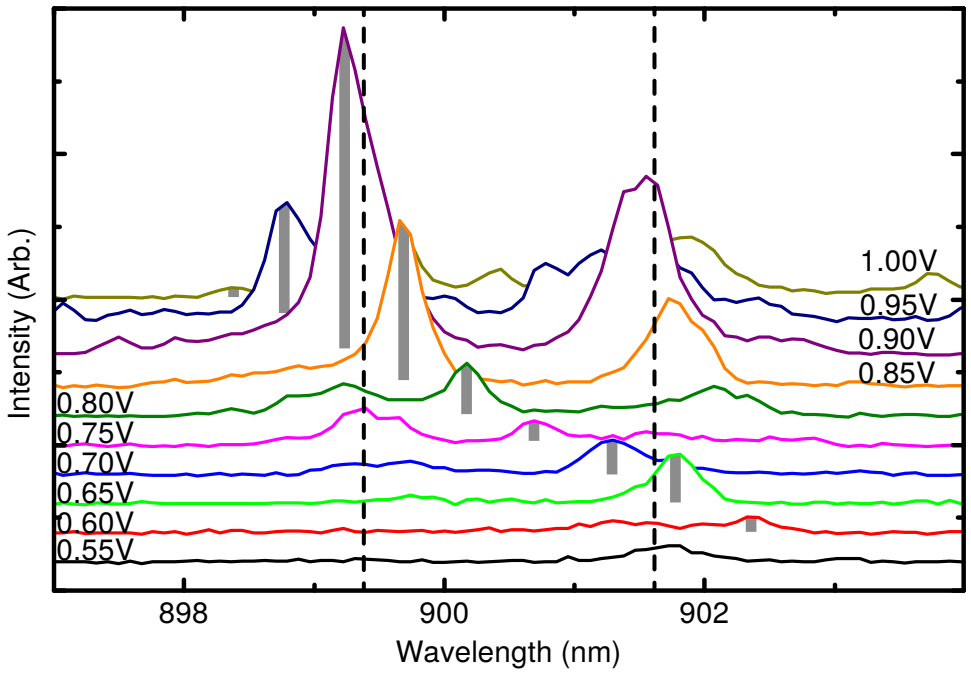

Figure 4.7 – Series of spectra at low excitation power (0.35 µW) at various biases. Each spectrum in the series are offset by 100 counts clarity. A single quantum dot peak which crosses both cavities is highlighted by grey vertical bars. Vertical dashed lines indicate the wavelengths of the cavity mode maxima

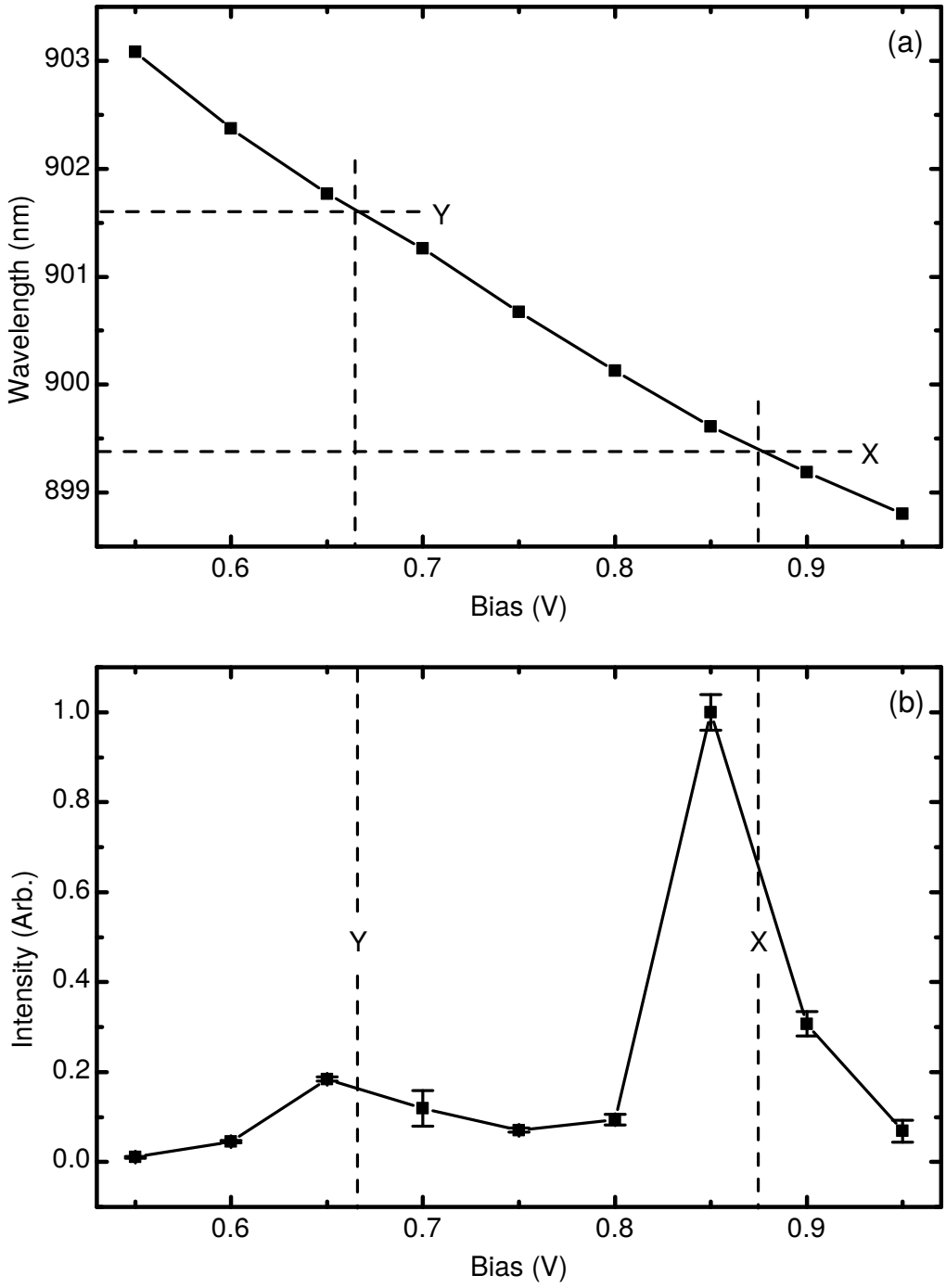

Figure 4.8 – Single-dot line a) wavelength and b) intensity as a function of bias in the spectra collected from the cavity. Solid lines are guides for the eye. Horizontal dashed lines indicate the wavelengths of the cavity X- and Y-mode maxima; vertical dashed lines indicate the voltage at which the QD line is observed at these wavelengths.

the out-couplers. These are presented in Figure 4.9a; it is clear that for the three collection geometries, the line positions coincide.

Figure 4.9b shows the intensity of the same QD line as a function of voltage for collection from the X and Y out-couplers. Results for cavity collection from Figure 4.8 are also presented for comparison. The plots are normalised to their respective maximum values. In absolute terms, the maximum emission intensity for the X out-coupler is approximately 5 times larger than for the Y out-coupler and is 10% of that for cavity collection. One can see that for collection from the X out-coupler, the line intensity peaks at the resonance with the X-mode at 899.3 nm. On the contrary, in the spectra collected from the Y out-coupler, the maximum intensity is observed at the resonance with the Y-mode at 901.7 nm, while at the resonance with the X-mode, the line almost vanishes, even though it is at its maximum value in the spectra collected from the cavity. Comparison of absolute values of intensities provides estimates of branching ratios (i.e., ratios of co-coupling to cross-coupling) at resonances with both modes. A branching ratio of 12:1 (X- to Y-waveguide) for the resonance with the X-mode and a ratio of 3:1 (Y- to X-waveguide) for that with the Y-mode was obtained. These ratios are significantly lower than predicted by theoretical calculations. This is most likely due to fabrication imperfections of the PhC membrane structures and Fabry-Perot modes in the waveguides. As the H1 cavity is small, any fabrication induced deviation from design can have a significant effect. Additionally, the out-couplers have a non-zero reflectivity resulting in the formation of a Fabry-Perot cavity between the out-coupler and H1 cavity. These modes can be observed in high power spectra exciting and collecting from an out-coupler. An example spectrum of these Fabry-Perot modes is shown in Figure 4.10.

These observations unambiguously demonstrate electrically controlled selective routing of single-dot emission to the waveguides. They provide convincing evidence that the mechanism of routing is based on a combination of two types of coupling: first, resonant coupling of single-dot emission to the cavity modes, which is tunable by means of the QCSE, and second, preferential coupling of the cavity modes to the respective waveguides, which is achieved by the PhC cavity design.

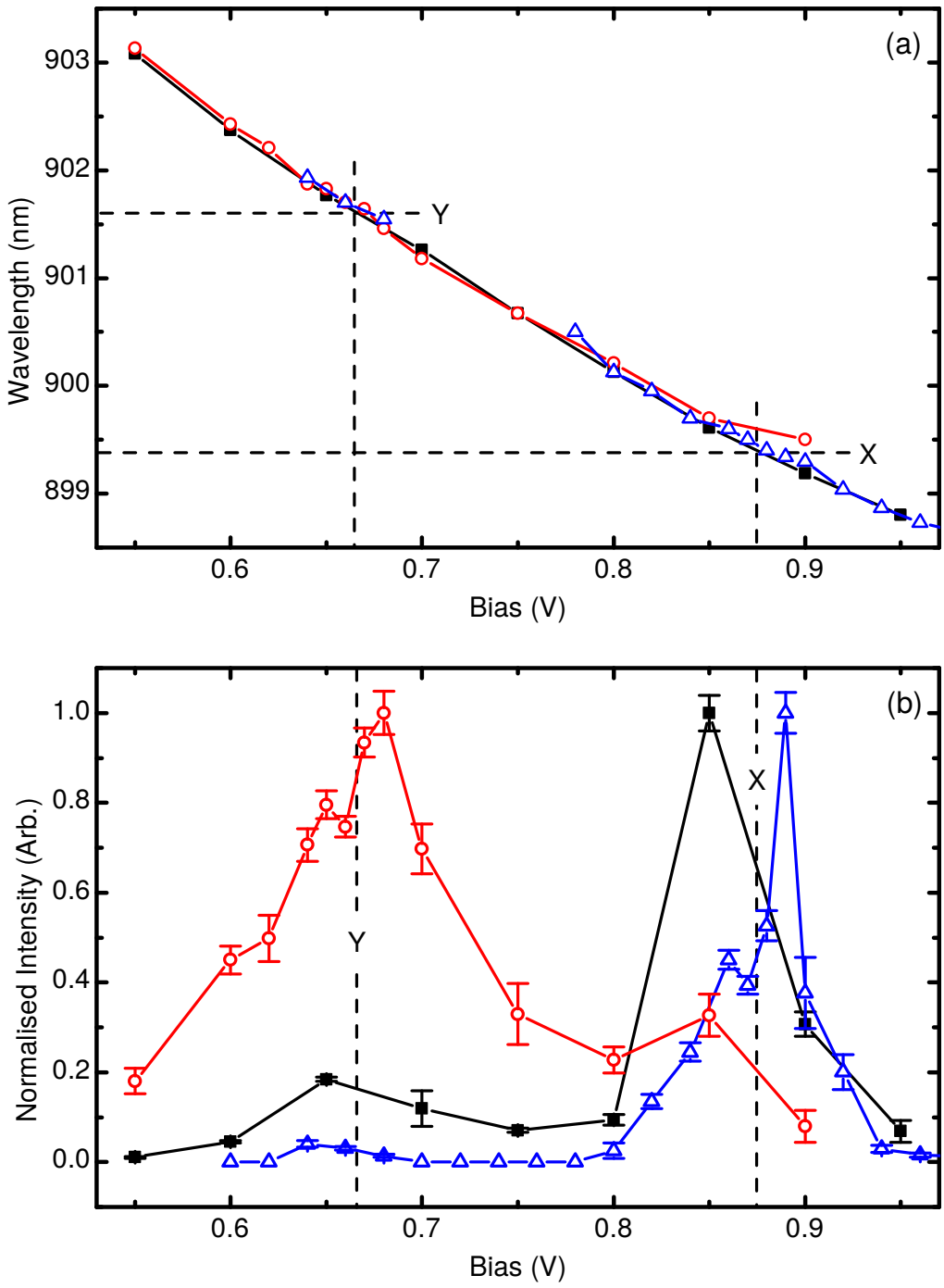

Figure 4.9 – Single-dot line a) wavelength and b) intensity as a function of bias in the spectra collected from the cavity, X and Y out-couplers (black squares, blue triangles and red circles, respectively). Solid lines are guides for the eye. Horizontal dashed lines indicate the wavelengths of the cavity X- and Y-mode maxima; vertical dashed lines indicate the voltage at which the QD line is observed at these wavelengths.

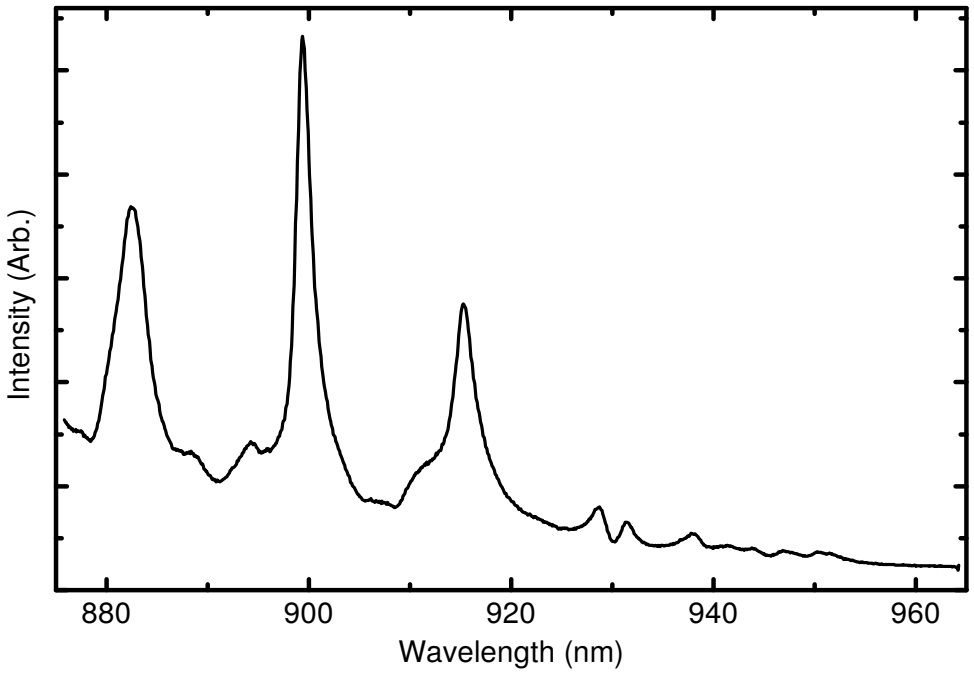

Figure 4.10 – Photoluminescence spectrum exciting and collecting from the out-coupler at high excitation power. Fabry-Perot modes dominate the spectra.

4.6 Summary and Outlook

In conclusion, the electrical control of on-chip routing of photons emitted by a single InAs/GaAs quantum dot has been demonstrated. The emission from a single quantum dot located inside an H1 photonic crystal cavity can be selectively coupled to either of two W1 waveguides by changing the bias. The proof of concept device provides the basis for scalable, low-power, high-speed operation of single-photon routers for use in integrated quantum photonic circuits.

References

[52] A. J. Bennett, R. B. Patel, J. Skiba-Szymanska, C. A. Nicoll, I. Farrer, D. A. Ritchie and A. J. Shields, "Giant Stark effect in the emission of single semiconductor quantum dots", Applied Physics Letters **97**, 1–4 (2010) (see pp. 11, 60).

[55]E. M. Purcell, "Spontaneous emission probabilities at radio frequencies", Physical Review B **69**, 681 (1946) (see pp. 13, 64).

[61]A. Kiraz, P. Michler, C. Becher, B. Gayral, A. İmamoğlu, L. Zhang, E. Hu, W. V. Schoenfeld and P. M. Petroff, "Cavity-quantum electrodynamics using a single InAs quantum dot in a microdisk structure", Applied Physics Letters **78**, 3932–3934 (2001) (see pp. 14, 56).

[79]A. F. Oskooi, D. Roundy, M. Ibanescu, P. Bermel, J. D. Joannopoulos and S. G. Johnson, "Meep: A flexible free-software package for electromagnetic simulations by the FDTD method", Computer Physics Communications **181**, 687–702 (2010) (see pp. 25, 57).

[112]A. Schwagmann, S. Kalliakos, I. Farrer, J. P. Griffiths, G. A. Jones, D. A. Ritchie and A. J. Shields, "On-chip single photon emission from an integrated semiconductor quantum dot into a photonic crystal waveguide", Applied Physics Letters **99**, 261108 (2011) (see pp. 55, 73).

[113]M. N. Makhonin, J. E. Dixon, R. J. Coles, B. Royall, I. J. Luxmoore, E. Clarke, M. Hugues, M. S. Skolnick and A. M. Fox, "Waveguide Coupled Resonance Fluorescence from On-Chip Quantum Emitter", Nano Letters **14**, 6997–7002 (2014) (see pp. 55, 73).

[114]S. Kalliakos, Y. Brody, A. Schwagmann, A. J. Bennett, M. B. Ward, D. J. P. Ellis, J. Skiba-Szymanska, I. Farrer, J. P. Griffiths, G. A. C. Jones, D. A. Ritchie and A. J. Shields, "In-plane emission of indistinguishable photons generated by an integrated quantum emitter", Applied Physics Letters **104**, 221109 (2014) (see pp. 55, 73).

[115]R. J. Coles, N. Prtljaga, B. Royall, I. J. Luxmoore, a. M. Fox and M. S. Skolnick, "Waveguide-coupled photonic crystal cavity for quantum dot spin readout", Optics Express **22**, 2376–2385 (2014) (see pp. 56, 57).

[116]S. Mosor, J. Hendrickson, B. C. Richards, J. Sweet, G. Khitrova, H. M. Gibbs, T. Yoshie, a. Scherer, O. B. Shchekin and D. G. Deppe, "Scanning a photonic crystal slab nanocavity by condensation of xenon", Applied Physics Letters **87**, 1–3 (2005) (see p. 56).

[117]P. W. Fry, I. E. Itskevich, D. J. Mowbray, M. S. Skolnick, J. J. Finley, J. a Barker, E. P. O'Reilly, L. R. Wilson, I. a Larkin, P. a Maksym, M. Hopkinson, M. Al-Khafaji, J. P. David, a. G. Cullis, G. Hill and J. C. Clark, "Inverted electron-hole alignment in InAs-GaAs self-assembled quantum dots.", Physical review letters **84**, 733–736 (2000) (see p. 56).

[118]A. Laucht, F. Hofbauer, N. Hauke, J. Angele, S. Stobbe, M. Kaniber, G. Böhm, P. Lodahl, M.-C. C. Amann and J. J. Finley, "Electrical control of spontaneous emission and strong coupling for a single quantum dot", New Journal of Physics **11**, 023034 (2009) (see pp. 56, 61, 64).

[119]M. Shirane, S. Kono, J. Ushida, S. Ohkouchi, N. Ikeda, Y. Sugimoto and A. Tomita, "Mode identification of high-quality-factor single-defect nanocavities in quantum dot-embedded photonic crystals", Journal of Applied Physics **101**, 073107–073107–7 (2007) (see p. 57).

[120]V. A. Mandelshtam and H. S. Taylor, "Harmonic inversion of time signals and its applications", The Journal of Chemical Physics **107**, 6756 (1997) (see p. 58).

[121]A. Faraon, E. Waks, D. Englund, I. Fushman and J. Vuckovic, "Efficient photonic crystal cavity-waveguide couplers", Appl. Phys. Lett. **90**, 73102 (2007) (see p. 58).

[122]M. Kaniber, A. Laucht, A. Neumann, J. M. Villas-Bôas, M. Bichler, M. C. Amann and J. J. Finley, "Investigation of the nonresonant dot-cavity coupling in two-dimensional photonic crystal nanocavities", Physical Review B - Condensed Matter and Materials Physics **77**, 1–4 (2008) (see p. 62).

[123]A. Badolato, M. Winger, K. J. Hennessy, E. L. Hu and A. İmamoğlu, "Cavity QED effects with single quantum dots", Comptes Rendus Physique **9**, 850–856 (2008) (see p. 62).

[124]M. Winger, T. Volz, G. Tarel, S. Portolan, A. Badolato, K. J. Hennessy, E. L. Hu, A. Beveratos, J. Finley, V. Savona and A. İmamoğlu, "Explanation of photon correlations in the far-off-resonance optical emission from a quantum-dot-cavity system", Physical Review Letters **103**, 11–14 (2009) (see p. 62).

[125]B. Gayral and J. M. Gérard, "Photoluminescence experiment on quantum dots embedded in a large Purcell-factor microcavity", Physical Review B - Condensed Matter and Materials Physics **78**, 1–7 (2008) (see p. 64).

Chapter 5

Single-Photon Electroluminescence for On-Chip Quantum Networks

The use of single photons as flying qubits in quantum networks[126] provides a platform for quantum computation[8] and the secure transfer of information[127] in scalable optical quantum information systems[10, 128]. For real-world applications, high component densities are likely to be required[15], which can be achieved using integrated semiconductor nano-photonic circuits. In addition, integrated optical circuits are inherently stable and dramatically reduce the experimental complexity[129]. A key requirement for this approach is a controllable on-chip single-photon source with favourable coherence properties. Moreover, if the source can be driven electrically, this provides an important advantage in terms of scalability.

Embedded semiconductor quantum dots (QDs) are very promising as on-chip light sources. Emission from single QDs has been demonstrated with both optical[24, 130–132] and electrical excitation[133], and the single-photon nature of the emission[32, 34, 35, 37, 38] has been established. The integration of QDs with circuit elements such as waveguides[112–114] and beamsplitters[134] has also been demonstrated. However, all experiments on integrated single-photon sources so far have relied on external optical excitation. Although this has the benefit of limiting the emission to QDs within the excitation spot, such an approach becomes increasingly challenging for networks requiring multiple single-photon sources. By contrast, electrical injection is a viable method of creating a true on-chip source of single photons. However, to limit the number of emitting QDs in

this case is a challenge.

This chapter firstly presents, and justifies experimentally, the challenges associated with using electroluminescence (EL) and possible solutions to these problems before moving onto an experimental demonstration of the on-chip spatially selective electrical generation of single photons and their coupling into a suspended nanobeam waveguide. In this device, the photons are generated by electrical injection into self-assembled QDs. Emission from only a few QDs located within a small area at the end of the waveguide, where coupling to the waveguide mode is strong, is used to produce a waveguide-coupled single-photon EL source. The results show high photon coherence values comparable with the best reported for diode structures[135, 136] suggesting that the proximity of the doped layers and surfaces in the present devices does not necessarily have a significant impact on device performance under EL conditions. The coherence properties are in principle sufficient to observe non-classical interference which is a key requirement for linear optical quantum computing (LOQC).

5.1 Wafer Design

Perhaps the most obvious, and basic, requirement for EL emission is that a diode structure is needed. The wafer must form either a p-i-n or p-n diode with a layer of QDs sandwiched between the p- and n-doped regions. Only p-i-n diodes are considered in this chapter as the intrinsic region allows the dopants to be separated from the QDs, helping to maintain good dot emission characteristics. Although this may be all that is required for EL emission, the requirements for a narrow single QD EL emission in a membrane sample are much more stringent as well as being different to those for a photoluminescence (PL) optimised sample.

A good example of this can be seen by comparing a p-i-n wafer optimised for quantum-confined Stark effect (QCSE) PL tuning, which has a 50 nm $Al_{0.3}Ga_{0.7}As$ tunnelling barrier either side of the QD in the intrinsic region, and a p-i-n wafer without any barriers. The structure of these samples is illustrated in Figure 5.1. Figure 5.2 shows EL emission from each of these wafers. The emission from the sample containing barriers has a much larger emission linewidth than that from the sample without barriers. In PL however, the linewidth of the emission from each is limited by the spectrometer.

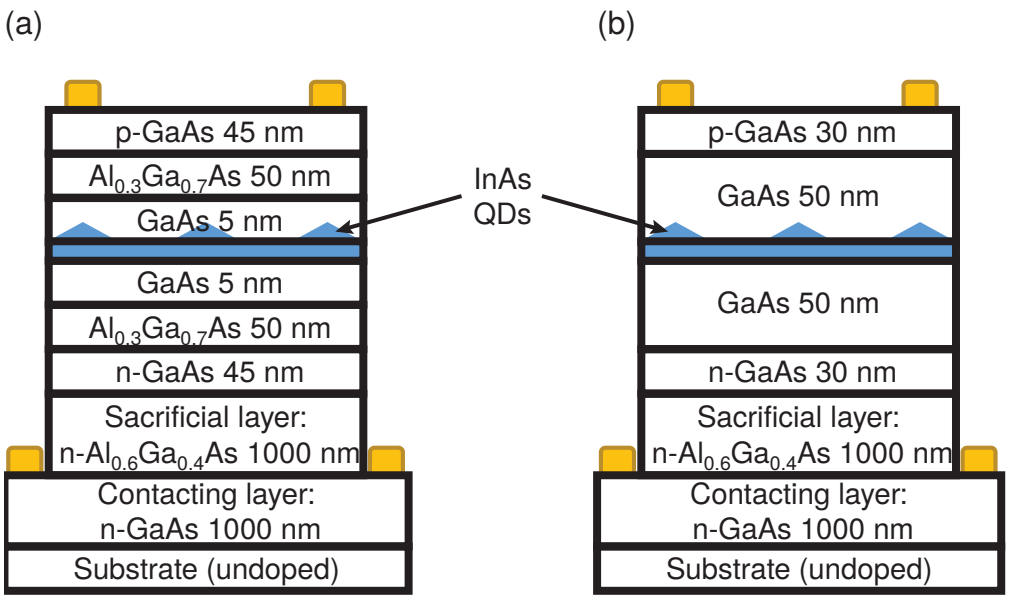

Figure 5.1 – Schematic diagram of two wafers used in the comparsion. a) A p-i-n wafer with two 50 nm $Al_{0.3}Ga_{0.7}As$ tunnelling barriers designed for optimal QCSE tuning in photoluminescence and b) a p-i-n wafer without barriers.

The cause of the striking difference in emission linewidth can be determined using bias dependent PL measurements. The emission from the sample without barriers shows three distinct emission regimes (Figure 5.3a). At small forward bias (less than 1.40 V) no emission is observed as the large built-in electric field sweeps the photo-generated carriers out of the QDs before recombination can occur. As the bias is increased the electric field decreases resulting in the onset of PL emission. A small QCSE shift of less than 0.2 nm is also observed. At 1.55 V the onset of EL occurs. No significant change in PL linewidth is observed over this range.

The emission from the barrier sample however shows four emission regimes (Figure 5.3b). Similar to the sample without barriers, no emission is observed at a small bias. The onset of PL occurs at a lower voltage (0.7 V) due to the barriers reducing the probability of the generated electron and hole pair tunnelling out of the QD before radiative recombination can occur. After the onset of PL a large QCSE tuning range of several nanometres is observed due to the presence of tunnelling barriers. In contrast to the sample without barriers, an abrupt change in emission linewidth occurs at 1.4 V. This is most likely due to electrons tunnelling through the barriers from the contact region filling the wetting layer. The resultant

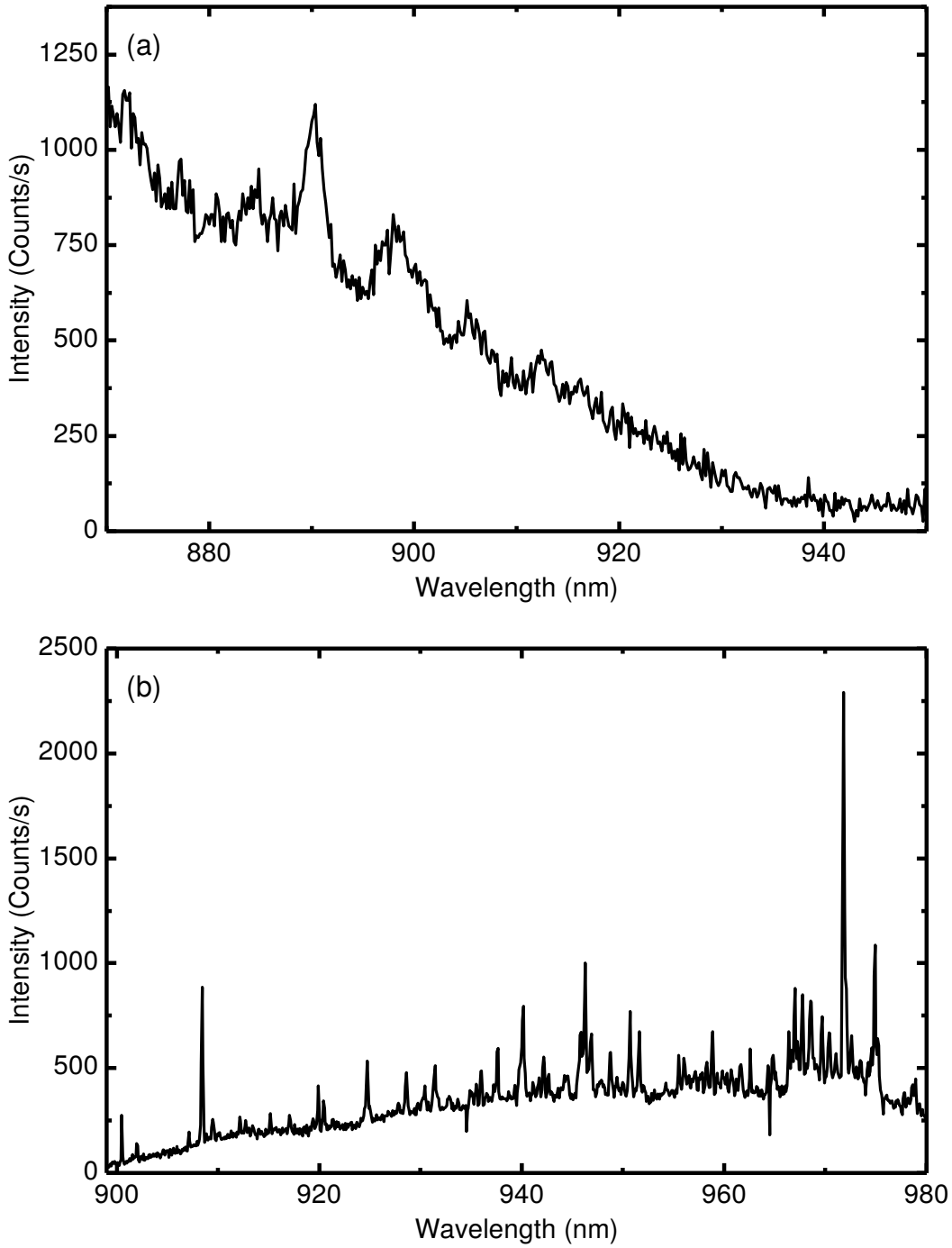

Figure 5.2 – Electroluminescence emission spectrum from a p-i-n sample a) with 50 nm tunnelling barriers and b) no barriers. A large difference in linewidth is observed in contrast to PL where both are spectrometer limited.

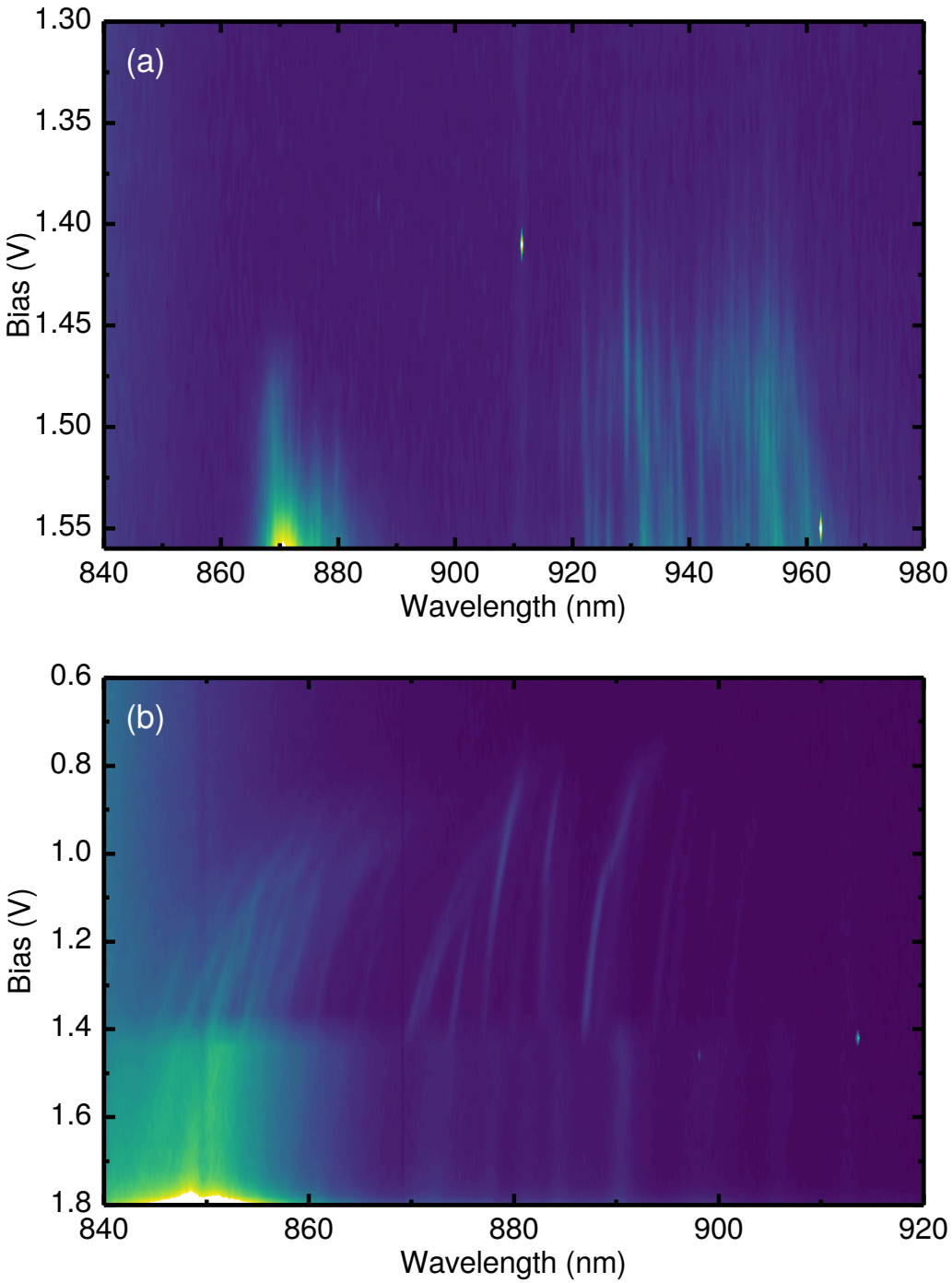

Figure 5.3 – Photoluminescence emission spectra as a function of applied bias for a sample with a) no barriers and b) symmetric 50 nm barriers. Colourmap corresponds to emission intensity with blue and red/white representing weak and bright emission intensities, respectively. The sample with barriers shows a large QCSE tuning range as charge carriers are prevented from escaping the QD. As the bias is increased to 1.4 V the tunnelling rate increases resulting in the wetting layer filling with electrons, degrading the linewidth of the QD emission. EL onset occurs at 1.8 V as holes tunnel in. The sample without barriers however shows no degradation of emission linewidth as the electrons and holes tunnel in at the same rate.

build up of charges near the QDs causes the lines to shift and broaden. Upon reaching 1.75 V holes are able tunnel through the barrier resulting in the onset of EL.

This brings us to the key requirement for an EL wafer; that both the electrons and holes tunnel into the quantum dot at the same rate for any voltage. This can be achieved in several different ways, one of which is to remove any tunnelling barriers so that the flow of charge carriers is unrestricted. The disadvantage of this method is that these wafers generally have unfavourable properties in PL and if any QCSE tuning is observed, the range is very small (few QD linewidths at most). Another method is to introduce two asymmetric barriers where the tunnelling rate difference due to carrier effective mass is compensated by barrier thickness. This allows the creation of a sample with a large tuning range as well as showing favourable emission characteristics in PL and EL. A slightly different approach is to design the barriers such that the charge carriers are able to resonantly tunnel into a single quantum dot[47, 137–139]. With such an approach it is possible to achieve excitation of only a single or a few QDs, unlike the other techniques where all biased QDs are excited. Unfortunately this is also the most difficult to achieve, most likely requiring a series of wafer growths.

For the work presented in this chapter a sample without barriers was chosen for its simplicity. The sample consists of a 160 nm thick GaAs p-i-n structure grown on top of a 1 µm thick $Al_{0.6}G_{0.4}As$ sacrificial layer. A layer of InAs self-assembled QDs was grown in the middle of the diode. The dot layer is sandwiched between 50 nm GaAs spacer layers and a 30 nm Be-doped p-type layer on the top and a 30 nm Si-doped n-type layer at the bottom of the diode structure.

5.2 Device Design

Figure 5.4 presents a schematic and a scanning electron microscope (SEM) image of a typical device. It consists of an electrically contacted bar (horizontal on the image) running perpendicular to three suspended waveguides. Semi-circular air/GaAs grating output couplers[140] at the opposite end of the waveguides scatter light into the detection apparatus. The 15 µm long waveguides have a height of 160 nm (which is the thickness of the p-i-n structure) and width of 290 nm; the dimensions were chosen to ensure single-mode operation in transverse-electric (TE)

polarisation. The electrical connection across the device is broken by a masked etch through the top p-type contact layer, including 30 nm deep notches across two of the three waveguides (the third waveguide is used as a control). This is done to limit the EL emission to the area at the bottom edge of the waveguide and to prevent emission from the remaining part of the device; in particular, the notches prevent emission from most of the waveguide's area and from the out-couplers.

Figure 5.5a illustrates how propagation of EL down a waveguide from only a single, or a few QDs is achieved. It shows the simulated electric field intensity profile of the optical mode which interfaces the waveguide and membrane. It was obtained by directly exciting the waveguide mode with an eigenmode source and monitoring the electric field intensity in the QD plane[80]. These simulations were performed by Dr Rikki Coles. The intensity at a given point is a measure of the coupling strength of the emission of the QD at that location to the mode. This is confirmed in Figure 5.5b which shows a comparison between mode intensity and the coupling strength of a dipole source at the same location. One can see that the coupling is efficient only for QDs either within the waveguide or close to the bottom edge of the waveguide, and rapidly diminishes as the emitter is moved further from the waveguide. With a notch across the waveguide, which provides an electrical break, an effective excitation area of approximately 0.5 μm^2 can be expected.

5.3 Experimental Arrangement

5.3.1 Sample Fabrication

The samples were fabricated following the procedure outlined in Sections 3.2.2 and 3.2.3. Two variations upon the isolation method were produced, one with a 2 µm length notch in the waveguide and one with almost the entire length of waveguide etched. Each mesa contains 10 sets of waveguides with the distance between the notch and end of the waveguide varied between each set.

5.3.2 Experimental Apparatus

Optical measurements were performed in a helium exchange gas cryostat based confocal microscope system with four independent optical paths. A complete

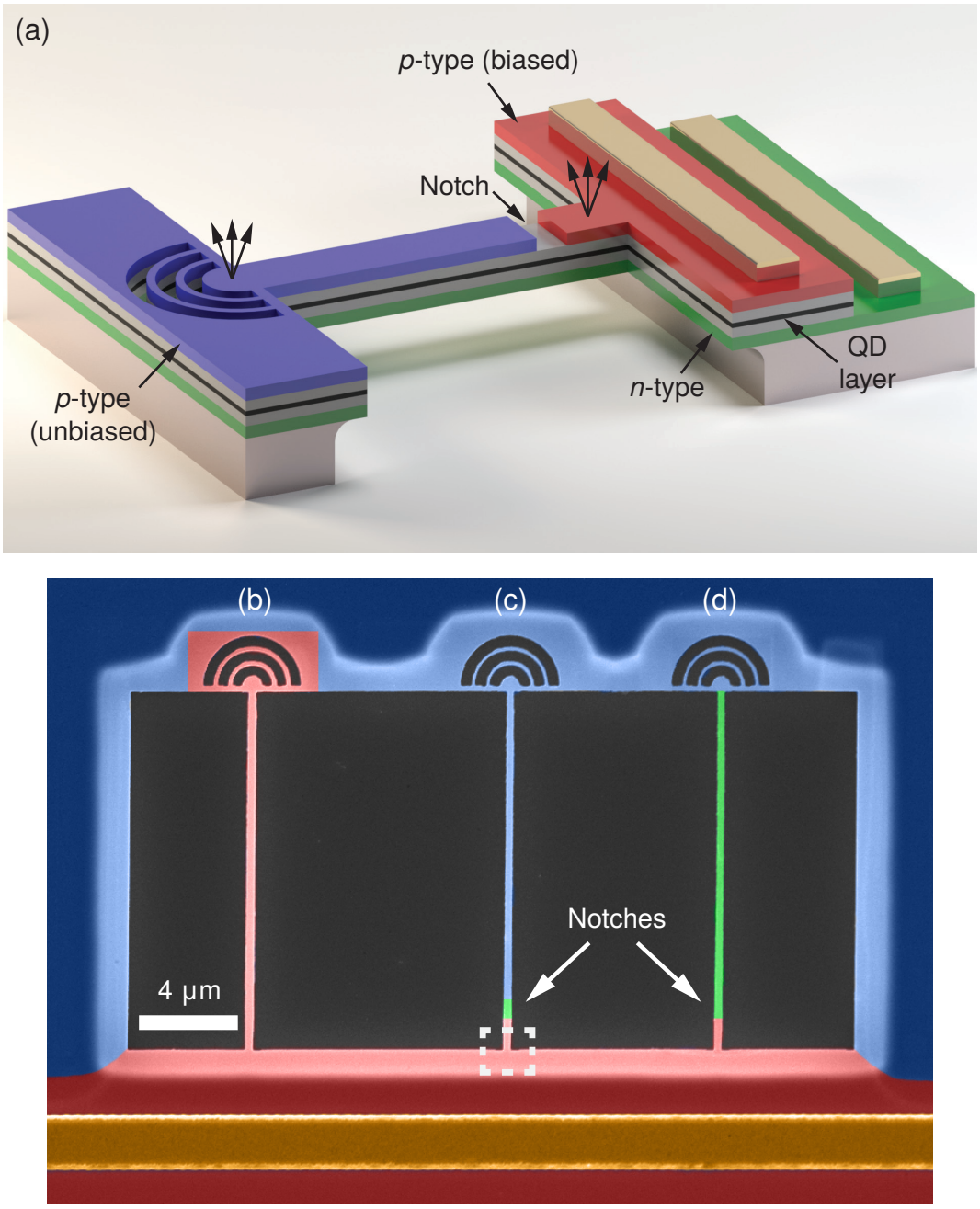

Figure 5.4 – a) Schematic of the device design. Only one of the three waveguide is shown. Red and blue colours represent biased and unbiased regions of the sample, respectively. They are separated by a notch which breaks electrical connection in the waveguide. The gold bars represent top electrical contacts to the p and n-doped layers. Vertical arrows on the left and right hand sides of the waveguide denote the EL emission collected above the out-coupler and above the QD position, respectively. b-d) False colour SEM image of a typical device. The red, blue and gold colours show the biased and unbiased regions, and the top contact respectively. The green areas represent notches, which break electrical connection in the waveguide. b) Control waveguide without a notch. c) Waveguide with a small notch (250 nm long). d) Waveguide with a notch the length of the waveguide.

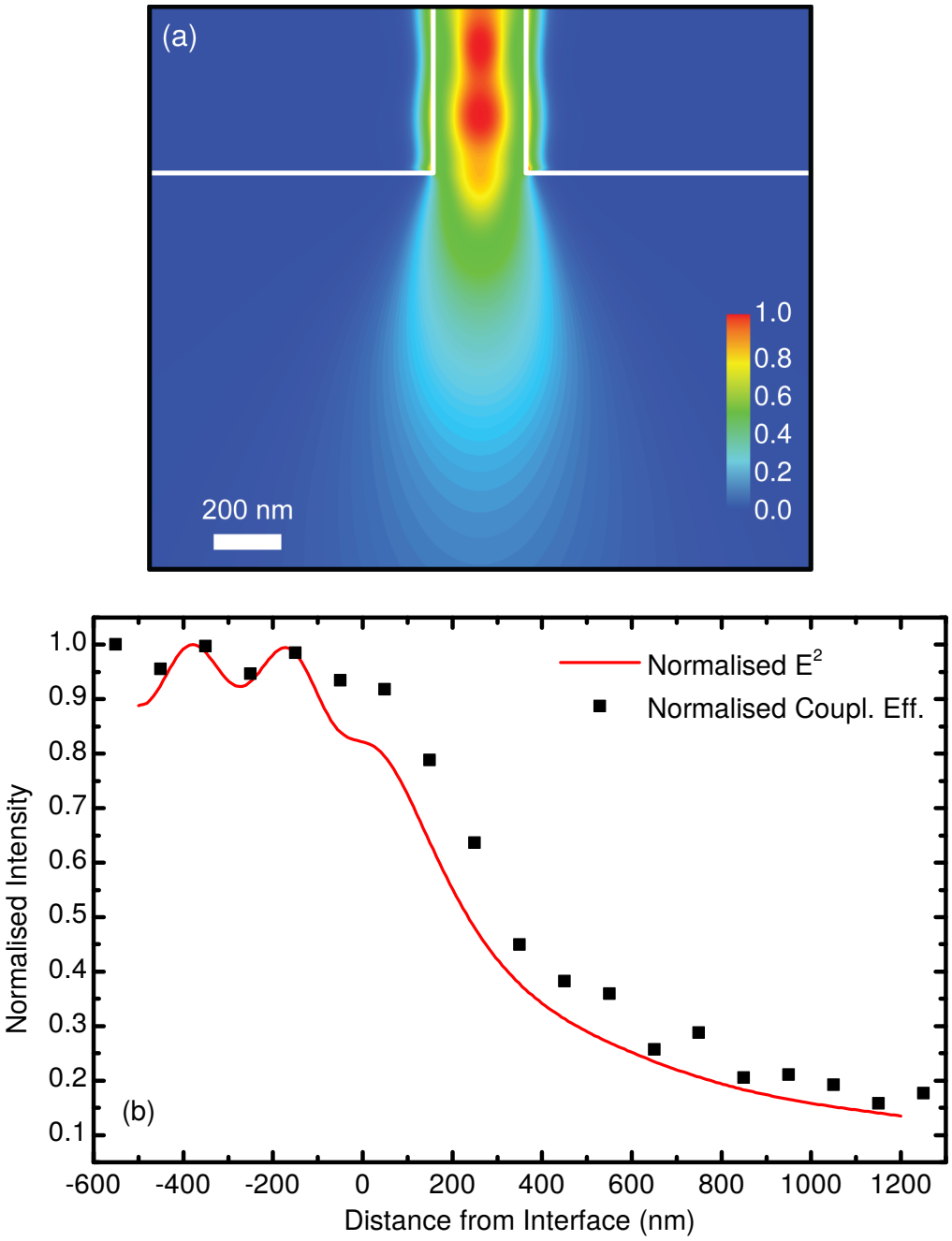

Figure 5.5 – a) Electric field intensity profile of the waveguide mode in the QD plane, obtained by finite-difference time-domain modelling using an eigenmode source within the waveguide. The area of the figure corresponds to the dashed white square on the SEM image in Figure 5.4. b) Comparison of waveguide mode's electric field intensity and normalised coupling efficiency of the QD to the waveguide mode.

description of the setup is presented in Section 3.4.5.2. The EL spectra were recorded using a single 0.75 m spectrometer and liquid N_2 cooled charge-coupled device (CCD) camera with resolution of 17 μeV. For time-correlated single-photon counting measurements, the emission was filtered using two separate 0.75 m spectrometers with a bandwidth of 90 μeV and detected by two single-photon avalanche diodes (SPADs).

5.4 Waveguide Coupled Single-Photon Emission

Figure 5.6 shows an EL map, which was obtained by raster scanning the collection across the device using motorised mirrors, whilst recording the intensity on a SPAD. The scan area matches the SEM image shown in Figure 5.4, with the control waveguide on the left-hand side. Emission is only observed from the contacted regions and out-couplers. The out-couplers are bright due to coupling of the EL emission from the QDs in the contacted regions to the waveguides. The out-coupler on the control waveguide (left) has a higher intensity as all QDs in the waveguide are excited. Brighter spots at the interface between the waveguides and the electrically contacted bar appear due to light scattering. Emission is only observed from the contacted regions and the out-couplers, this confirming the performance of the waveguides and verifying the electrical isolation.

Current-voltage (IV) characteristics of a typical device are shown in Figure 5.7. The signature of a second diode in parallel with a series resistance is observed. The origin of these defects is most likely due to gold diffusion through the device as discussed in Section 3.3.1. As a result of these defects a higher voltage needs to be applied to the device to observe EL.

Figure 5.8 presents EL spectra from a typical device, collected separately from each end of the middle waveguide (i.e. vertically above the emitting QDs and at the out-coupler). The onset of predominantly single-dot EL emission occurs at 2.3–2.4 V, as shown in Figure 5.8b. With bias, the lines grow in intensity. At approximately 2.9 V, background emission also starts increasing, which can most likely be attributed to EL from other QDs, and becomes increasingly strong with increasing voltage as seen in Figure 5.8d. A bright line is observed in all spectra at 921.8 nm. The best signal-to-background ratio for this line is achieved at 2.88 V. At this bias, the line intensity (measured on the CCD) in the spectra collected above

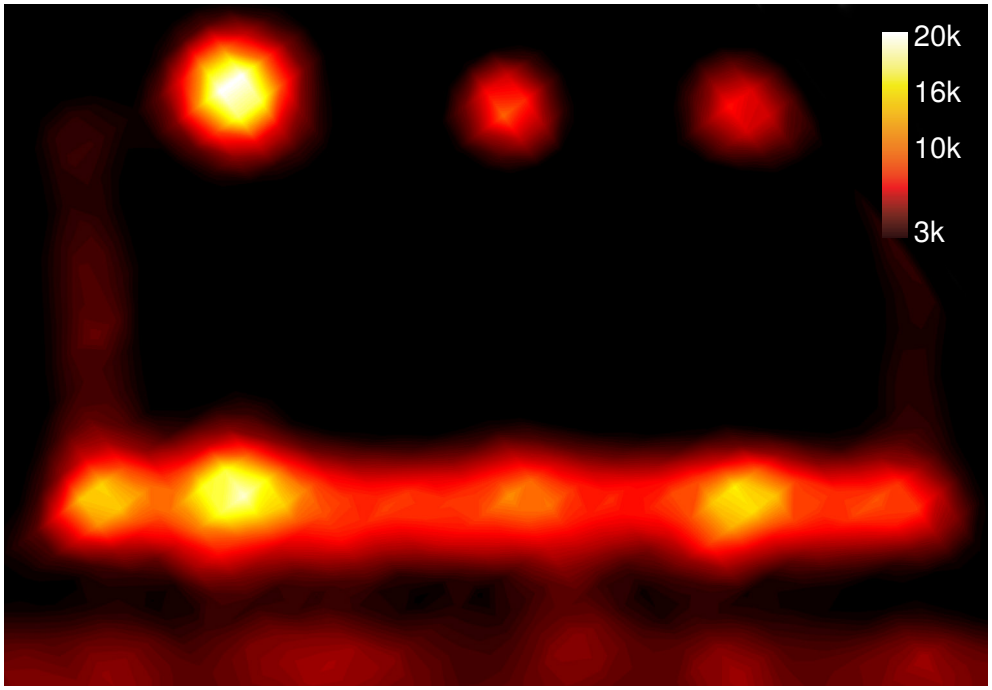

Figure 5.6 – Unfiltered electroluminescence map created by raster scanning the collection path across the tested device. Map area is the same as the SEM in Figure 5.4. Scale corresponds to counts per 0.5 s

the QD and from the out-coupler is as high as 30 000 counts/s and 80 000 counts/s, respectively, showing efficient coupling of the quantum dot to the waveguide mode. These spectra are shown in Figures 5.8a and 5.8c.

All further investigations were performed using the emission line at 921.8 nm at 2.88 V. In the previous spectra, the linewidth is limited by the spectrometer resolution. Further high resolution spectra were taken by collecting from the out-coupler and using a scanning Fabry-Perot interferometer with 0.3 µeV resolution, after initial filtering with a spectrometer. These spectra, shown in Figure 5.9, reveal that the line is a doublet with a linewidth of 5.9 µeV and a splitting of 15 µeV. The doublet is most likely to be due to fine structure splitting (FSS) of the neutral exciton state. The measured linewidth is comparable to the best reported values for p-i-n diode samples, such as for EL emission in thicker structures, 3.3 µeV[135] and resonance fluorescence in membrane devices under reverse bias, 2.6 µeV[136]. The observation of narrow linewidth EL is also in agreement with the suggestion that applied electric fields can stabilise the charge environment of quantum dots[141]. Altogether, this result demonstrates that high coherence, electrically

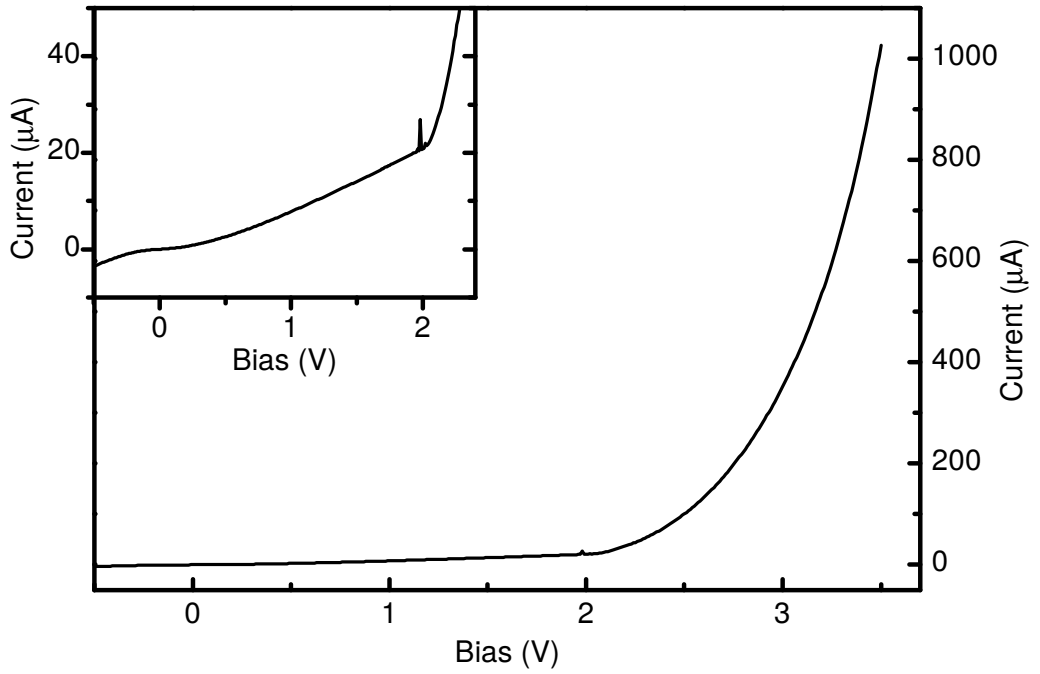

Figure 5.7 – Typical IV characteristics of a single mesa at 5 K for a current range of up-to 1 mA. Inset presents the same data over a smaller current range (up to 50 μA).

excited emission can be achieved from QDs incorporated in thin photonic diode structures.

The bias dependence of the linewidth is shown in Figure 5.10a. The measured linewidth remains constant from EL onset to 2.9 V. At higher bias, the linewidth increases with the rising background in agreement with Ref. 23, in which it was attributed to charge noise fluctuations. The increase in linewidth corresponds to the increase in overall emission intensity from the sample (Figure 5.10b).

The single-photon nature of the QD source was verified with a Hanbury Brown and Twiss (HBT) experiment, in which the filtered emission collected above the QD was passed through a fibre beamsplitter and coincidences were recorded. The resulting normalised histogram for the second order correlation function $g^{(2)}_{HBT}(t)$ without background subtraction is shown in Figure 5.11a. A raw value $g^{(2)}_{HBT-Raw}(0) = 0.34 \pm 0.04$ was measured. By deconvolving the experimental data with the temporal response of the detection system (Gaussian, full width at half maximum of 874 ps), $g^{(2)}_{HBT}(0) = 0.10 \pm 0.03$ was obtained, which shows that the source is strongly antibunched. The remaining multi-photon emis-

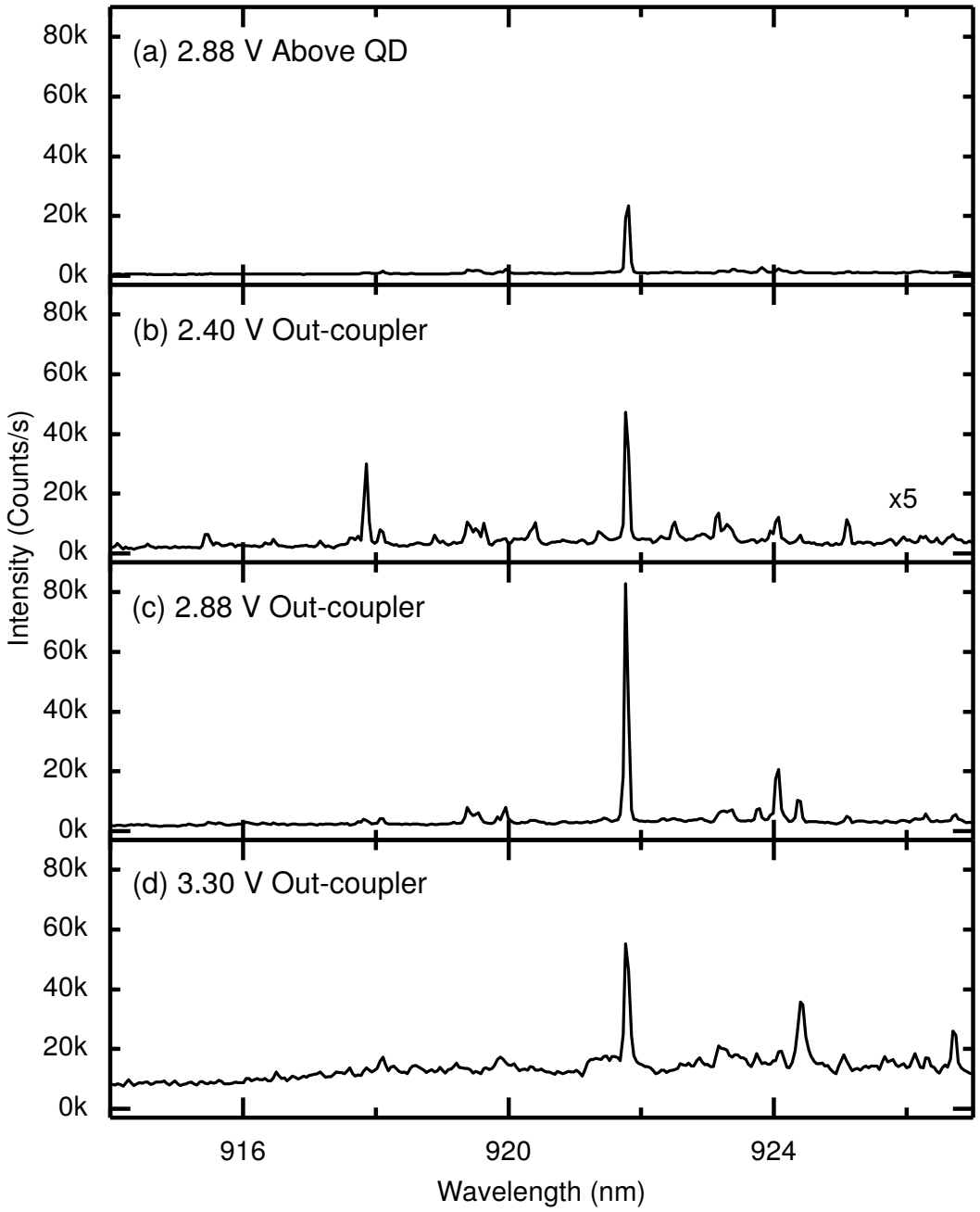

Figure 5.8 – Electroluminescence spectra collected from a) above the quantum dot at a bias of 2.88 V, from the out-coupler at a bias of b) 2.40 V, c) 2.88 V and d) 3.30 V.

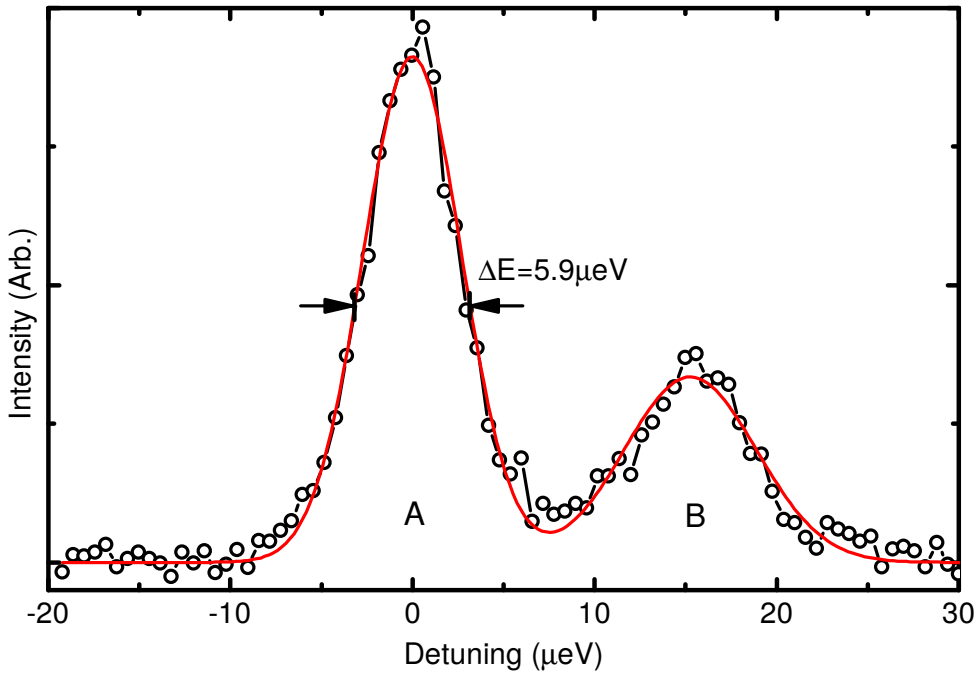

Figure 5.9 – High-resolution spectrum of the investigated emission line (open black circles) at 2.88 V. Red continuous line corresponds to a fit to the data.

sion probability is likely to be due to the residual background emission that can be seen in Figure 5.8a.

Propagation of single-photons along the waveguide was confirmed with an HBT experiment with emission collected from the out-coupler. Raw and deconvolved values $g^{(2)}_{HBT-Raw}(0) = 0.32 \pm 0.03$ and $g^{(2)}_{HBT}(0) = 0.07 \pm 0.02$ were obtained, as shown in Figure 5.11b. Again, the emission is strongly antibunched, demonstrating that it passes through the waveguide without deterioration of the photon statistics.

To verify the origin of the line, a cross-correlation measurement was performed, in which correlations were recorded between the emission collected above the QD and from the out-coupler. The resulting normalised histogram is presented in Figure 5.11c. Raw and deconvolved values are $g^{(2)}_{HBT-Raw}(0) = 0.33 \pm 0.03$ and $g^{(2)}_{HBT}(0) = 0.10 \pm 0.02$. This unambiguously proves that the emission observed at both ends of the waveguide originates from the same QD, i.e. that the single-photon EL emission from a single quantum dot couples to the waveguide mode and propagates along the waveguide.

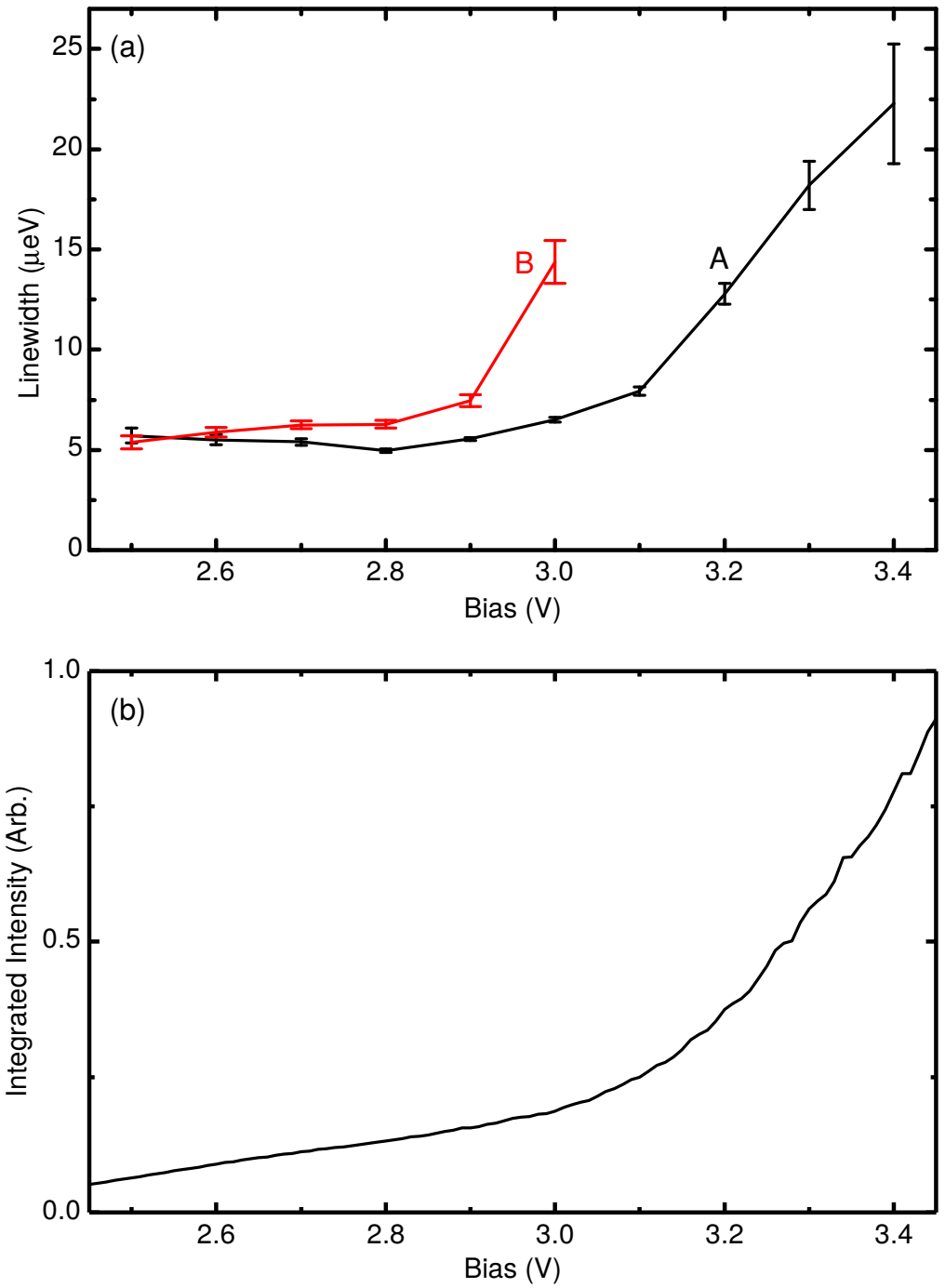

Figure 5.10 – a) Measurement of the linewidth of the two emission lines as a function of bias. Line labels correspond to those in Figure 5.9. b) Integrated intensity of all emission from 900–950 nm as a function of bias.

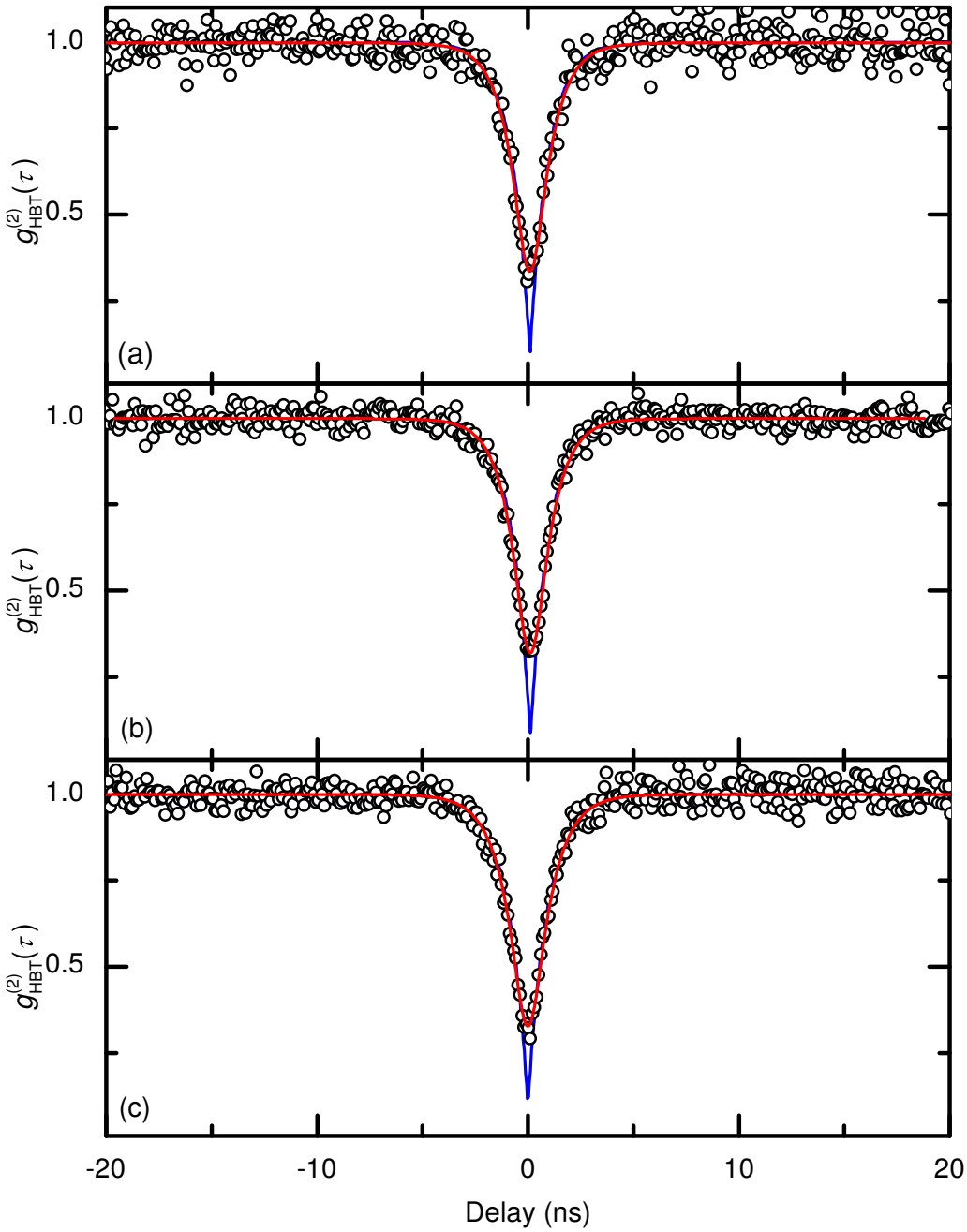

Figure 5.11 – Normalised second order correlation function for the quantum dot (open black circles) measured a) at quantum dot's location, b) at the out-coupler and c) cross correlated between photons collected at the out-coupler and at the quantum dot location. The red continuous line is a fit to the data taking into account the time response of the detection system. The blue line corresponds to fits in the limit of infinitely fast detectors.

5.5 Summary and Outlook

In conclusion, the monolithic integration of an on-demand electrically driven high quality quantum emitter, an InGaAs self-assembled quantum dot, with a nanobeam waveguide has been demonstrated. With careful design and fabrication, the ability to electrically excite and direct the highly coherent single-photon emission from a single quantum dot along the waveguide has been achieved. Correlation measurements performed above the quantum dot and at the out-coupler prove the single photon nature of the source. By performing cross-correlation measurements, the propagation of single photons from the same quantum dot along the waveguide was confirmed. This proof of concept device provides the basis for practical electrically driven single-photon sources which can be readily coupled to waveguide filters, directional couplers and other elements of quantum photonic circuits.

References

[8]T. D. Ladd, F. Jelezko, R. Laflamme, Y. Nakamura, C. Monroe and J. L. O'Brien, "Quantum computers", Nature **464**, 45–53 (2010) (see pp. 1, 73).

[10]E. Knill, R. Laflamme and G. J. Milburn, "A scheme for efficient quantum computation with linear optics", Nature **409**, 46–52 (2001) (see pp. 1, 73, 93).

[15]J. L. O'Brien, A. Furusawa and J. Vučković, "Photonic quantum technologies", Nature Photonics **3**, 687–695 (2009) (see pp. 1, 73, 93).

[24]J. Y. Marzin, J. M. Gerard, a. Izrael, D. Barrier and G. Bastard, "Photoluminescence of Single Inas Quantum Dots Obtained by Self- Organized Growth on Gaas", Physical Review Letters **73**, 716–719 (1994) (see pp. 7, 73).

[32]P. Michler, A. Kiraz, C. Becher, W. V. Schoenfeld, P. M. Petroff, L. Zhang, E. Hu and A. İmamoğlu, "A Quantum Dot Single-Photon Turnstile Device", Science **290**, 2282–2285 (2000) (see pp. 7, 73).

[34]Z. Yuan, B. E. Kardynal, R. M. Stevenson, A. J. Shields, C. J. Lobo, K. Cooper, N. S. Beattie, D. A. Ritchie and M. Pepper, "Electrically Driven Single-Photon Source", Science **295**, 102–105 (2002) (see pp. 7, 73).

[35]M. Pelton, C. Santori, J. Vučković, B. Zhang, G. S. Solomon, J. Plant and Y. Yamamoto, "Efficient Source of Single Photons: A Single Quantum Dot in a Micropost Microcavity", Physical Review Letters **89** (2002) 10.1103/PhysRevLett.89.233602 (see pp. 7, 73).

[37]W.-H. Chang, W.-Y. Chen, H.-S. Chang, T.-P. Hsieh, J.-I. Chyi and T.-M. Hsu, "Efficient Single-Photon Sources Based on Low-Density Quantum Dots in Photonic-Crystal Nanocavities", Physical Review Letters **96** (2006) 10.1103/PhysRevLett.96.117401 (see pp. 7, 73).

[38]S. Strauf, N. G. Stoltz, M. T. Rakher, L. A. Coldren, P. M. Petroff and D. Bouwmeester, "High-frequency single-photon source with polarization control", Nature Photonics **1**, 704–708 (2007) (see pp. 7, 73).

[47]O. Benson, C. Santori, M. Pelton and Y. Yamamoto, "Regulated and entangled photons from a single quantum dot", Physical review letters **84**, 2513 (2000) (see pp. 10, 78).

[80]*Lumerical Solutions, Inc. http://www.lumerical.com/tcad-products/fdtd/* (see pp. 25, 79).

[112]A. Schwagmann, S. Kalliakos, I. Farrer, J. P. Griffiths, G. A. Jones, D. A. Ritchie and A. J. Shields, "On-chip single photon emission from an integrated semiconductor quantum dot into a photonic crystal waveguide", Applied Physics Letters **99**, 261108 (2011) (see pp. 55, 73).

[113]M. N. Makhonin, J. E. Dixon, R. J. Coles, B. Royall, I. J. Luxmoore, E. Clarke, M. Hugues, M. S. Skolnick and A. M. Fox, "Waveguide Coupled Resonance Fluorescence from On-Chip Quantum Emitter", Nano Letters **14**, 6997–7002 (2014) (see pp. 55, 73).

[114]S. Kalliakos, Y. Brody, A. Schwagmann, A. J. Bennett, M. B. Ward, D. J. P. Ellis, J. Skiba-Szymanska, I. Farrer, J. P. Griffiths, G. A. C. Jones, D. A. Ritchie and A. J. Shields, "In-plane emission of indistinguishable photons generated by an integrated quantum emitter", Applied Physics Letters **104**, 221109 (2014) (see pp. 55, 73).

[126]H. J. Kimble, "The quantum internet", Nature **453**, 1023–1030 (2008) (see p. 73).

[127]N. Gisin, G. Ribordy, W. Tittel and H. Zbinden, "Quantum cryptography", Reviews of modern physics **74**, 145 (2002) (see p. 73).

[128]M. A. Nielsen, "Optical quantum computation using cluster states", Physical Review Letters **93**, 040503 (2004) (see pp. 73, 93).

[129]S. Tanzilli, A. Martin, F. Kaiser, M. De Micheli, O. Alibart and D. Ostrowsky, "On the genesis and evolution of Integrated Quantum Optics", Laser & Photonics Reviews **6**, 115–143 (2012) (see pp. 73, 93).

[130]E. Dekel, D. Gershoni, E. Ehrenfreund, D. Spektor, J. M. Garcia and P. M. Petroff, "Multiexciton spectroscopy of a single self-assembled quantum dot", Physical review letters **80**, 4991 (1998) (see p. 73).

[131]Y. Toda, S. Shinomori, K. Suzuki and Y. Arakawa, "Near-field magneto-optical spectroscopy of single self-assembled InAs quantum dots", Applied Physics Letters **73**, 517 (1998) (see p. 73).

[132]A. Kuther, M. Bayer, A. Forchel, A. Gorbunov, V. B. Timofeev, F. Schäfer and J. P. Reithmaier, "Zeeman splitting of excitons and biexcitons in single $In_{0.60}Ga_{0.40}As$/GaAs self-assembled quantum dots", Phys. Rev. B **58**, R7508–R7511 (1998) (see p. 73).

[133]I. E. Itskevich, S. I. Rybchenko, I. I. Tartakovskii, S. T. Stoddart, A. Levin, P. C. Main, L. Eaves, M. Henini and S. Parnell, "Stark shift in electroluminescence of individual InAs quantum dots", Applied Physics Letters **76**, 3932 (2000) (see p. 73).

[134]N. Prtljaga, R. J. Coles, J. O'Hara, B. Royall, E. Clarke, a. M. Fox and M. S. Skolnick, "Monolithic integration of a quantum emitter with a compact on-chip beam-splitter", Applied Physics Letters **104**, 129–132 (2014) (see pp. 73, 94).

[135]R. B. Patel, A. J. Bennett, K. Cooper, P. Atkinson, C. A. Nicoll, D. A. Ritchie and A. J. Shields, "Postselective Two-Photon Interference from a Continuous Nonclassical Stream of Photons Emitted by a Quantum Dot", Physical Review Letters **100**, 207405 (2008) (see pp. 74, 83).

[136]D. Pinotsi, P. Fallahi, J. Miguel-Sanchez and A. İmamoğlu, "Resonant Spectroscopy on Charge Tunable Quantum Dots in Photonic Crystal Structures", IEEE Journal of Quantum Electronics **47**, 1371–1374 (2011) (see pp. 74, 83).

[137]L. Turyanska, A. Baumgartner, A. Chaggar, A. Patanè, L. Eaves and M. Henini, "Sharp-line electroluminescence from individual quantum dots by resonant tunneling injection of carriers", Applied Physics Letters **89**, 092106 (2006) (see p. 78).

[138]A. Baumgartner, E. Stock, A. Patanè, L. Eaves, M. Henini and D. Bimberg, "Optical Imaging of Electrical Carrier Injection into Individual InAs Quantum Dots", Physical Review Letters **105** (2010) 10 . 1103 / PhysRevLett . 105 . 257401 (see p. 78).

[139]M. J. Conterio, N. Sköld, D. J. P. Ellis, I. Farrer, D. A. Ritchie and A. J. Shields, "A quantum dot single photon source driven by resonant electrical injection", Applied Physics Letters **103**, 162108 (2013) (see p. 78).

[140]A. Faraon, I. Fushman, D. Englund, N. Stoltz, P. Petroff and J. Vučković, "Dipole induced transparency in waveguide coupled photonic crystal cavities", Optics express **16**, 12154–12162 (2008) (see pp. 78, 100).

[141]N. Somaschi, V. Giesz, L. De Santis, J. C. Loredo, M. P. Almeida, G. Hornecker, S. L. Portalupi, T. Grange, C. Antón, J. Demory, C. Gómez, I. Sagnes, N. D. Lanzillotti-Kimura, A. Lemaítre, A. Auffeves, A. G. White, L. Lanco and P. Senellart, "Near-optimal single-photon sources in the solid state", Nature Photonics **10**, 340–345 (2016) (see p. 83).

Chapter 6

On-Chip Interference of Single Photons from a Quantum Dot and a Laser

The interference of multiple photons originating from different quantum emitters is an essential component that underpins proposed linear optical quantum computing (LOQC) schemes[10, 128]. Additionally, interference between single photons and coherent states is of interest for several practical implementations in quantum communications and quantum key distribution[142–144]. For quantum interference to occur, the interfering photons must be mutually indistinguishable in all observable degrees of freedom[10]. The degree of indistinguishability between the two interfering photons can be quantified by performing a Hong-Ou-Mandel (HOM) experiment[21]. It is desirable that the generation of single photon and manipulation of the photon states all occurs within a single chip[15, 129, 145] to provide an avenue towards scalable quantum photonics. The level of photon indistinguishability that is maintained when a quantum emitter is embedded within a realistic photonic circuit is currently of great interest.

In this chapter, a detailed investigation of the on-chip two-photon interference of two dissimilar sources is presented. Photons emitted by a single InGaAs quantum dot integrated with an on-chip beamsplitter are combined with photons from an external laser within the same device, demonstrating HOM interference. The observation of two-photon interference demonstrates that indistinguishability is maintained within the photonic circuitry. The chapter begins with a brief

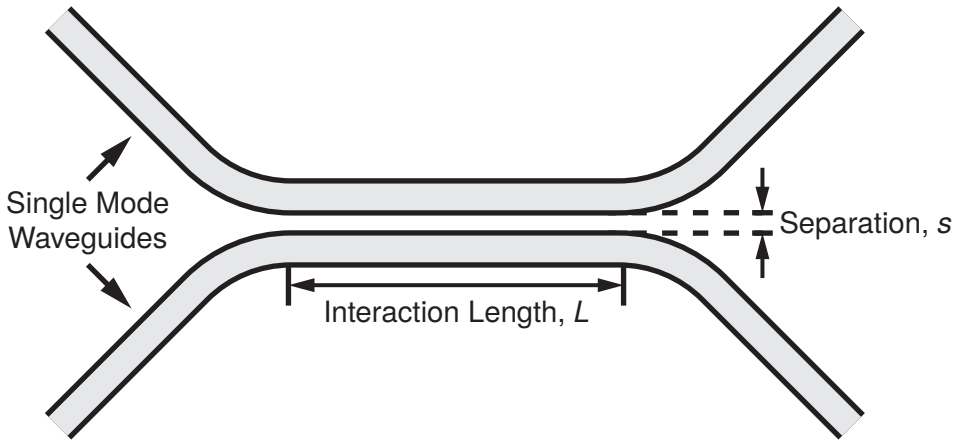

Figure 6.1 – Schematic diagram of a directional coupler showing the two waveguides seperated by s for a distance L.

overview of the principle of operation of the on-chip beamsplitter and the device design before proceeding onto experimental results. This is comprised of microphotoluminescence (μPL) measurements looking the behaviour as a whole as well as single photon correlation measurements to probe device operation at the single photon level.

6.1 Device Design

A directional coupler was chosen to be used as the on-chip beamsplitter for several reasons. Firstly, the directional coupler can be easily integrated with other circuit elements, such as nanobeam cavities[146], filters[147] or waveguide based spin-photon interfaces via single mode waveguides; this can be done without requiring any tapering or other modifications to the output. They are also advantageous due to their simple design, ease of modelling, flexibility of splitting ratio and low backscatter losses. As well as this, the behaviour of a directional coupler at the single photon level is already well understood[134, 148, 149].

6.1.1 Principle of Operation

The directional coupler consists of two single mode optical waveguides brought into close proximity such that light evanescently couples between the two waveguides (Figure 6.1). Coupled mode theory can be used to obtain an equation

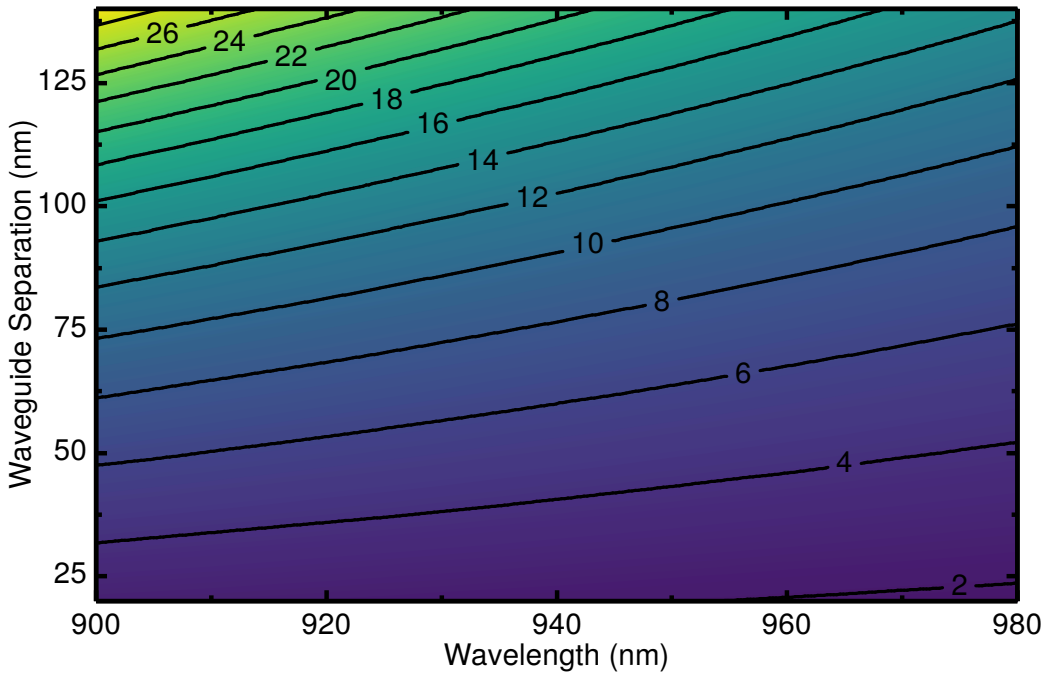

Figure 6.2 – Simulated map of coupler length required to achieve 50/50 coupling as a function of wavelength and waveguide separation. Labels correspond to the coupler length required in microns.

to describe the power transfer between the waveguides[150]. For a directional coupler with two identical waveguides the interaction length, $L_{50/50}$, required for R(reflectance):T(transmittance) 50:50 coupling is given by:

$$L_{50/50} = \frac{\lambda_0}{\pi \Delta n} \arcsin(\sqrt{0.5}) \tag{6.1}$$

where λ_0 is the free space wavelength and Δn is the refractive index difference between the symmetric and anti-symmetric supermodes. In order to determine the refractive index difference, finite-difference time-domain (FDTD) simulations were performed by Dr Nikola Prtljaga using a commercial-grade eigenmode solver and propagator[82]. Figure 6.2 shows the length of coupler required to achieve 50:50 coupling as a function of separation and wavelength. Simulations were also performed to determine optimal bend radius, expected yields and loss rates.

The correlation function, $g^{(2)}_{HOM}(\tau)$, for a HOM interference measurement taking into account non-ideal source parameters and beamsplitter ratios can be quantified as[151]:

$$g^{(2)}_{HOM}(\tau) = \frac{\frac{\eta^2}{\alpha^4} g^{(2)}_{HBT}(\tau) + \frac{\eta}{\alpha^2}\left(\frac{T^2+R^2}{TR} - 2\gamma^2 \cos\left(\frac{\Delta E \tau}{\hbar}\right)\cos^2(\phi)\exp\left(\frac{-|\tau|}{\tau_c}\right)\right) + 1}{\frac{\eta^2}{\alpha^4} + \frac{\eta}{\alpha^2}\frac{T^2+R^2}{TR} + 1} \tag{6.2}$$

where $\gamma = \langle \psi_{QD} | \psi_{Laser} \rangle$ is a measure of the wavefunction overlap of the two photons, η and α^2 are proportional to the probabilities of detecting a photon from the antibunched source and laser respectively, R and T are the reflectivity and transmission coefficients of the beamsplitter, τ is the delay between photons, $g^{(2)}_{HBT}$ is the Hanbury Brown and Twiss (HBT) of the antibunched source, τ_r and τ_{coh} are the radiative lifetime and coherence time of the antibunched source, ϕ is the angle between the polarisation of the two photons and ΔE is the energy difference between the two photons. In the directional couplers only a single polarisation mode is supported and therefore $\cos^2(\phi) = 1$. Since the timing jitter of single-photon avalanche diodes (SPADs) used is on the order of the coherence length of the QD emission, there is a significant effect upon the measurement results. This can be accounted for by convolving $g^{(2)}_{HOM}(\tau)$ with the detector response, R_f:

$$R_f(\tau) = D \exp\left(-4\ln(2)\left(\frac{\tau}{F}\right)^2\right) \tag{6.3}$$

where D is a constant and F is the detector jitter time (874 ps, see section 3.4.4.3), to give:

$$g^{(2)}_{HOM}(\tau) = R_f * \left[\frac{\frac{\eta^2}{\alpha^4} g^{(2)}_{HBT}(\tau) + \frac{\eta}{\alpha^2}\left(\frac{T^2+R^2}{TR} - 2\gamma^2 \cos\left(\frac{\Delta E \tau}{\hbar}\right)\exp\left(\frac{-|\tau|}{\tau_c}\right)\right) + 1}{\frac{\eta^2}{\alpha^4} + \frac{\eta}{\alpha^2}\frac{T^2+R^2}{TR} + 1}\right] \tag{6.4}$$

As per Reference [151], the visibility of HOM interference is defined as:

$$V(\tau) = \frac{g^{(2)}_{Dis}(\tau) - g^{(2)}_{Indis}(\tau)}{g^{(2)}_{Dis}(\tau)} \tag{6.5}$$

where $g^{(2)}_{Dis}(\tau)$ and $g^{(2)}_{Indis}(\tau)$ are the $g^{(2)}_{HOM}(\tau)$ in the cases where the input photons are distinguishable and indistinguishable respectively.

From these equations we are able to predict the expected maximum observed visibility as well as determining the sensitivity to device and experimental para-

meters.

6.1.2 Coherence Time Dependence

An important prediction to be able to make is the required QD coherence time to observe HOM interference. The coherence time is related to the QDs linewidth by:

$$\tau_c = \frac{1}{\pi \Delta\nu} \tag{6.6}$$

where $\Delta\nu$ is the full width at half maximum (FWHM) in frequency units. If we assume the case of completely distinguishable and indistinguishable photons for $g^{(2)}_{Dis}(\tau)$ and $g^{(2)}_{Indis}(\tau)$ i.e. that $2\gamma^2 \cos\left(\frac{\Delta E \tau}{\hbar}\right) = 0$ and $2\gamma^2 \cos\left(\frac{\Delta E \tau}{\hbar}\right) = 1$, along with a QD/laser intensity ratio, η/α^2, of 1 and a 50:50 beamsplitter splitter, equation 6.2 simplifies to:

$$g^{(2)}_{Indis}(\tau) = \frac{g^{(2)}_{HBT}(\tau) + 3 - 2\exp\left(\frac{-|\tau|}{\tau_c}\right)}{4} \tag{6.7}$$

$$g^{(2)}_{Dis}(\tau) = \frac{g^{(2)}_{HBT}(\tau) + 3}{4} \tag{6.8}$$

To give a visibility of:

$$V(\tau) = \frac{2\exp\left(\frac{-|\tau|}{\tau_c}\right)}{g^{(2)}_{HBT}(\tau) + 3} \tag{6.9}$$

It can be seen that setting the delay to zero, $\tau = 0$, removes all dependence upon the coherence time. However this is only true in the case of infinitely fast detectors, since the function is convoluted with the detector jitter. If the detector jitter is comparable to the coherence time, the maximum visibility, $V(0)$, becomes strongly dependent upon the coherence time. The results of the simulated HOM visibility are shown in Figure 6.3 in terms of the QD linewidth. Since the experimental setup has detectors with a combined timing resolution of 874 ps (Section 3.4.4.3), it is expected that a maximum visibility of 16 % will be achievable for a linewidth of 10 µeV which is typical for a self-assembled QD. One way to improve the visibility would be to switch to faster detectors. Faster single-photon avalanche diodes are available however detector quantum efficiency is compromised. A bet-

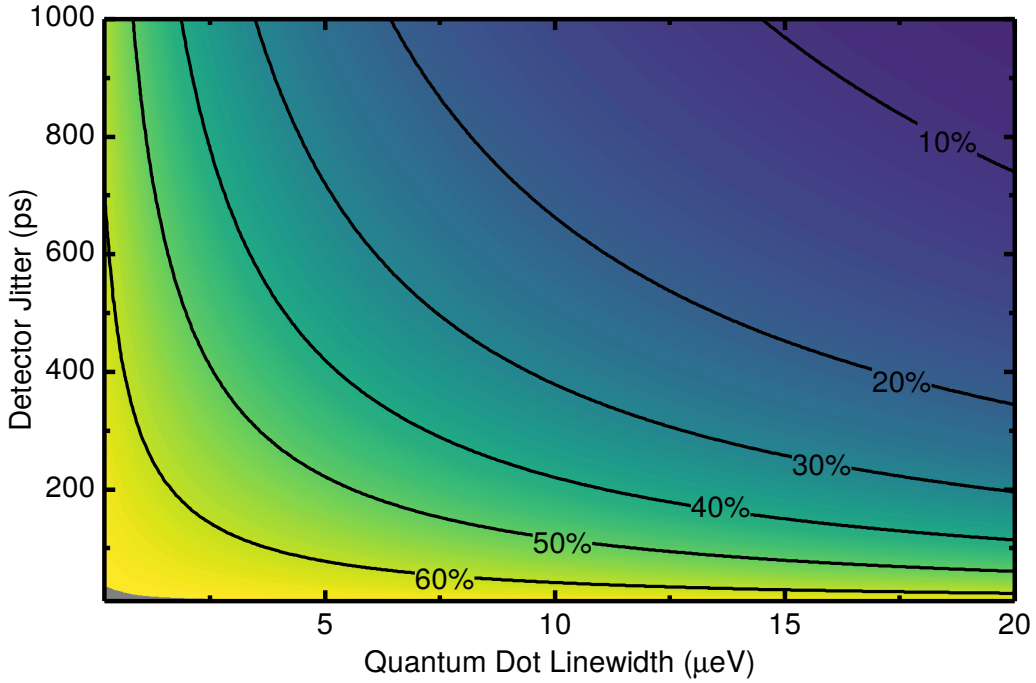

Figure 6.3 – Simulated Hong-Ou-Mandel visibility as a function of quantum dot linewidth and detector response.

ter option would be to use a superconducting nanowire single photon detector (SNSPD) system where response times of 100 ps with similar quantum efficiencies (∼30 %) to that of a SPAD are achievable. With such a system visibilities of up to 52 % would be expected.

6.1.3 Directional Coupler Splitting Ratio Dependence

Another important consideration is the effect of the splitting ratio of the directional coupler. If the fabrication is imperfect, or the quantum dot is not at the design wavelength of the directional coupler, then the splitting ratio will not be 50:50. The effect of this can be estimated from equation 6.4 and is shown in Figure 6.4. It can be seen that even with a directional coupler with a splitting ratio of 36:64. a HOM visibility of 90 % of the maximum is possible. With a typical splitting ratio variation of 48 p.p. over the range of the quantum dot emission energies, successful on-chip interference is possible and is robust against any fabrication inaccuracies.

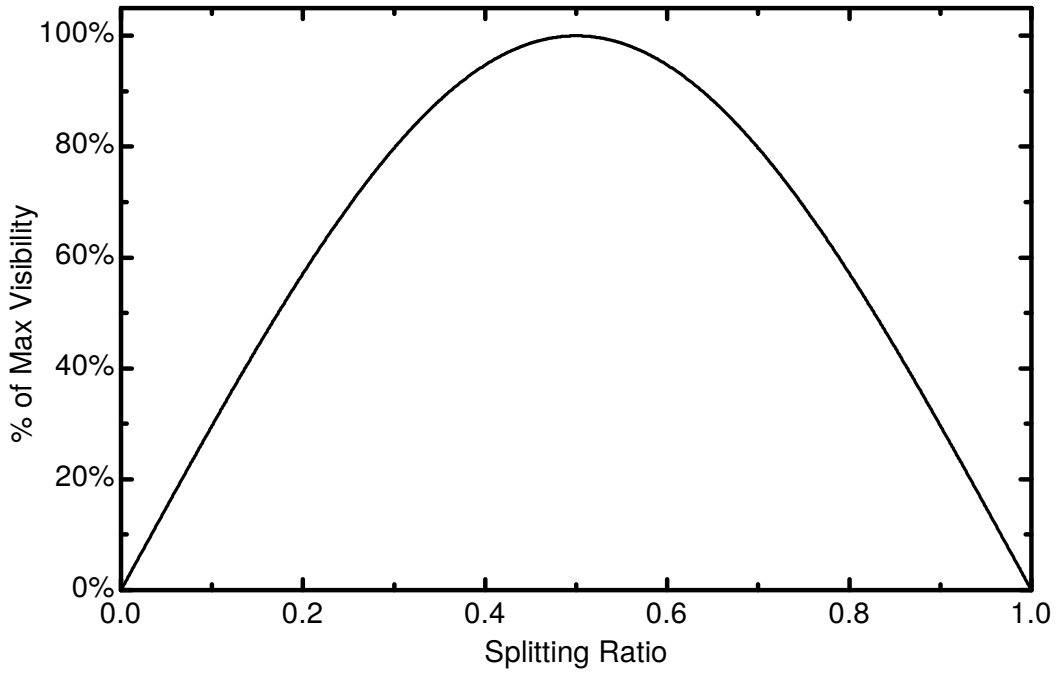

Figure 6.4 – Dependence of the HOM visibility on the beamsplitter splitting ratio.

6.1.4 Quantum Dot/Laser Intensity Ratio Dependence

Also of interest is the effect of the relative intensities of the QD emission and the incoming resonant laser, η/α^2. In the two-photon interference of two dissimilar sources, where one emitter is anti-bunched, $g^{(2)}_{HBT}(0) = 0$, and the other is Poissonian, $g^{(2)}_{HBT}(t) = 1$, the interference visibility is limited by the Poissonian nature of the second source. As the QD/laser intensity ratio, η/α^2, tends to infinity the visibility approaches 100 % (Figure 6.5a). The improvement at high ratios is a result of decreased multi-photon emission probability from the laser source. Unfortunately high QD/laser ratios are not practical for several reasons. Firstly, the ratio is increased by decreasing the laser intensity thereby reducing the number of coincident counts. Also the difference between the distinguishable and indistinguishable cases decreases even though the visibility is greater at higher ratios. Due to these effects, achieving statistical significance in visibility measurements would require integration for months to years (Figure 6.6). So far we have assumed that one of the sources is perfectly anti-bunched, i.e. $g^{(2)}_{HBT}(0) = 0$, however in reality this rarely the case. If the single-photon emitter is non-perfect, the maximum visibility no longer occurs as $\eta/\alpha^2 \to \infty$ (Figure 6.5a). Even with a

near perfect anti-bunched emitter with $g^{(2)}_{HBT}(0) = 0.05$, the optimal QD/laser ratio is reduced to 4.5. Adding the detector response further reduces the optimal QD/laser ratio (Figure 6.5b). For the detection system used with an 874 ps timing jitter, the highest visibility is expected to be observed at $\eta/\alpha^2 = 2.7$.

6.1.5 Quantum Beats

Another interesting prediction is the observation of quantum beats (Figure 6.7a). Unfortunately due to the response time of the measurement system these small time-scale features are smoothed and thus unobservable (Figure 6.7b). With an SNSPD system it may be possible to detect signatures of these quantum beats.

6.2 Experimental Arrangement

6.2.1 Sample Fabrication

The samples were fabricated following the procedure outlined in Section 3.2.3. In order to direct light onto and off the chip, semicircular $\lambda/2n$ vacuum/GaAs grating couplers[140] were added to the end of the waveguides. To correct for any fabrication inaccuracies a range of directional coupler lengths, L, separations and electron beam lithography (EBL) doses were produced. At the time of designing the devices it was unknown whether the resonant laser scattering would be an issue so the output waveguides were varied between 10 µm, 15 µm and 20 µm. A total of 540 devices were produced. A scanning electron microscope (SEM) image of a typical directional coupler and device schematic are shown in Figure 6.8.

6.2.2 Experimental Apparatus

The sample was loaded into a liquid helium cold lens cryostat (described in Section 3.4.5.2). Optical measurements were performed using a confocal microscope with four independent optical paths: two excitation paths and two collection paths. The quantum dots were excited with either a continuous wave (CW) multi-mode Ti:Sapphire laser at 840 nm for wetting layer excitation, a tunable CW single mode Ti:Sapphire laser for *p*-shell excitation or a mode-locked, femtosecond pulsed

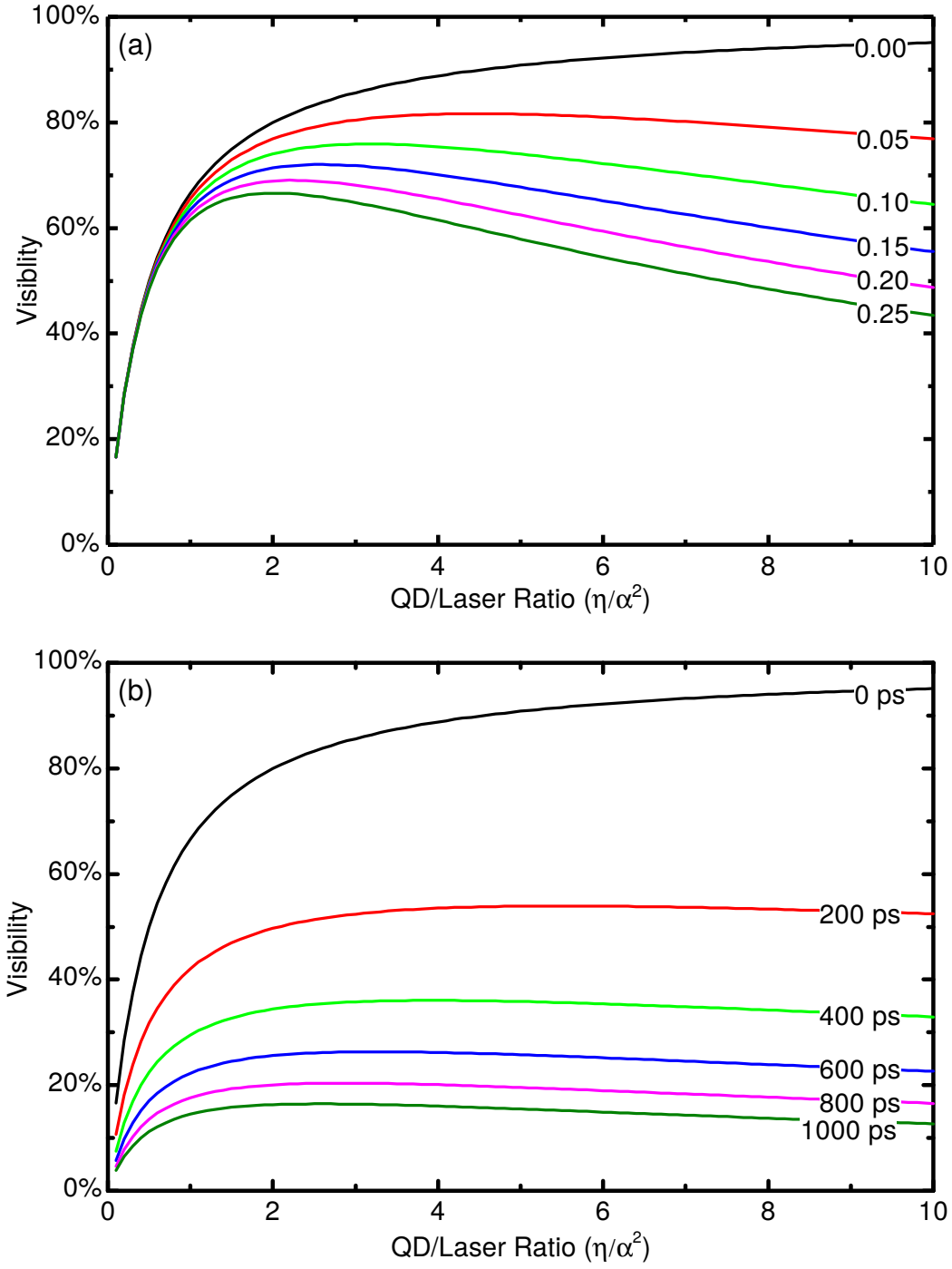

Figure 6.5 – Dependence of the HOM visibility on the QD/laser ratio for varying a) $g^{(2)}_{HBT}(0)$ of the QD and b) detector jitter time.

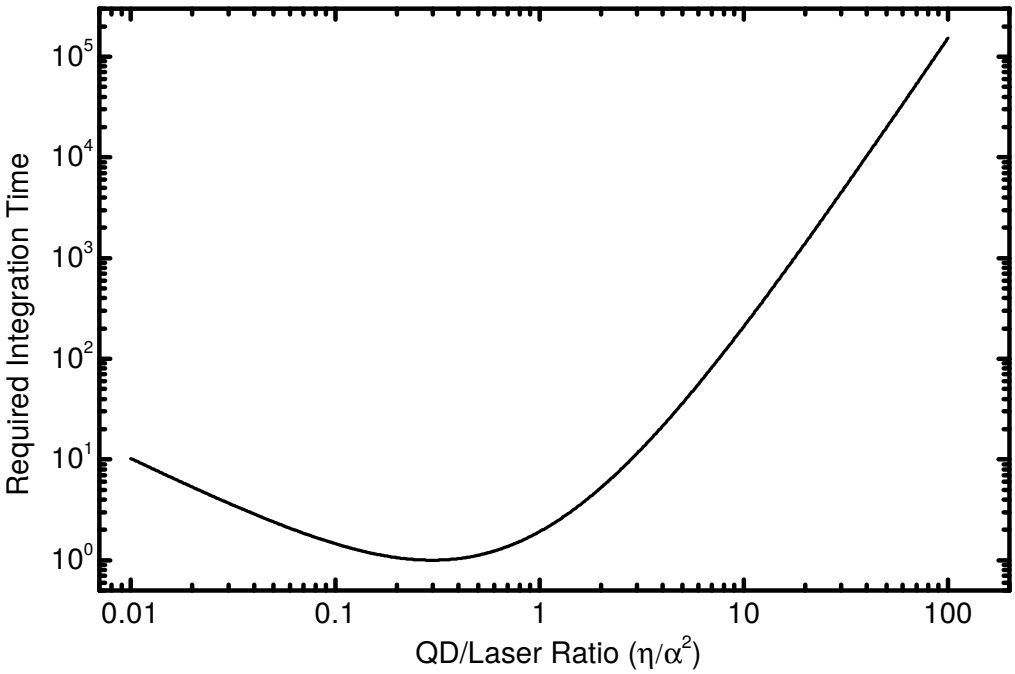

Figure 6.6 – Dependence of integration time required to acheive same noise level in visibility on QD/laser ratio, η/α^2. Integration time is shown as a fraction of the shortest time. Data assumes no timing jitter and a perfect single-photon source.

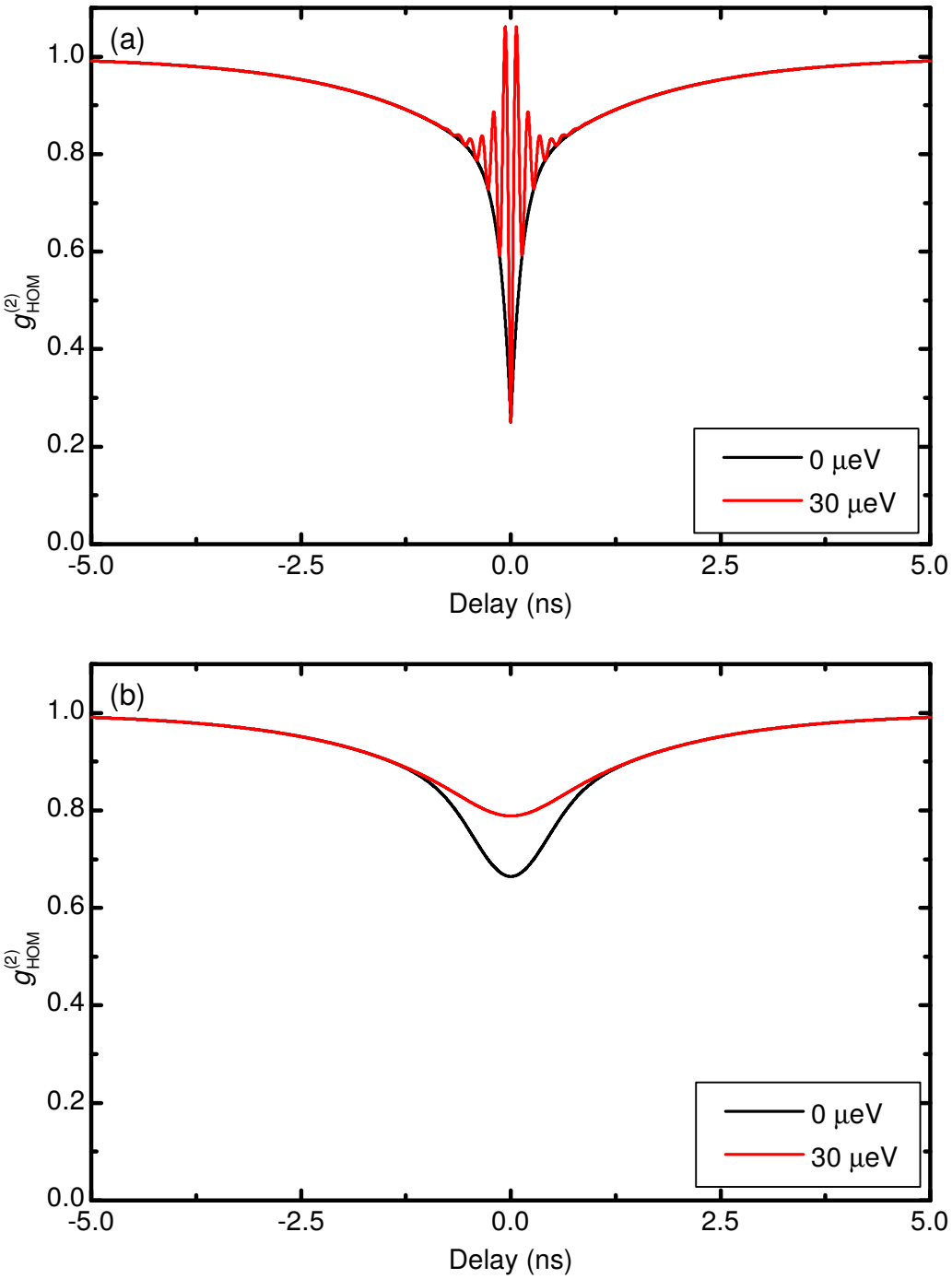

Figure 6.7 – Simulated Hong-Ou-Mandel $g^{(2)}_{HOM}$ at detunings, ΔE, of 0 μeV and 30 μeV for a) an infinitely fast detector and for b) detectors with a 874 ps jitter time.

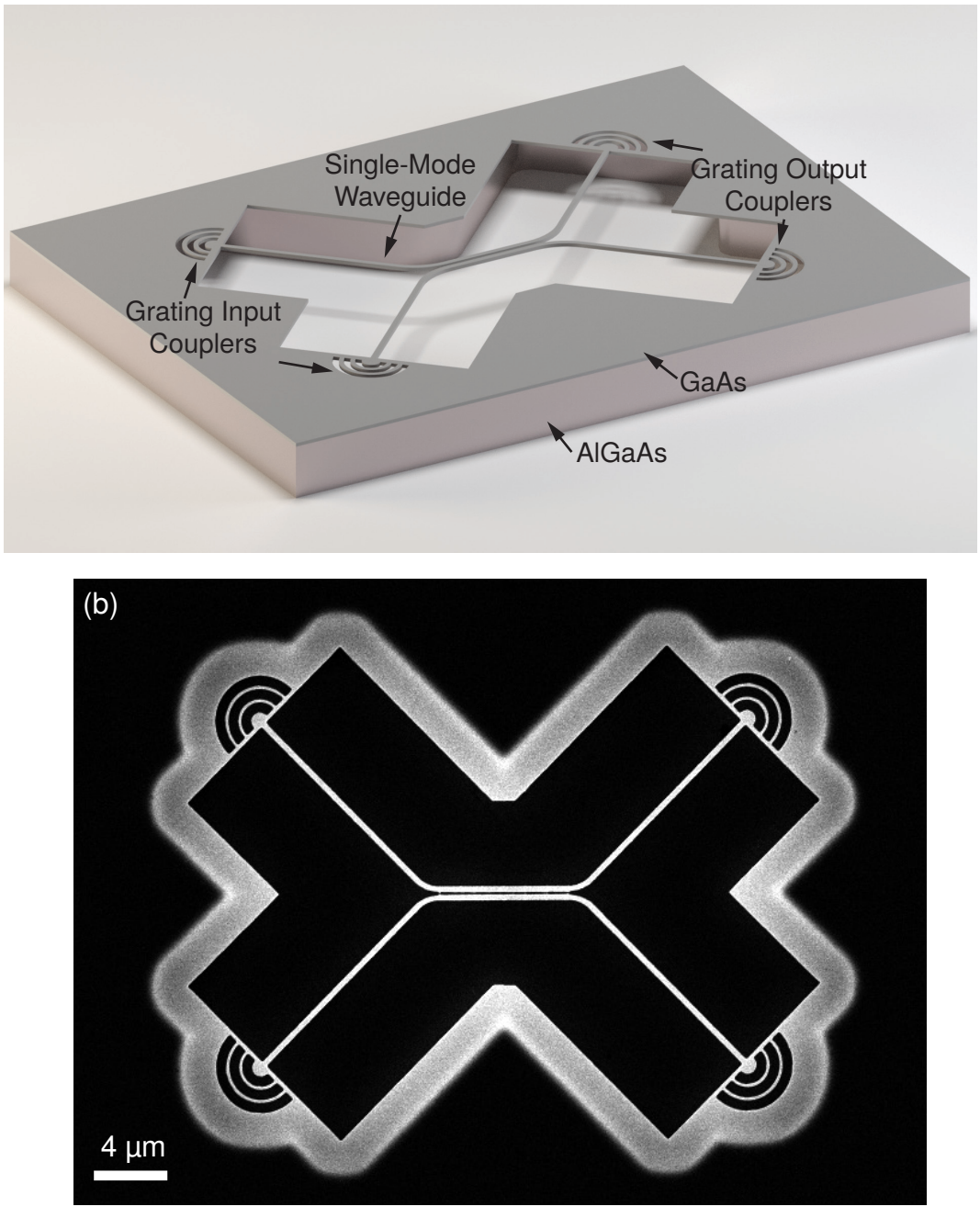

Figure 6.8 – a) Schematic of the device design b) Scanning electron microscope image of a typical directional coupler device.

Ti:Sapphire at either wetting layer or *p*-shell wavelengths. For the resonant interfering laser either a tunable single-mode CW Ti:Sapphire or a tunable external cavity diode laser was used. All the lasers used were both frequency and power stabilised. The input lasers were focused onto the sample into a diffraction limited spot of 1–2 µm using a 0.55 numerical aperture (NA) aspheric objective lens. In order to have a sufficient field of view (FOV) to image the entirety of the largest directional couplers, two relay lenses of $f = 40\,\mathrm{cm}$ in a $4f$ configuration were added into the optical path. Photoluminescence (PL) signal was collected from the output gratings by the same objective lens, through a beam splitter and into two single-mode optical fibres. Following this spectral filtering and imaging was provided by two 0.75 m spectrometers and either two charge-coupled device (CCD) cameras or fibre-coupled SPADs.

6.3 Device Characterisation

In order to observe the HOM effect with a reasonable visibility certain criteria must be met. As discussed in section 6.1.1, due to the detector timing jitter the QD emission line must have a narrow linewidth for interference to be observable. A large signal-to-noise ratio (SNR) is also needed without which the single photon characteristics of the source will be impaired. Additionally the QD must have a high enough count rate ($> 20\,000\,\mathrm{counts/s}$ on the CCD) so that the measurements do not take an impractically long amount of time. Furthermore the directional coupler must provide close to a 50/50 splitting.

Initial characterisation involved mapping the QDs within the devices to determine their suitability i.e. their linewidth, SNR and intensity. This was performed with a series of photoluminescence excitation (PLE) measurements. Although characterising the devices in this way increases experimental complexity, it does have several advantages over wetting layer excitation. One important advantage is that the laser wavelength is much closer to that of the design wavelength of the waveguides so that the laser is able to propagate along the waveguides exciting the QDs in-plane. By positioning the laser over an out-coupler and coupling the laser into the directional coupler, QDs in $3/4$ of the device will be excited. Therefore the full device can be characterised by a performing a PLE measurement at the two input couplers. To characterise an entire device with wetting layer excita-

tion (840 nm), continual stepping of the laser along each input waveguide would be required. Although a scanning excitation path can be used, maintaining alignment upon the waveguide is more difficult to automate. Additionally, as peaks in PLE spectra correspond to resonances with the internal electronic states of the QDs, this mapping can be used to open up the possibility of using quasi-resonant excitation to improve the coherence of the QDs[152–155].

Figure 6.9 shows PLE spectra for QDs located within a directional coupler device. Performing the same measurements from other excitation ports on the device produces similar spectra with most of the QD lines present along with a few new emission lines (not shown). These experimental results demonstrate that PLE is able to excite $^3/_4$ of the device.

In the process of characterisation over 2000 spectra were taken per device and therefore required automated processing. A program was written to identify QD lines with a spectrometer limited PL linewidth and a sufficiently large SNR for use with the HOM experiment. An example spectrum is reported in Figure 6.10. Peaks marked in red were then investigated further using a higher resolution (resolution limit of 17 µeV) grating before testing with a Fabry-Perot Interferometer (FPI) (0.3 µeV) if needed. This process allowed rapid characterisation of the quantum dots in the directional couplers. On average one "good" quantum dot was found per device with a linewidth around 10 µeV under wetting layer excitation.

The addition of a half-wave plate and linear polariser into each collection arm allowed polarisation sensitive measurements to be performed. The polarisation of the output gratings was found to be linearly polarised (Figure 6.11) due to their design, which favours light polarised transverse to the waveguide axis. Since the two output gratings and waveguides differ by 90°, the output signals are mutually orthogonally linearly polarised providing full distinguishability between the outputs. This also makes it possible to increase the SNR and count rate by replacing the non-polarising collection beamsplitter with a polarising beamsplitter and half-wave plate.

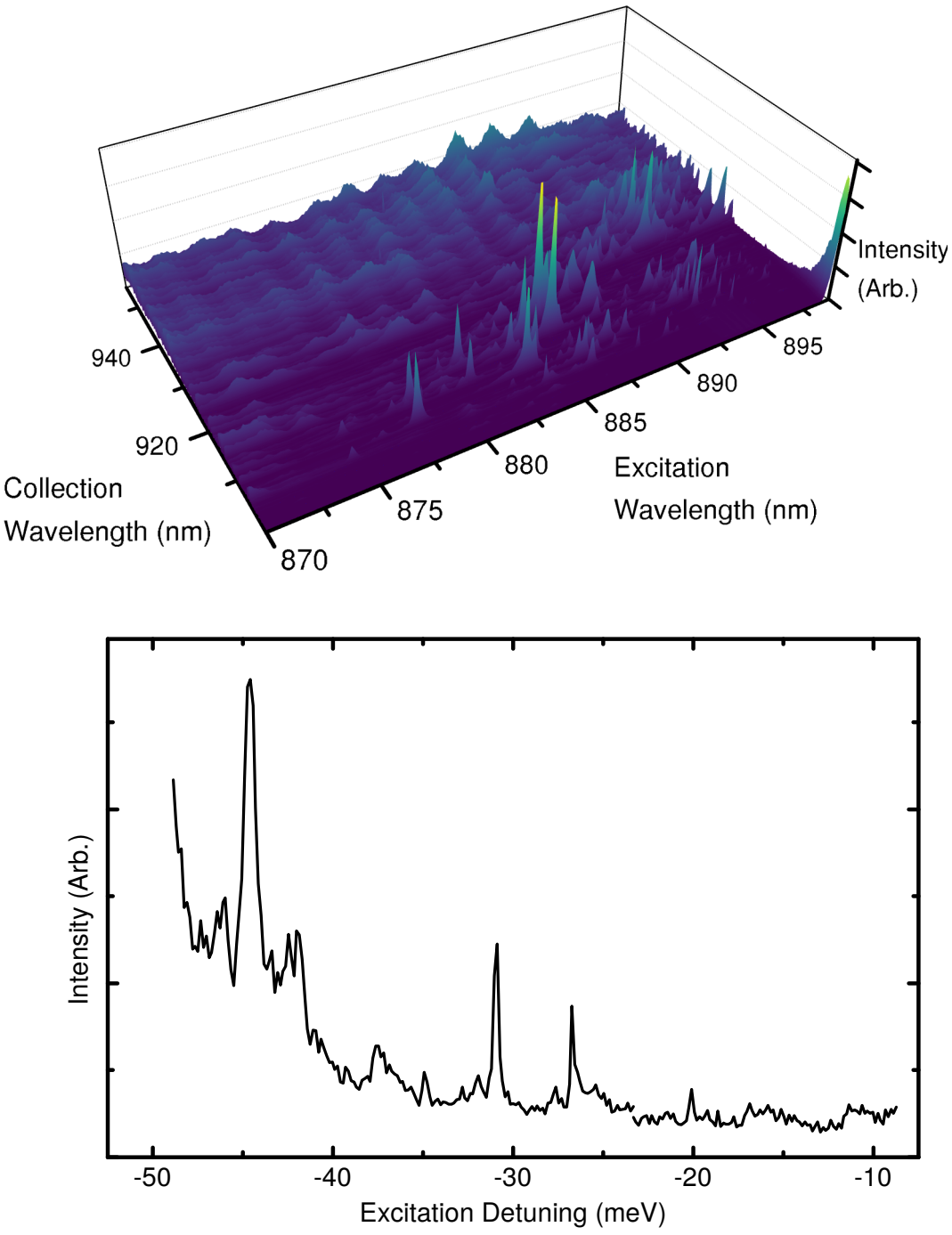

Figure 6.9 – PLE spectra obtained from a single device. A diagonal trend is observed due to the (relatively) constant offset of position of the excitation resonance from the emission energy between QDs. b) PLE spectrum for a single QD emission line.

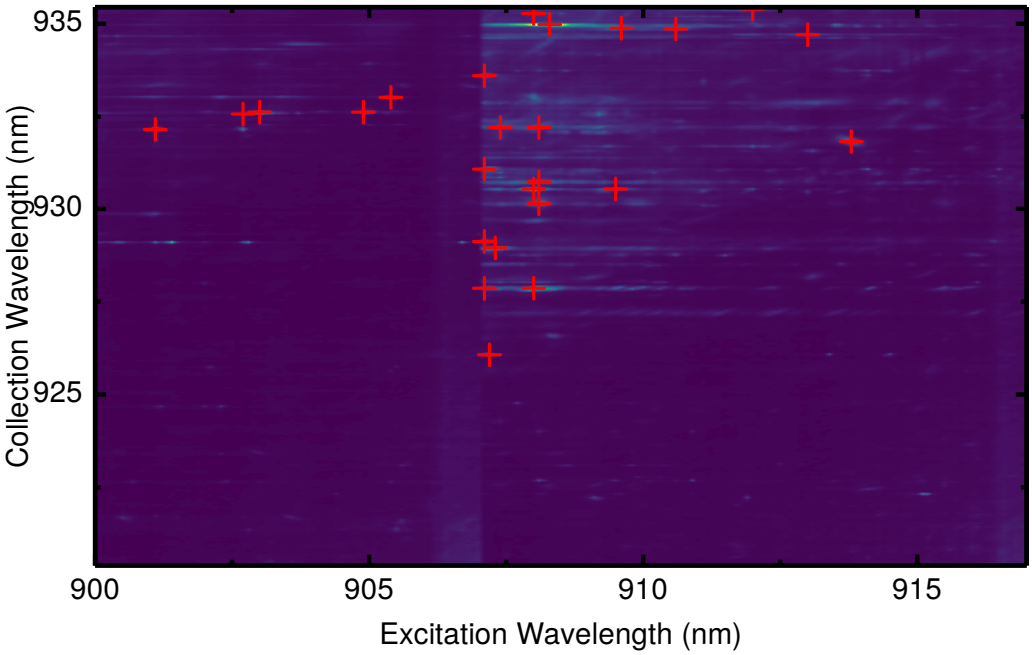

Figure 6.10 – Photoluminescence excitation spectra of a single device. Red crosses mark the locations of potential quantum dot candidates. The discontinuity at 907 nm is due to a stitching artifact. The PLE spectrum was taken in two parts due to laser scatter as the laser wavelength approached the edge of the spectral window.

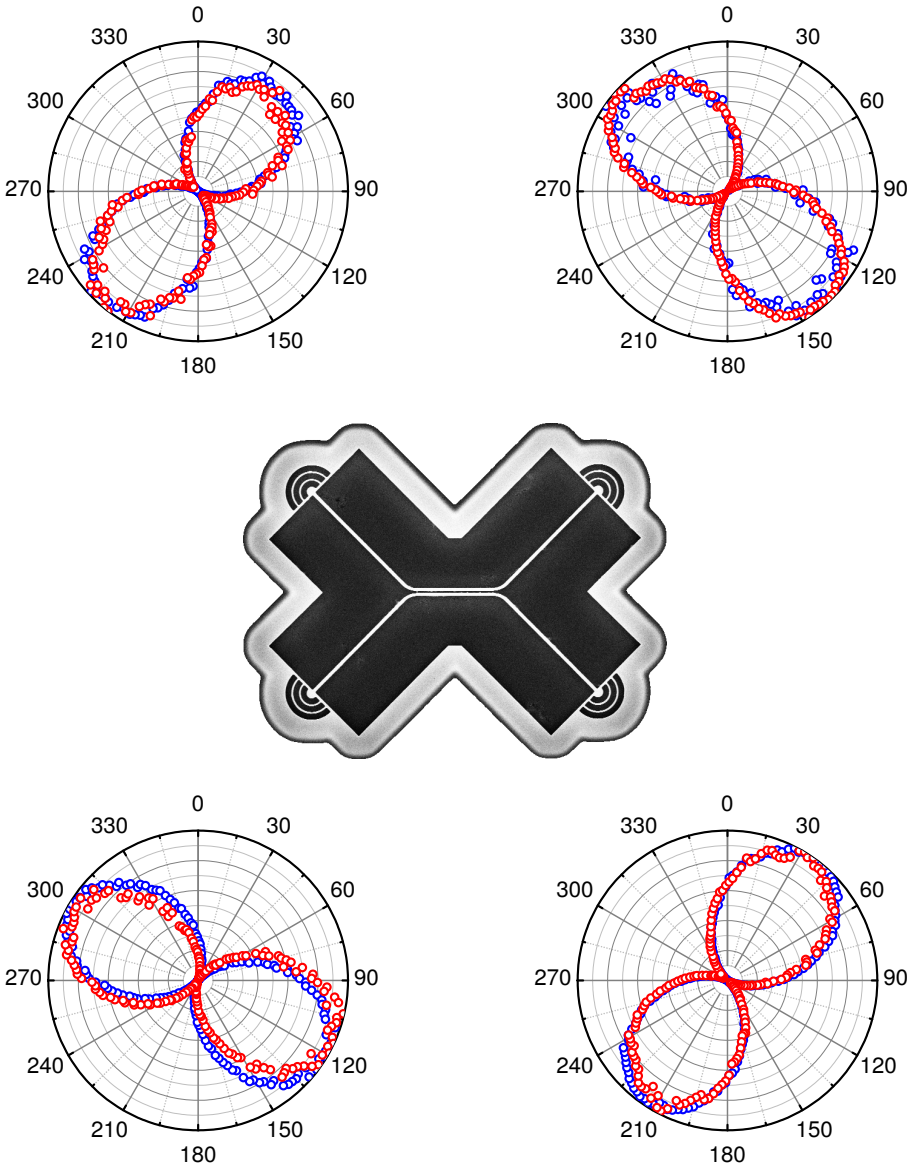

Figure 6.11 – Measured out-coupler polarisation dependence for a resonant laser (red) and embedded quantum dot (blue).

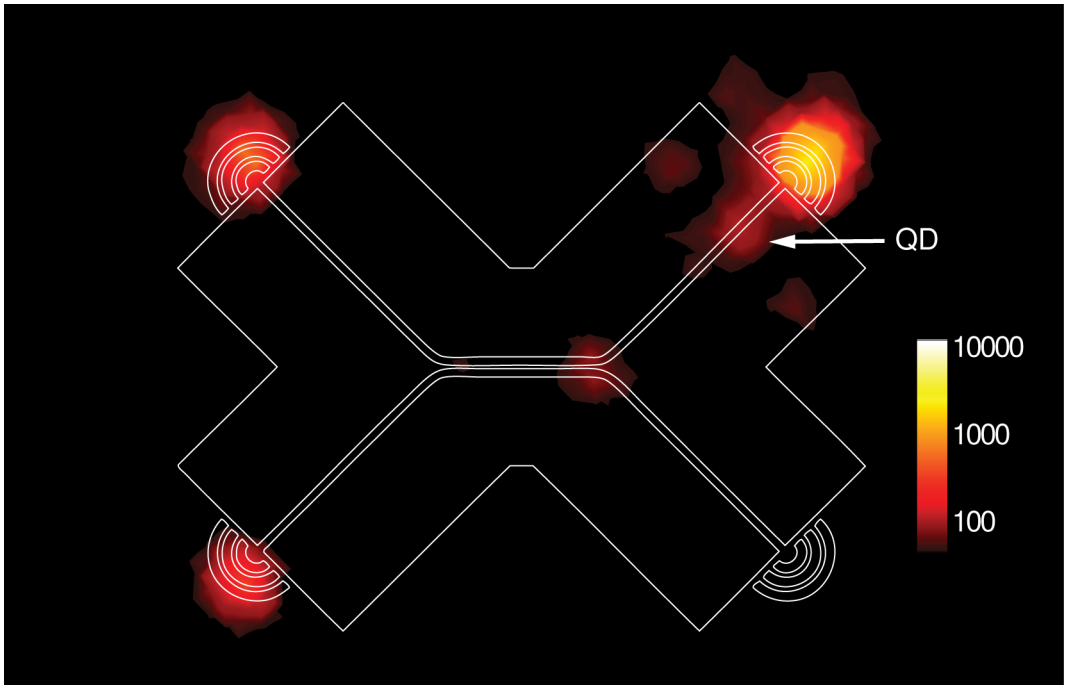

Figure 6.12 – Logarithmic scale photoluminescence map of device A filtered at the QD's wavelength. Map is overlaid with the device contour.

6.4 Device A: 15 % Hong-Ou-Mandel Visibility

The first device presented is a directional coupler with a coupling region of length $L = 7\,\mu\text{m}$ and waveguide separation of $s = 70\,\text{nm}$. To ensure the device was properly operating, a PL map was taken. The map was obtained by positioning the excitation laser (840 nm, wetting layer) over the QD of interest then raster scanning one of the collection paths across the sample using motorised mirrors, whilst recording the filtered intensity on a SPAD. Figure 6.12 shows the filtered PL map for a quantum dot emitting at 924.5 nm located in one of the input arms of the directional coupler. This map highlights the relatively low loss rate of the directional coupler design with the majority of the photons from the QD being emitted from the output gratings. A small loss from the interface between coupling region and input waveguide is observed with an intensity of 7 % of the intensity at the output couplers.

Figure 6.13 presents PL spectra, collected from above the QD and above each out-coupler. The same emission line is observed in all spectra. The linewidth is limited by the spectrometer resolution (17 µeV). The chosen QD is on the blue

side of the QD ensemble so that the emission line is resolvable without any other emission lines nearby. The power dependence of the line was measured to be linear (Figure 6.14). All further measurements were performed with an excitation power of 2 µW to be within the linear regime and sufficiently far away from saturation so that $g^{(2)}_{HBT}(0)$ and the emission linewidth is not degraded. At higher powers, although still within the linear regime, the linewidth of QD broadens.

In order to verify that the quantum dot linewidth was small enough for the HOM effect to be observable, further high resolution spectra were taken. These were performed using an FPI with 0.3 µeV resolution after initial filtering with a spectrometer. These spectra, shown in Figure 6.15, show a singlet with a linewidth of $\Delta E = (10.9 \pm 0.1)\,\mu\text{eV}$. With this linewidth the maximum HOM visibility expected for our detection system is 15 %. The combination of a linear power dependence and lack of fine structure splitting (FSS) indicate that the emission line is from a charged state of the QD.

The wavelength dependence of the splitting ratio of the device was characterised by performing transmission measurements with an external tunable Ti:Sapphire laser (Figure 6.16). These measurements were performed by scanning the laser wavelength over the QD ensemble wavelength range (approx. 900–950 nm) whilst recording the intensity at each of the output couplers filtered through a spectrometer. After correcting for differences between spectrometers and collection arms, the data was normalised and the splitting ratio calculated. The measured spectral dependence is in close agreement with the theoretical dependence obtained from coupled mode theory for the target device design. The deviation from the theory can be attributed to a combination of fabrication inaccuracies and the output couplers having a non-zero reflectivity, resulting in Fabry-Perot modes within the waveguides. One possible cause of the difference is due to a software bug within the EBL system's proximity correction code which resulted in the creation of periodic variations in the waveguide width and separation. At the emission wavelength of the QD, 924.5 nm, the directional coupler is operating as a 55:45 beamsplitter.

6.4.1 Hanbury Brown and Twiss Measurements

To verify the single photon nature of the emission, as well as the propagation of single photons along the waveguide, an on-chip HBT measurement was performed.

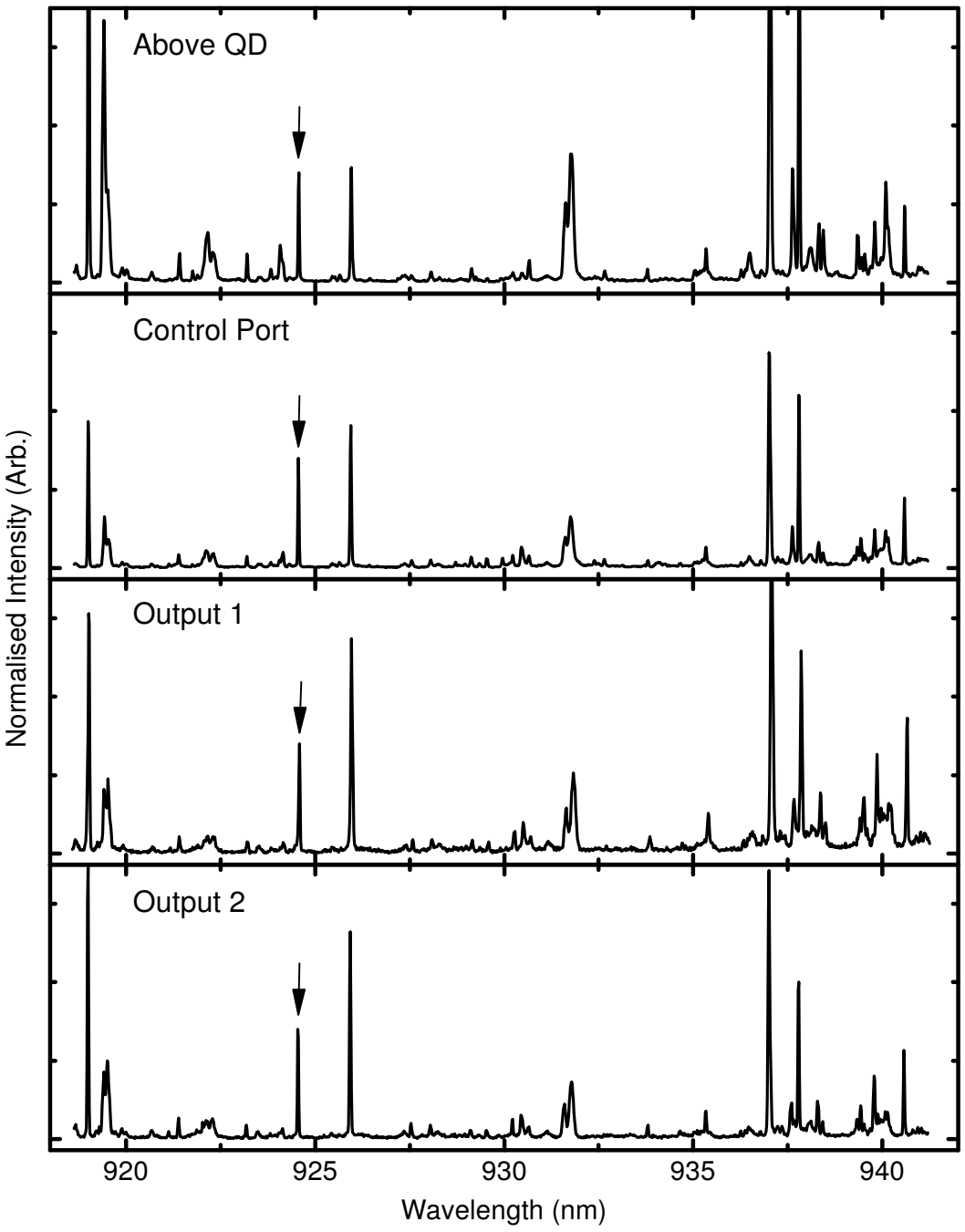

Figure 6.13 – Quantum dot PL emission spectra from above the QD, at the devices input and output ports. An arrow indicates the wavelength of the emission line used in this section. All spectra are normalised to the used QD emission line.

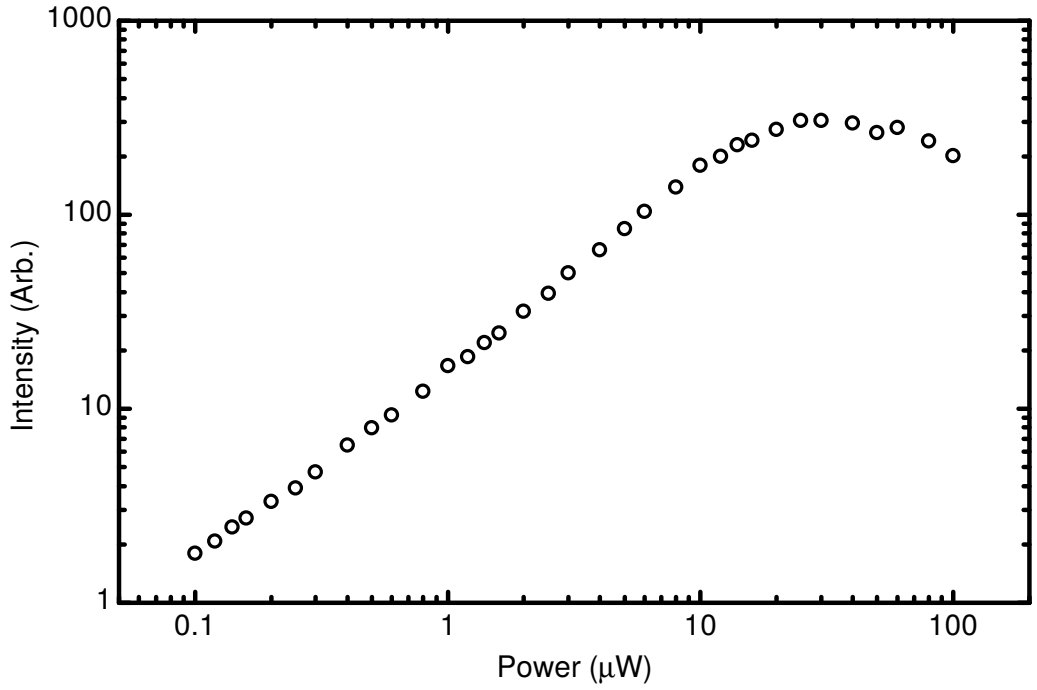

Figure 6.14 – Power dependence of the emission line under wetting layer excitation. A clear linear trend is observed up-to 10 μW.

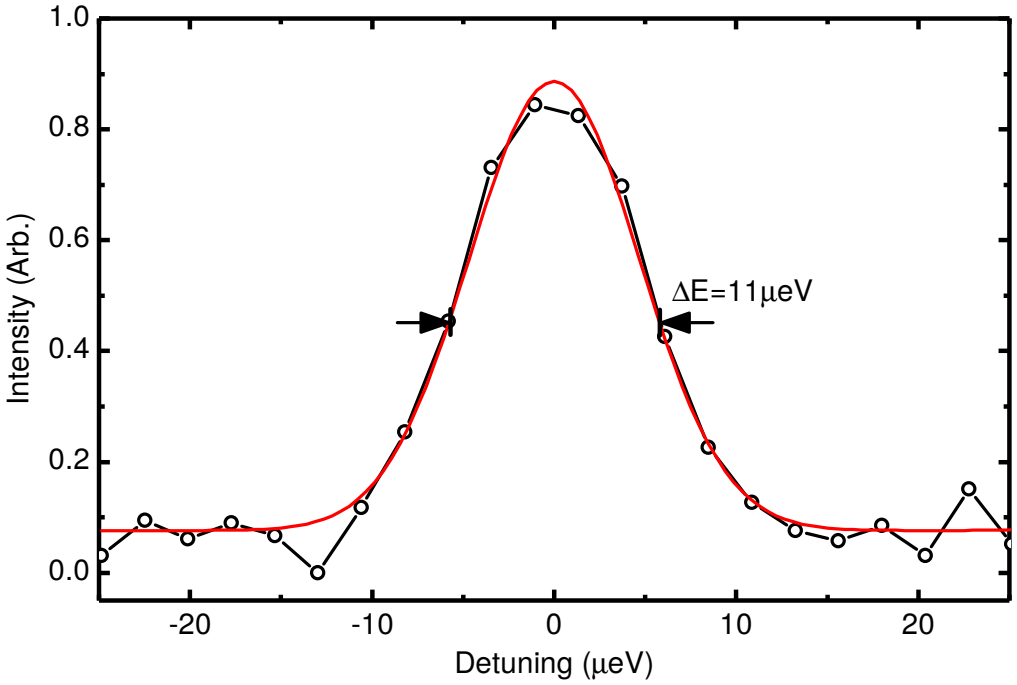

Figure 6.15 – Fabry-Perot Interferometer spectrum of the quantum dot under test. Experimental data is shown by the symbols and black lines. A Gaussian fit to the data is shown in red.

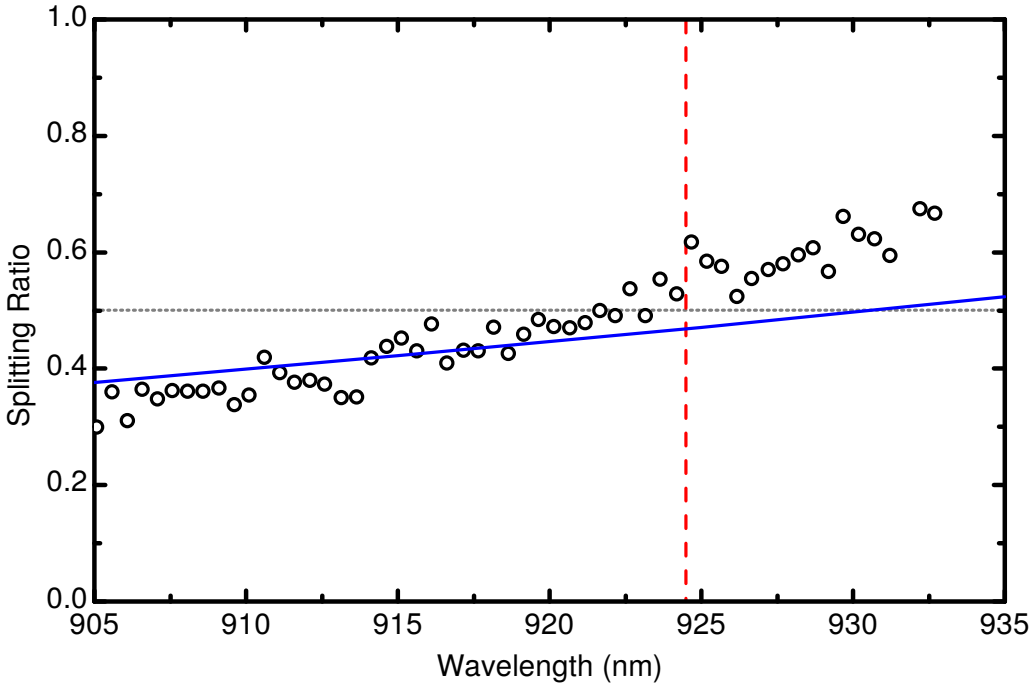

Figure 6.16 – Measured wavelength dependence (circles) of device A's beamsplitter's splitting ratio. Vertical red dashed line indicates the quantum dot's emission wavelength. The blue line is the theoretical wavelength dependence obtained from coupled mode theory for the nominal device design. Grey horizontal line indicates a splitting ratio of 0.5.

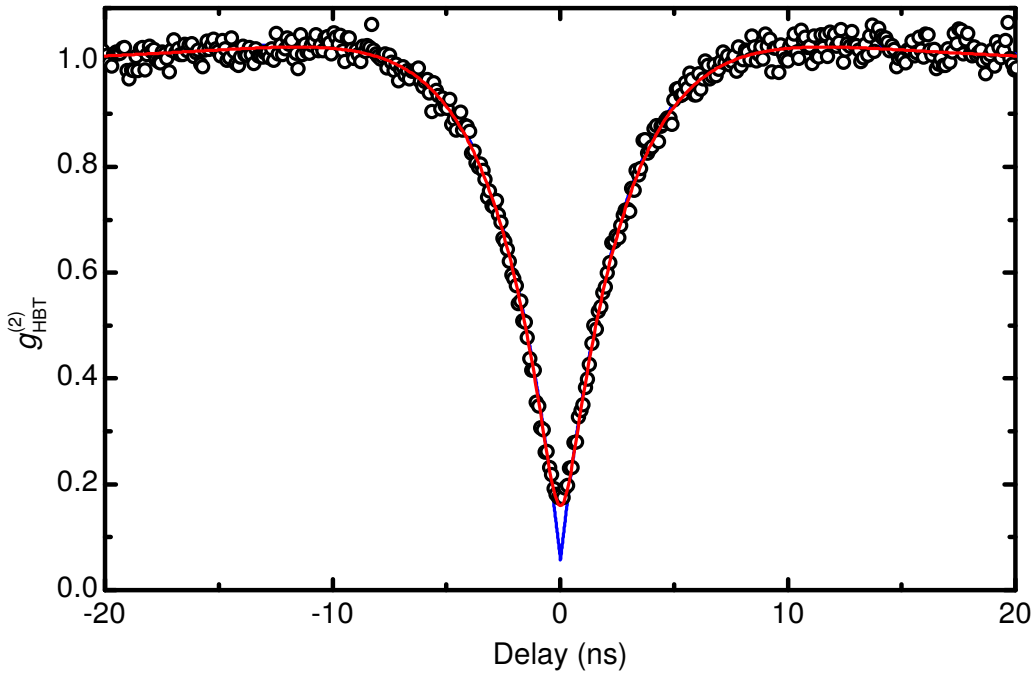

Figure 6.17 – Normalised second order correlation function for the quantum dot in device A measured through the on-chip beamsplitter (symbols) without background subtraction. The red continuous line is a fit to the data taking into account the time response of the detection system. The blue line corresponds to fits in the limit of infinitely fast detectors. The main noise present in the data originates from the single photon counting module.

This consists of cross-correlating the photons from the output ports. These measurements were performed using two 0.75 m spectrometers to filter the QD emission from each output port and then detecting the signal with two SPADs. The resulting normalised trace without background subtraction is presented in Figure 6.17. A broad bunched feature is superimposed upon the expected anti-bunched feature expected for a single-photon source. This is a sign that the quantum dot is changing charge state with charge transfer to the environment[110]. In this case a fit using a single exponential is incorrect as a two-level model no longer accurately describes the system. In this case a more accurate model is based upon a three level system with a non-radiative transition to a metastable state. The energy level diagram for this model is shown in Figure 6.18. By considering rate equations it can be shown that the HBT measurement should follow:

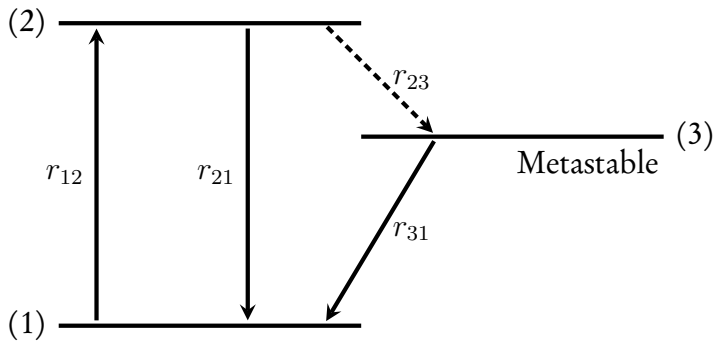

Figure 6.18 – Proposed energy level diagram of the QD's transition. Solid arrows indicate radiative transitions and dash arrows indicate non-radiative transitions.

$$g^{(2)}_{HBT}(\tau) = 1 - (1+A)\exp\left(\frac{-|\tau|}{\tau_{Excited}}\right) + B\exp\left(\frac{-|\tau|}{\tau_{Metastable}}\right) \tag{6.10}$$

where τ is the delay, $\tau_{Excited}$ and $\tau_{Metastable}$ are the lifetimes of the excited and metastable states respectively, A and B are the degree of antibunching and bunching, respectively. Fitting this to the data gives a $g^{(2)}_{HBT-Raw}(0) = 0.17 \pm 0.02$ with a decay constant of $\tau_{Excited} = (2.96 \pm 0.05)\,\mathrm{ns}$. The value of $g^{(2)}_{HBT}(0)$ is limited by the detector response of the system and not the quality of the single-photon emitter. Convolving the fit function with the detector response (Gaussian, FWHM 874 ps) provides a more accurate $g^{(2)}_{HBT}(0)$ of 0.056 ± 0.006. This is indicative of the quantum dot being a high quality single-photon emitter.

Although the curve fits the data well with a coefficient of determination, R^2, of 0.99, the noise in the data makes it difficult to obtain an accurate measure of $\tau_{Metastable}$. One would expect to be able to integrate out the noise as it should follow a Poissonian distribution, however the noise is dominated by electrical noise in the counting card. This does not effect the measurements of the HOM effect as these include the entirety of the HBT fit and not individual parameters derived from it (Equation 6.2).

6.4.2 Hong-Ou-Mandel Effect

Two-photon interference takes place when an external, attenuated resonant laser is added to the other input port of the directional coupler. Before measuring the

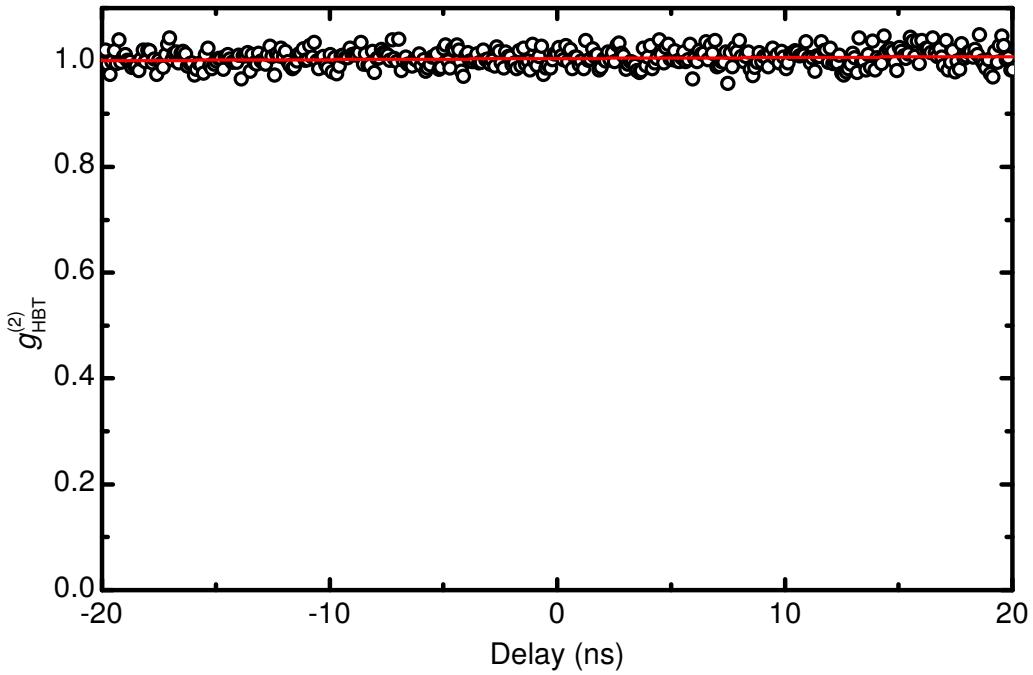

Figure 6.19 – Normalised second order correlation function for the resonant Ti:Sapphire laser (symbols). A fit to the data is shown in red.

HOM effect, the laser photons were verified to be coherent by performing an off-chip HBT, shown in Figure 6.19. The laser has $g^{(2)}_{HBT}(\tau) = 1.00 \pm 0.02$ as expected for a coherent source. Since the devices only support a single polarisation mode, distinguishability between the two sources was provided by detuning the laser by 29 μeV. This was chosen to be sufficiently large that the photons are distinguishable whilst still being within the spectral window of the spectrometer. With the long integration times needed to achieve a small noise level, the optical system can drift whilst measurements take place (even with all the precautions taken in Section 3.4.5.2). In order to minimise the effect that this drift has, the traces for the on-resonance and off-resonance cases were acquired almost simultaneously by detuning the laser on and off resonance with the QD every half an hour. Additionally both the resonant and QD excitation laser were frequency and power stabilised.

The results of these measurements after 82 hours integration is shown in Figure 6.20 for equal QD/laser intensity ratio, $\eta/\alpha^2 = 1$. Equal QD and laser intensity was chosen because even though the visibility is limited to 66 %, it is easiest to resolve the difference between the indistinguishable and distinguishable cases. It

can be seen that when the quantum dot's emission is in resonance with the laser, there is a deeper dip within a time window whose width is determined by the coherence time of the quantum dot. This is a clear indication that the photons from the two dissimilar sources have interfered, generating a N00N-state. The simulated behaviour, which includes the system temporal response, linewidth and HBT fit, agrees very well with the measured data. The level of interference can be quantified by the visibility (Equation 6.5) and is shown in Figure 6.21. A detector limited visibility of 15 % is achieved, close to the theoretical maximum of 16 % for the detection system and QD with a linewidth of 11 µeV. With a state of the art detection system (SNSPDs) a visibility of 51 % could be expected. The measured visibility is smaller than that reported by Bennett et al. for off-chip QD/laser interference, who obtained a visibility of 35 % due to slower detectors, 874 ps versus 428 ps, and a large linewidth, 10.9 µeV versus 4.4 µeV[151]. For off-chip two-QD interference experiments, the measured visibility is similar to Flagg et al. (18 %[156]) and lower than Gold et al. (39 %[153]) which were both performed under pulsed excitation thereby reducing the dependence on the detector timing jitter. Under CW excitation, Patel et al. have obtained a higher visibility of 33 %[53] for similar reasons to those for Bennett et al.

6.5 Device B: 7 % Hong-Ou-Mandel Visibility

A second device with a targeted coupler separation of $s = 60\,\mathrm{nm}$ and length of $L = 6\,\mu\mathrm{m}$ was also studied in a similar manner to the previous device. The QD emission line studied in this device emits at a slightly longer wavelength, 928.5 nm, compared to the previous sample. Spectra from each of the out-couplers is shown in Figure 6.22. The location of the quantum dot within the directional coupler is clearly visible in a PL map, obtained by raster scanning the collection across the device (Figure 6.23).

The linewidth of the QD emission line studied was determined to be (17 ± 2) µeV using a FPI with no resolvable FSS (not shown). Since the linewidth is broader than that of the previous device the visibility will be limited to 10 %. A linear power dependence was also observed (not shown) indicating the emission is also from a charged state of the QD.

As with the previous device, the splitting ratio was characterised by performing

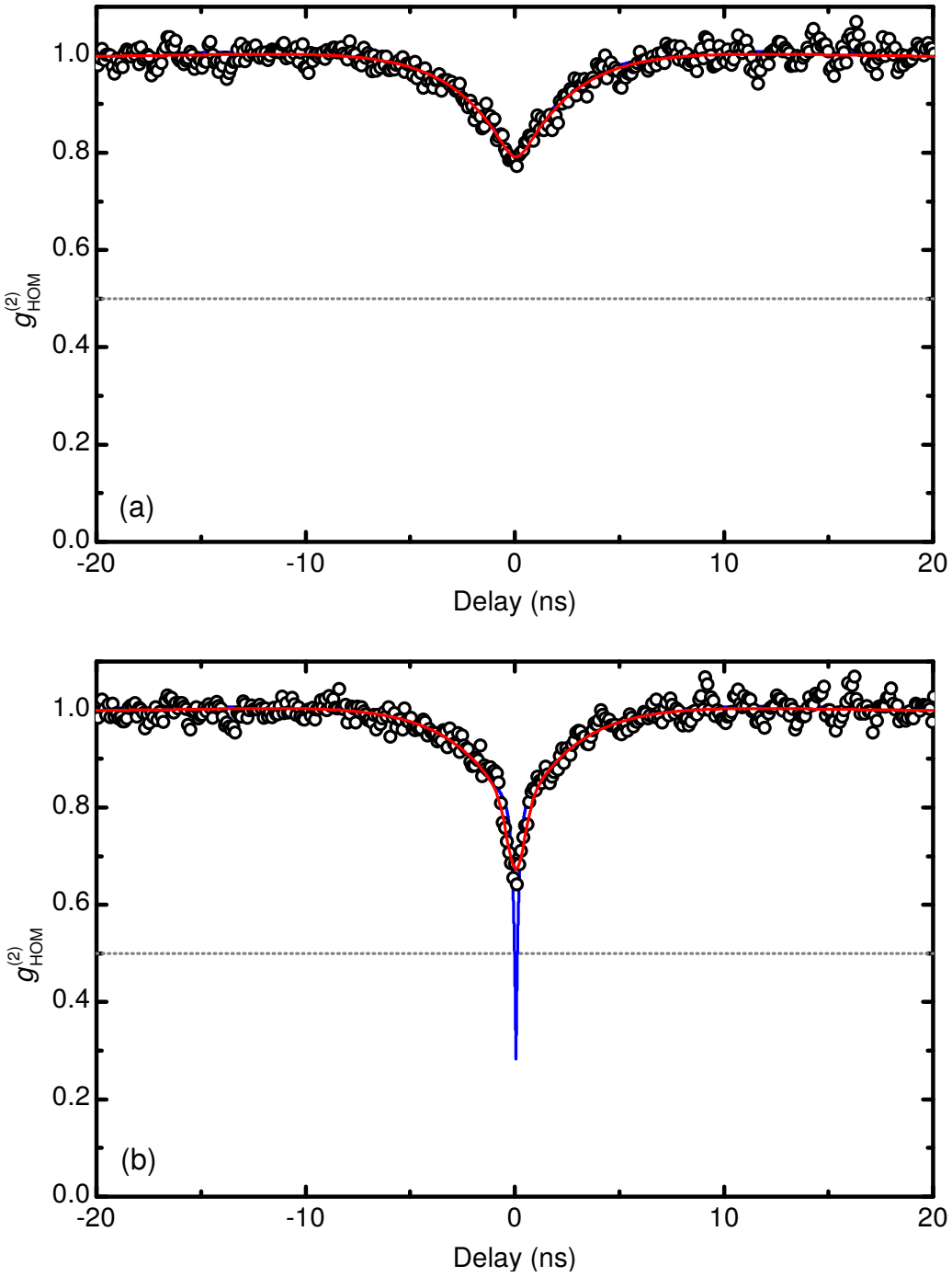

Figure 6.20 – Cross-correlated signal from device A's output ports with the laser tuned a) off resonance with the QD and b) in resonance. Open circles correspond to the experimental data. Red lines are simulated curves using the fitting parameters from the HBT measurements taking into account the detector response. Blue lines correspond to simulated curves with an infinitely fast detector.

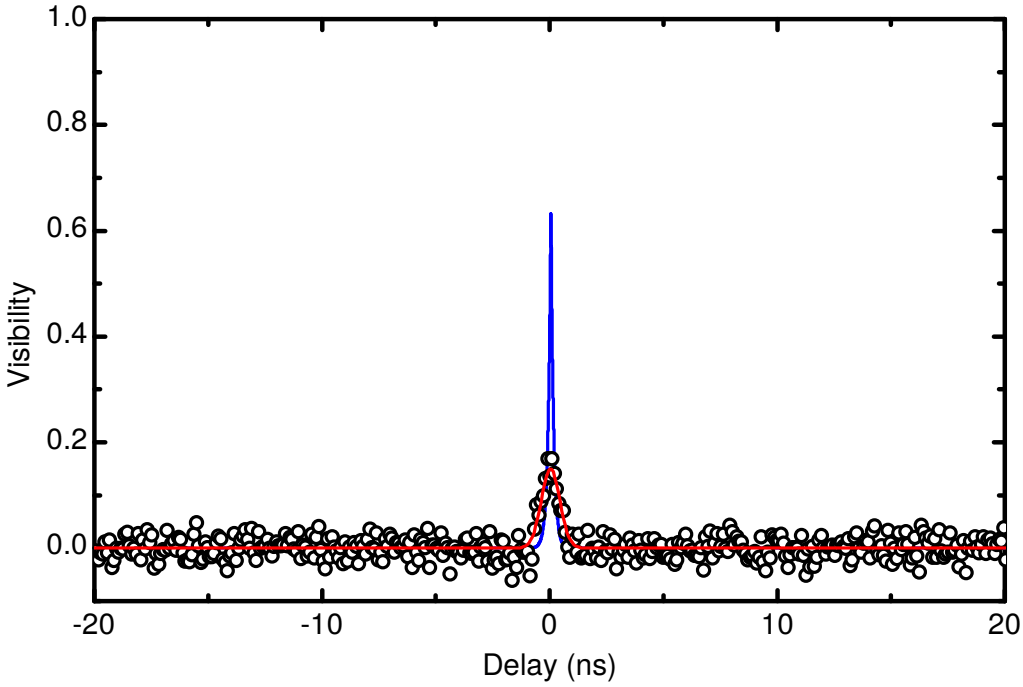

Figure 6.21 – Measured Hong-Ou-Mandel interference visibility (symbols) and simulation (red line) for device A. The blue line corresponds to the theory in the limit of infinitely fast detectors.

a transmission measurement with a tunable single-mode laser (Figure 6.24). At the emission wavelength of the QD, the directional coupler can be approximated as a 60:40 beamsplitter. Once again the large deviation from the theory is due to fabrication inaccuracies. The effect of the fabrication inaccuracies is increased due to the reduced separation in this device (60 nm and 70 nm).

The single-photon nature of the quantum dot's emission was verified with an on-chip HBT experiment. The normalised correlation function is shown in Figure 6.25 without any background subtraction. The raw data gives $g^{(2)}_{HBT-Raw}(0) = 0.35 \pm 0.01$. Taking into account the detector response, by convolving the fit function with a Gaussian, gives $g^{(2)}_{HBT}(0) = 0.27 \pm 0.01$. The remaining multi-photon emission probability can be attributed to background emission originating from other QDs spectrally nearby.

The results of the two-photon interference measurements after integrating for 41 hours is shown in Figure 6.26 for equal QD and laser intensity i.e. $n/\alpha^2 = 1$. The noise in the correlation measurements originates from the counting module used. The visibility of the interference is 7 % (Figure 6.27). The origin of the

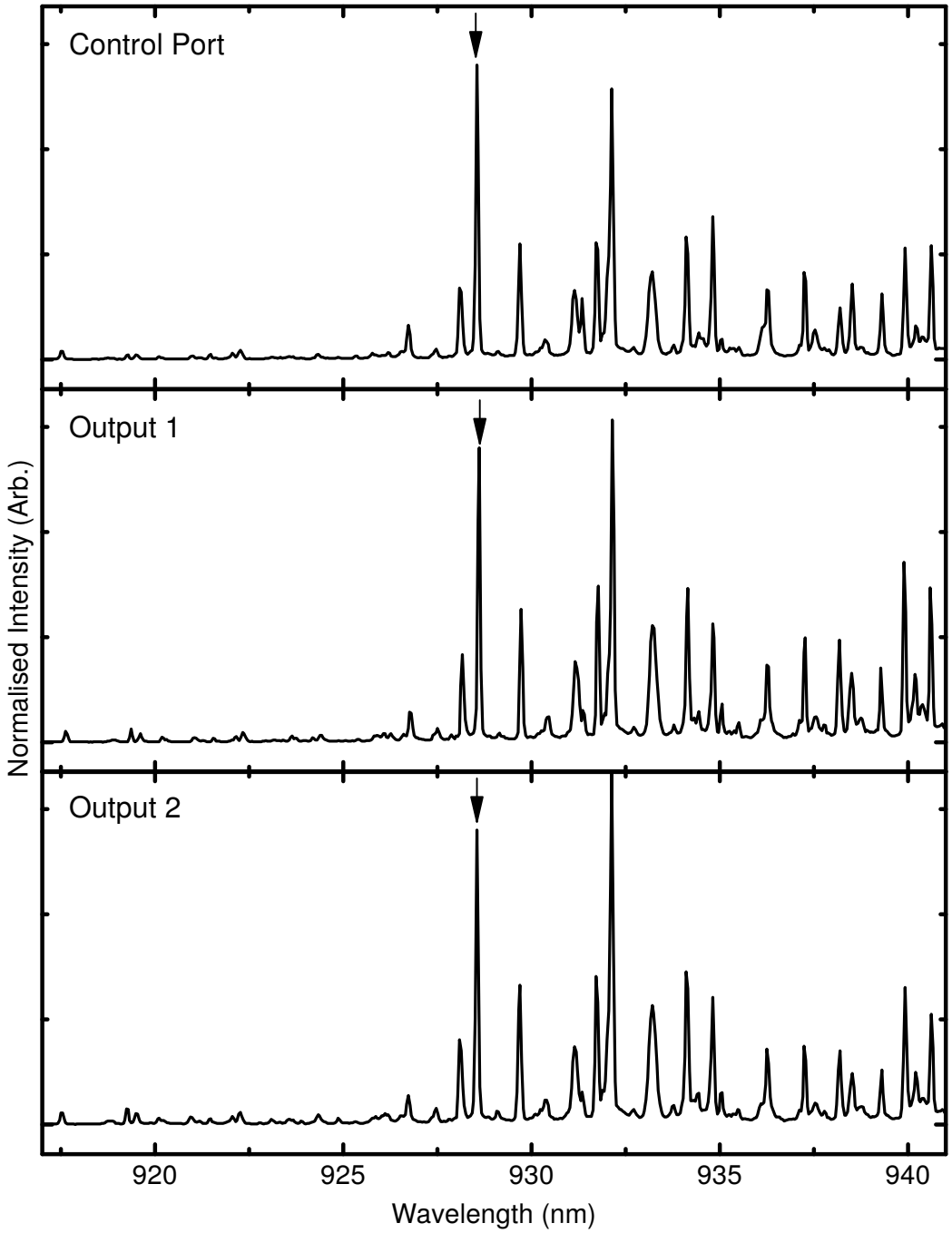

Figure 6.22 – Quantum dot PL emission spectra from the devices input and output ports. An arrow indicates the wavelength of the emission line used in this section. All spectra are normalised to the used QD emission line.

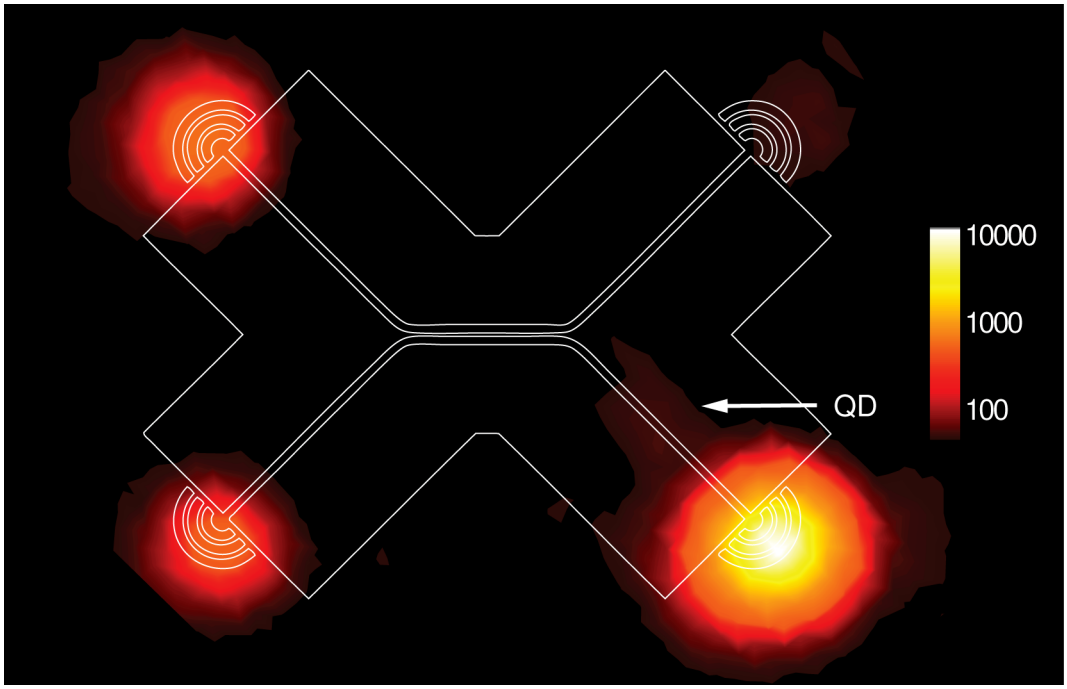

Figure 6.23 – Logarithmic scale photoluminescence map of device B filtered at the QD's wavelength. Map is overlaid with the device contour.

difference between the devices can be attributed to the linewidth, 17 µeV (device B) compared to 11 µeV (device A). Even with a large linewidth the main factor limiting the visibility is still the timing jitter of the detectors. With an SNSPD system, a visibility of 31.5 % is expected for device B.

6.6 Summary and Outlook

In conclusion, the fabrication of an integrated, on-demand, single quantum emitter, a self-assembled quantum dot, and a 50/50 beamsplitter has been demonstrated. The device is used to combine photons originating from an external resonant laser with photons from the a quantum dot embedded within the device. Performing correlation measurements on the device's output ports when both the external laser and quantum dot photons are present reveals the presence of on-chip two-photon interference between the two dissimilar sources. Ultimately the measured performance of the devices presented here is limited by the detection system. It is essential to note that the limitations of the detector system do not effect the envisioned applications of the devices where the generated N00N state will

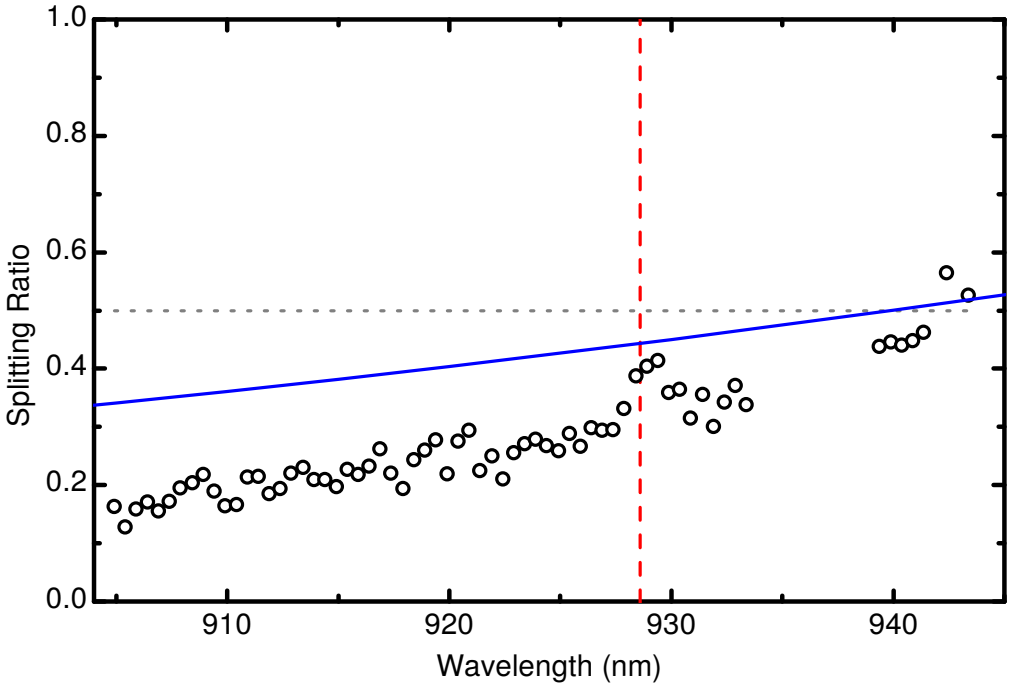

Figure 6.24 – Measured wavelength dependence (circles) of device B's beamsplitter's splitting ratio. Vertical red dashed line indicates the quantum dot's emission wavelength. The blue line is the theoretical wavelength dependence obtained from coupled mode theory for the nominal device design. Grey horizontal line indicates a splitting ratio of 0.5.

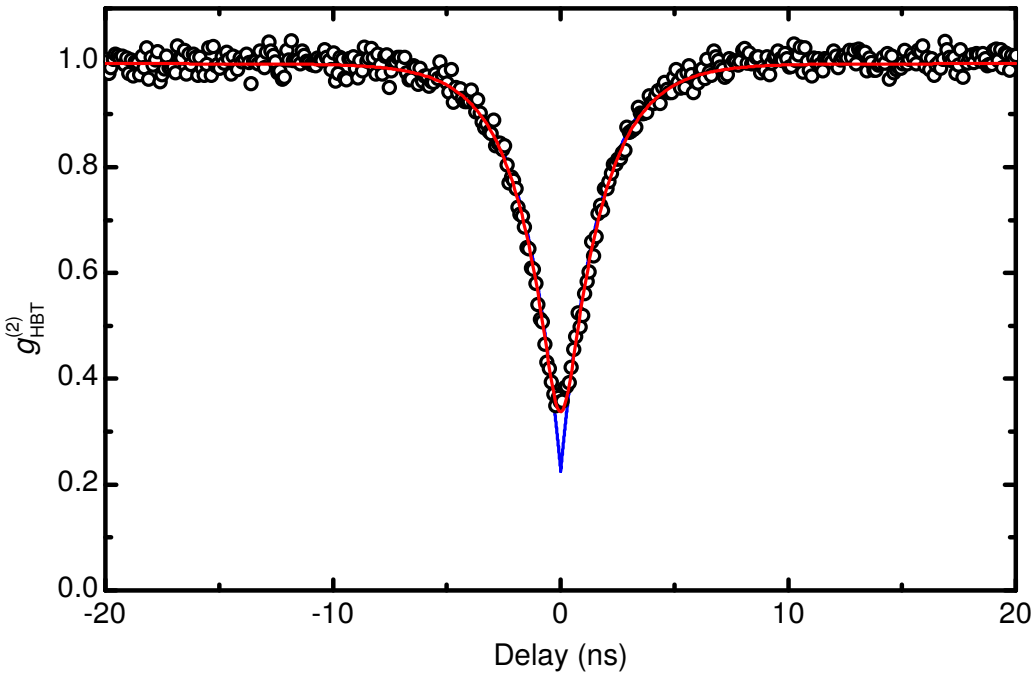

Figure 6.25 – Normalised second order correlation function for the quantum dot in device B measured through the on-chip beamsplitter (symbols) without background subtraction. The red continuous line is a fit to the data taking into account the time response of the detection system. The blue line corresponds to fits in the limit of infinitely fast detectors. The main noise present in the data originates from the single photon counting module.

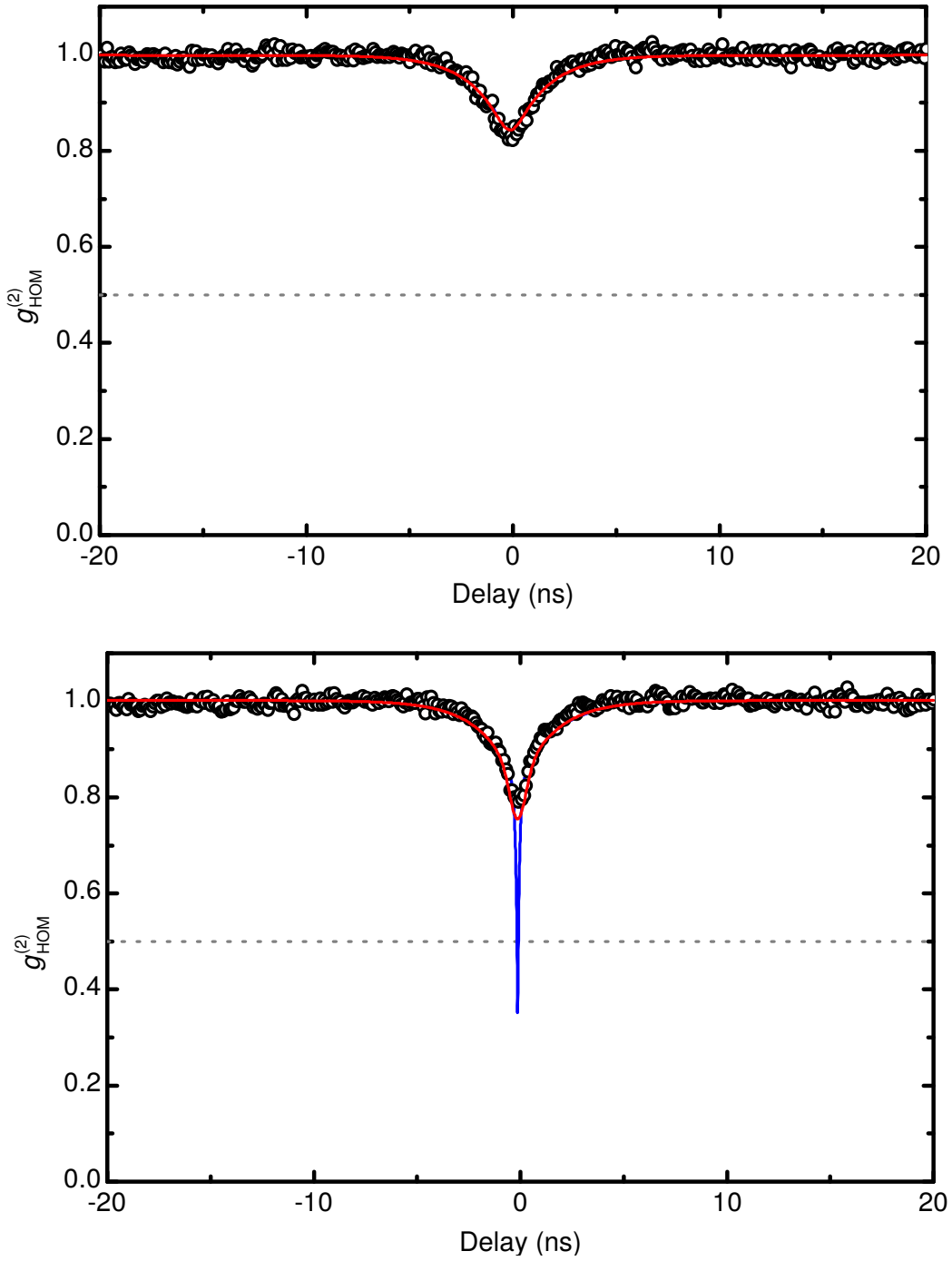

Figure 6.26 – Cross-correlated signal from device B's output ports with the laser tuned a) off resonance with the QD and b) in resonance. Open circles correspond to the experimental data. Red lines are simulated curves using the fitting parameters from the HBT measurements taking into account the detector response. Blue lines correspond to simulated curves with an infinitely fast detector.

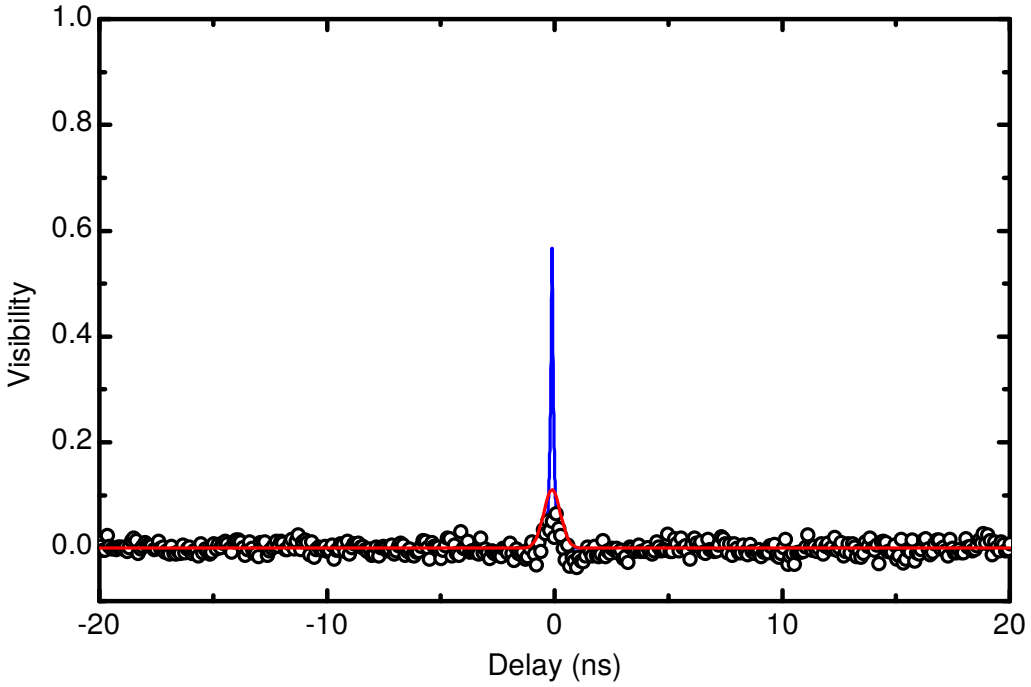

Figure 6.27 – Measured Hong-Ou-Mandel interference visibility (symbols) and simulation (red line) for device B. The blue line corresponds to the theory in the limit of infinitely fast detectors.

be directed into other circuit components. This work paves the way towards demonstration of linear quantum optical circuits with integrated deterministic quantum emitters for quantum computation and/or quantum communication. One proposed application of the experimental approach presented in this chapter is the wafer scale testing of future integrated quantum optical logic gates.

References

[10]E. Knill, R. Laflamme and G. J. Milburn, "A scheme for efficient quantum computation with linear optics", Nature **409**, 46–52 (2001) (see pp. 1, 73, 93).

[15]J. L. O'Brien, A. Furusawa and J. Vučković, "Photonic quantum technologies", Nature Photonics **3**, 687–695 (2009) (see pp. 1, 73, 93).

[21]C. K. Hong, Z. Y. Ou and L. Mandel, "Measurement of subpicosecond time intervals between two photons by interference", Physical Review Letters **59**, 2044 (1987) (see pp. 2, 18, 93).

[53]R. Patel, A. Bennett, I. Farrer, C. Nicoll, D. A. Ritchie and A. J. Shields, "Two-photon interference of the emission from electrically tunable remote quantum dots", Nature Photonics **4**, 632–635 (2010) (see pp. 11, 118).

[82]*Lumerical Solutions, Inc. http://www.lumerical.com/tcad-products/mode/* (see pp. 25, 95).

[110]H. Nakajima, H. Kumano, H. Iijima, S. Odashima and I. Suemune, "Carrier-transfer dynamics between neutral and charged excitonic states in a single quantum dot probed with second-order photon correlation measurements", Physical Review B **88** (2013) 10.1103/PhysRevB.88.045324 (see pp. 44, 115).

[128]M. A. Nielsen, "Optical quantum computation using cluster states", Physical Review Letters **93**, 040503 (2004) (see pp. 73, 93).

[129]S. Tanzilli, A. Martin, F. Kaiser, M. De Micheli, O. Alibart and D. Ostrowsky, "On the genesis and evolution of Integrated Quantum Optics", Laser & Photonics Reviews **6**, 115–143 (2012) (see pp. 73, 93).

[134]N. Prtljaga, R. J. Coles, J. O'Hara, B. Royall, E. Clarke, a. M. Fox and M. S. Skolnick, "Monolithic integration of a quantum emitter with a compact on-chip beam-splitter", Applied Physics Letters **104**, 129–132 (2014) (see pp. 73, 94).

[140]A. Faraon, I. Fushman, D. Englund, N. Stoltz, P. Petroff and J. Vučković, "Dipole induced transparency in waveguide coupled photonic crystal cavities", Optics express **16**, 12154–12162 (2008) (see pp. 78, 100).

[142]U. L. Andersen and T. C. Ralph, "High-Fidelity Teleportation of Continuous-Variable Quantum States Using Delocalized Single Photons", Physical Review Letters **111** (2013) 10.1103/PhysRevLett.111.050504 (see p. 93).

[143]K. Azuma, K. Tamaki and H.-K. Lo, "All-photonic quantum repeaters", Nature Communications **6**, 6787 (2015) (see p. 93).

[144]L. Yu, C. M. Natarajan, T. Horikiri, C. Langrock, J. S. Pelc, M. G. Tanner, E. Abe, S. Maier, C. Schneider, S. Höfling, M. Kamp, R. H. Hadfield, M. M. Fejer and Y. Yamamoto, "Two-photon interference at telecom wavelengths for time-bin-encoded single photons from quantum-dot spin qubits", Nature Communications **6**, 8955 (2015) (see p. 93).

[145]A. Aspuru-Guzik and P. Walther, "Photonic quantum simulators", Nature Physics **8**, 285–291 (2012) (see p. 93).

[146]Q. Quan, P. B. Deotare and M. Loncar, "Photonic crystal nanobeam cavity strongly coupled to the feeding waveguide", Applied Physics Letters **96**, 39–42 (2010) (see pp. 94, 134).

[147]J. C. Chen, H. a Haus, P. R. Villeneuve and J. D. Joannopoulos, *Optical filters from photonic band gap air bridges*, Vol. 14, 11 (1996), 2575–2580 (see p. 94).

[148]U. Rengstl, M. Schwartz, T. Herzog, F. Hargart, M. Paul, S. L. Portalupi, M. Jetter and P. Michler, "On-chip beamsplitter operation on single photons from quasi-resonantly excited quantum dots embedded in GaAs rib waveguides", Applied Physics Letters **107**, 021101 (2015) (see p. 94).

[149]K. D. Jöns, U. Rengstl, M. Oster, F. Hargart, M. Heldmaier, S. Bounouar, S. M. Ulrich, M. Jetter and P. Michler, "Monolithic on-chip integration of semiconductor waveguides, beamsplitters and single-photon sources", Journal of Physics D: Applied Physics **48**, 085101 (2015) (see p. 94).

[150]B. E. A. Saleh and M. C. Teich, "Fundamentals of photonics", NASA STI/Recon Technical Report A **92** (1991) (see p. 95).

[151]a. J. Bennett, R. B. Patel, C. a. Nicoll, D. a. Ritchie and a. J. Shields, "Interference of dissimilar photon sources", Nature Physics **5**, 715–717 (2009) (see pp. 95, 96, 118).

[152]E. B. Flagg, S. V. Polyakov, T. Thomay and G. S. Solomon, "Dynamics of Nonclassical Light from a Single Solid-State Quantum Emitter", Physical Review Letters **109** (2012) 10.1103/PhysRevLett.109.163601 (see p. 106).

[153]P. Gold, A. Thoma, S. Maier, S. Reitzenstein, C. Schneider, S. Höfling and M. Kamp, "Two-photon interference from remote quantum dots with inhomogeneously broadened linewidths", Physical Review B **89** (2014) 10.1103/PhysRevB.89.035313 (see pp. 106, 118).

[154]X. Liu, H. Kumano, H. Nakajima, S. Odashima, T. Asano, T. Kuroda and I. Suemune, "Two-photon interference and coherent control of single InAs quantum dot emissions in an Ag-embedded structure", Journal of Applied Physics **116**, 043103 (2014) (see p. 106).

[155]T. Huber, A. Predojević, D. Föger, G. Solomon and G. Weihs, "Reach of Environmental Influences on the Indistinguishability of Single Photons from Quantum Dots", arXiv preprint arXiv:1507.07404 (2015) (see p. 106).

[156]E. B. Flagg, A. Muller, S. V. Polyakov, A. Ling, A. Migdall and G. S. Solomon, "Interference of Single Photons from Two Separate Semiconductor Quantum Dots", Physical Review Letters **104**, 137401 (2010) (see p. 118).

Chapter 7

Summary and Future Work

7.1 Summary

This thesis has described spectroscopic measurements on single-photon sources integrated with quantum optical circuit components. The devices presented represent steps towards achieving fully integrated quantum optical circuits.

Chapter 2 introduced the basic concepts and background information relating to the use of self-assembled quantum dots (QDs) as integrated sources in III-V semiconductor circuits.

Following this background chapter, Chapter 3 described the computational, fabrication and experimental methods used to perform the experiments presented in the subsequent chapters.

7.1.1 Chapter 4: Waveguide-Coupled H1 Cavities for Single Photon Routing

Chapter 4 presented an on-chip photonic router in which the emission from a single QD can be directed electrically. The device consists of a QD coupled to an H1 cavity with two W1 waveguides. By tuning the applied voltage, the QD emission was shown to be selectively directed into either waveguide, enabling voltage controlled optical routing. The router operation was confirmed with spatially selective spectroscopic measurements and finite-difference time-domain (FDTD) simulations.

7.1.2 Chapter 5: Single-Photon Electroluminescence for On-Chip Quantum Networks

Chapter 5 demonstrated the on-chip spatially selective electrical generation of single photons and their coupling into a suspended nanobeam waveguide. The single photon nature of the source and the propagation of single photons along the waveguide was confirmed with correlation and cross-correlation measurements. Additional high resolution spectra were used to show the highly coherent nature of the source, with coherence properties which should be sufficient to observe non-classical interference.

7.1.3 Chapter 6: On-Chip Interference of Single-Photons from a Quantum Dot and a Laser

Chapter 6 presented work on the on-chip two photon interference between single-photons emitted by an embedded QD and external laser. The QD was monolithically integrated in one arm of a directional coupler which acted as a beamsplitter. The chapter presented modelling of the interference as well as an experimental demonstration of non-classical interference with cross correlation measurements on separate output ports of the the directional coupler.

7.2 Future Work

A number of possible future directions of the work presented in this thesis are summarised here.

7.2.1 On-Chip Filtering and Integration of Superconducting Detectors

The work presented in this thesis has focused on the integration of QD single-photon sources with other optical circuit elements with the development of electroluminescence (EL) based sources and on-chip interference. However, this work has relied upon external filtering with a spectrometer and detection with a charge-coupled device (CCD) camera or single-photon avalanche diode (SPAD). In order to achieve the goal of a fully integrated circuit, this needs to be moved on-chip. A

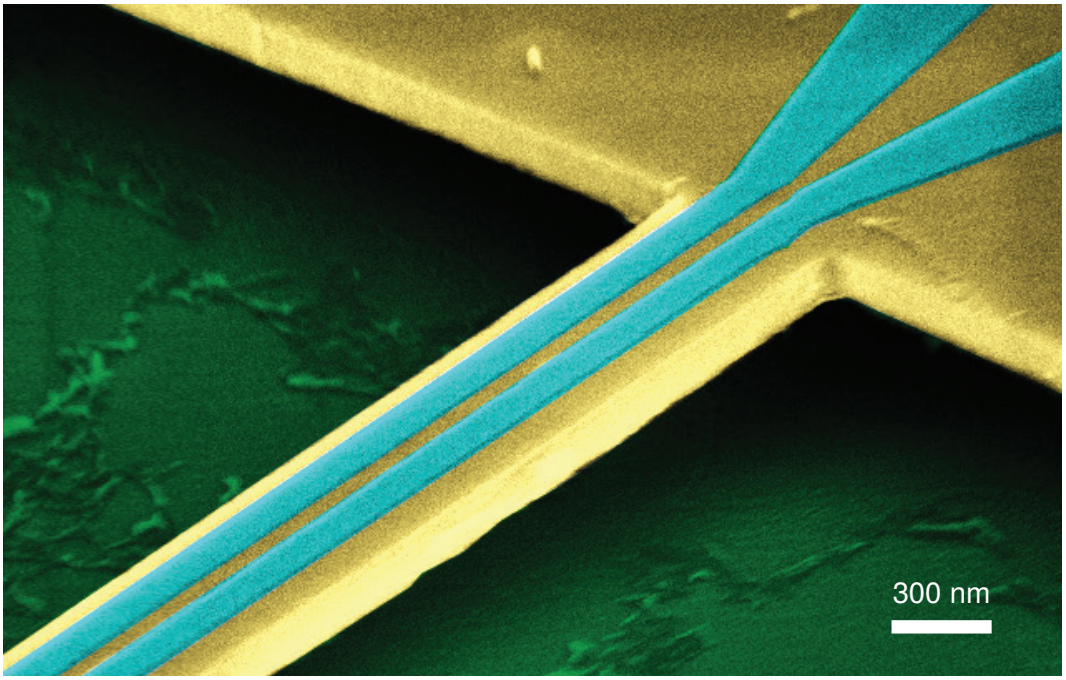

Figure 7.1 – False colour scanning electron microscope image of an SNSPD integrated with a nanobeam waveguide. Blue, green and yellow represent the nanowire detector, underetched region, and membrane, respectively. Device and image produced by the University of Glasgow.

promising candidate for integrated detectors is a superconducting nanowire single photon detector (SNSPD) system. SNSPD systems are ideal as they have a high quantum efficiency at QD wavelengths, low timing jitter and are suitable for integration in a planar geometry[157–161]. These detectors can be integrated by placing the superconducting nanowire on top of a nanobeam waveguide (Figure 7.1).

In order to use on-chip detectors, on-chip filtering is also required due to background emission. The excitation of a single QD state typically involves exciting other QDs or QD states within the same dot due to the large laser spot in photoluminescence (PL) and large biased area in EL. Even quasi-resonant excitation schemes can result in large background due to laser light coupling to the waveguide modes. To be able to measure a single emission line from a quantum dot, this background emission must be filtered out. One possible choice of integrated filter is a one-dimensional photonic crystal in a nanobeam waveguide (Figure 7.2). With such a device, filtering of a single QD emission line is possible due to the

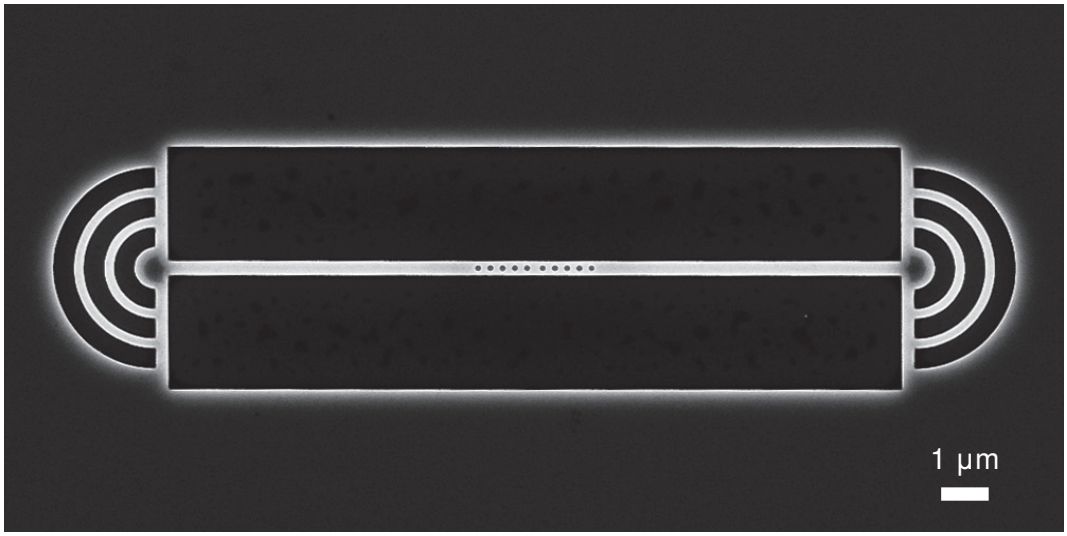

Figure 7.2 – Scanning electron microscope image of a one-dimensional photonic crystal filter within a nanobeam waveguide. Device and image produced by Dr Benjamin Royall.

combination of a large stop band and narrow pass band[146, 162, 163]. Furthermore these filters can be tuned with the use of microelectromechanical systems (MEMS)[164, 165].

7.2.2 On-Chip Two Photon Interference from Embedded Quantum Emitters

One further extension of the work shown here would be the on-chip interference of the emission from two QDs. Although the devices presented in this thesis all contain multiple QDs they are not suitable for two-dot interference due to the large variation in emission wavelength between dots. This is at odds with the requirement that the photons are indistinguishable. The probability of finding two QDs with the same linewidth, wavelength and within a working directional coupler is extremely small. Even if such a device is found, the approach is clearly not scalable and therefore unsuitable for any future devices which may be used for more advanced quantum information processing (QIP) applications utilising many QDs as qubits. A better approach is a design combining a wafer optimised for large quantum-confined Stark effect (QCSE) tuning and a directional coupler. By etching through the p-doped layer in a similar manner to the devices in Chapter

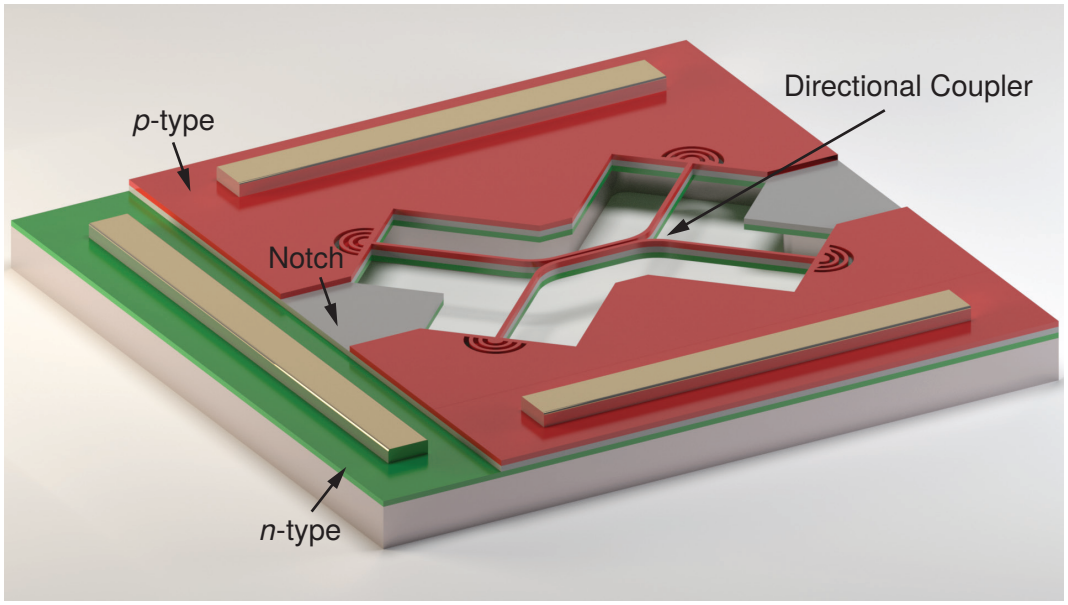

Figure 7.3 – Schematic of a directional coupler with independently electrically tunable emitters. A notch breaks the electrical connection between the two sides of the directional coupler. By applying a voltage to one of the p-type contacts, QDs within that one arm can be tuned independently via the quantum-confined Stark effect.

5, independent tuning of the emission from the two QDs can be achieved. A mock-up of such a device is shown in Figure 7.3. With the ability to tune both QDs by up to 5 nm, the probability of finding multiple quantum emitters producing identical photons is much higher. The tuning range could also be used to tune both QDs to a wavelength at which the directional coupler is closer to 50:50 splitting. Another possible advantage is that the linewidth of the QD may be reduced as the applied electric field can isolate the dots from local charge traps/fluctuation[166, 167].

7.2.3 Further Integration of Electroluminescence Single-Photon Sources

A step forwards from the integration of an electrically driven single-photon source with a nano-beam waveguide is to begin integration with other circuit components. The most interesting component to integrate with the EL source is a directional coupler. Demonstrating two-photon interference occurring in an on-chip beam-

splitter with integrated electrically driven sources would represent a significant step forwards in the field; it would conclusively prove the viability of using EL based single-photon sources in integrated linear optical quantum computing. As discussed previously, the main difficulty in achieving this goal lies in the statistical nature of the QD growth process. In EL, QCSE tuning is possible although the tuning range is typically small due to the device operating in near flat band conditions. One possible solution to this problem is to use registration techniques to locate QDs with similar emission energies prior to device fabrication. Additionally, the wafer design could be optimised for QCSE tuning with the addition of tunnelling barriers.

References

[146]Q. Quan, P. B. Deotare and M. Loncar, "Photonic crystal nanobeam cavity strongly coupled to the feeding waveguide", Applied Physics Letters **96**, 39–42 (2010) (see pp. 94, 134).

[157]R. H. Hadfield, "Single-photon detectors for optical quantum information applications", Nature photonics **3**, 696–705 (2009) (see p. 133).

[158]M. G. Tanner, C. M. Natarajan, V. K. Pottapenjara, J. A. O'Connor, R. J. Warburton, R. H. Hadfield, B. Baek, S. Nam, S. N. Dorenbos, E. B. Ureña, T. Zijlstra, T. M. Klapwijk and V. Zwiller, "Enhanced telecom wavelength single-photon detection with NbTiN superconducting nanowires on oxidized silicon", Applied Physics Letters **96**, 221109 (2010) (see p. 133).

[159]C. M. Natarajan, M. G. Tanner and R. H. Hadfield, "Superconducting nanowire single-photon detectors: physics and applications", Superconductor Science and Technology **25**, 063001 (2012) (see p. 133).

[160]G. Reithmaier, S. Lichtmannecker, T. Reichert, P. Hasch, K. Müller, M. Bichler, R. Gross and J. J. Finley, "On-chip time resolved detection of quantum dot emission using integrated superconducting single photon detectors", Scientific Reports **3** (2013) 10.1038/srep01901 (see p. 133).

[161]G. Reithmaier, M. Kaniber, F. Flassig, S. Lichtmannecker, K. Müller, A. Andrejew, J. Vučković, R. Gross and J. J. Finley, "On-Chip Generation, Routing, and Detection of Resonance Fluorescence", Nano Letters **15**, 5208–5213 (2015) (see p. 133).

[162]J. S. Foresi, P. R. Villeneuve, J. Ferrera, E. R. Thoen, G. Steinmeyer, S. Fan, J. D. Joannopoulos, L. C. Kimerling, H. I. Smith and E. P. Ippen, "Photonic-bandgap microcavities in optical waveguides", Nature **390**, 143–145 (1997) (see p. 134).

[163]Q. Quan and M. Loncar, "Deterministic design of wavelength scale, ultra-high Q photonic crystal nanobeam cavities", Optics express **19**, 18529–18542 (2011) (see p. 134).

[164]P. B. Deotare, M. W. McCutcheon, I. W. Frank, M. Khan and M. Lončar, "Coupled photonic crystal nanobeam cavities", Applied Physics Letters **95**, 031102 (2009) (see p. 134).

[165]X. Chew, G. Zhou, F. S. Chau, J. Deng, X. Tang and Y. C. Loke, "Dynamic tuning of an optical resonator through MEMS-driven coupled photonic crystal nanocavities", Optics letters **35**, 2517–2519 (2010) (see p. 134).

[166]N. Somaschi, V. Giesz, L. De Santis, J. C. Loredo, M. P. Almeida, G. Hornecker, S. L. Portalupi, T. Grange, C. Anton, J. Demory et al., "Near optimal single photon sources in the solid state", arXiv preprint arXiv:1510.06499 (2015) (see p. 135).

[167]V. Giesz, N. Somaschi, G. Hornecker, T. Grange, B. Reznychenko, L. De Santis, J. Demory, C. Gomez, I. Sagnes, A. Lemaitre et al., "Coherent control of a solid-state quantum bit with few-photon pulses", arXiv preprint arXiv:1512.04725 (2015) (see p. 135).

Bibliography

[1]R. P. Feynman, "Simulating physics with computers", International journal of theoretical physics **21**, 467–488 (1982) (see p. 1).

[2]P. W. Shor, "Algorithms for quantum computation: Discrete logarithms and factoring", in Foundations of Computer Science, 1994 Proceedings., 35th Annual Symposium on (1994), pp. 124–134 (see p. 1).

[3]L. K. Grover, "A fast quantum mechanical algorithm for database search", in Proceedings of the twenty-eighth annual ACM symposium on Theory of computing (1996), pp. 212–219 (see p. 1).

[4]J. I. Cirac and P. Zoller, "Quantum computations with cold trapped ions", Physical review letters **74**, 4091 (1995) (see p. 1).

[5]N. A. Gershenfeld and I. L. Chuang, "Bulk spin-resonance quantum computation", science **275**, 350–356 (1997) (see p. 1).

[6]Y. Nakamura, Y. A. Pashkin and J. S. Tsai, "Coherent control of macroscopic quantum states in a single-Cooper-pair box", Nature **398**, 786–788 (1999) (see p. 1).

[7]C. H. W. Barnes, J. M. Shilton and A. M. Robinson, "Quantum computation using electrons trapped by surface acoustic waves", Physical Review B **62**, 8410 (2000) (see p. 1).

[8]T. D. Ladd, F. Jelezko, R. Laflamme, Y. Nakamura, C. Monroe and J. L. O'Brien, "Quantum computers", Nature **464**, 45–53 (2010) (see pp. 1, 73).

[9]J. L. O'Brien, "Optical quantum computing", Science **318**, 1567–1570 (2007) (see p. 1).

[10]E. Knill, R. Laflamme and G. J. Milburn, "A scheme for efficient quantum computation with linear optics", Nature **409**, 46–52 (2001) (see pp. 1, 73, 93).

[11]T. B. Pittman, M. J. Fitch, B. C. Jacobs and J. D. Franson, "Experimental controlled-NOT logic gate for single photons in the coincidence basis", Physical Review A **68** (2003) 10.1103/PhysRevA.68.032316 (see p. 1).

[12]J. L. O'Brien, G. J. Pryde, A. G. White, T. C. Ralph and D. Branning, "Demonstration of an all-optical quantum controlled-NOT gate", Nature **426**, 264–267 (2003) (see p. 1).

[13]A. Politi, M. J. Cryan, J. G. Rarity, S. Yu and J. L. O'Brien, "Silica-on-Silicon Waveguide Quantum Circuits", Science **320**, 646–649 (2008) (see p. 1).

[14]M. A. Pooley, D. J. P. Ellis, R. B. Patel, A. J. Bennett, K. H. A. Chan, I. Farrer, D. A. Ritchie and A. J. Shields, "Controlled-NOT gate operating with single photons", Applied Physics Letters **100**, 211103 (2012) (see p. 1).

[15]J. L. O'Brien, A. Furusawa and J. Vučković, "Photonic quantum technologies", Nature Photonics **3**, 687–695 (2009) (see pp. 1, 73, 93).

[16]A. Crespi, R. Osellame, R. Ramponi, D. J. Brod, E. F. Galvão, N. Spagnolo, C. Vitelli, E. Maiorino, P. Mataloni and F. Sciarrino, "Integrated multimode interferometers with arbitrary designs for photonic boson sampling", Nature Photonics **7**, 545–549 (2013) (see p. 1).

[17]M. Tillmann, B. Dakić, R. Heilmann, S. Nolte, A. Szameit and P. Walther, "Experimental boson sampling", Nature Photonics **7**, 540–544 (2013) (see p. 1).

[18]M. A. Broome, A. Fedrizzi, S. Rahimi-Keshari, J. Dove, S. Aaronson, T. C. Ralph and A. G. White, "Photonic boson sampling in a tunable circuit", Science **339**, 794–798 (2013) (see p. 1).

[19]J. B. Spring, B. J. Metcalf, P. C. Humphreys, W. S. Kolthammer, X.-M. Jin, M. Barbieri, A. Datta, N. Thomas-Peter, N. K. Langford, D. Kundys et al., "Boson sampling on a photonic chip", Science **339**, 798–801 (2013) (see p. 1).

[20]B. T. Gard, K. R. Motes, J. P. Olson, P. P. Rohde and J. P. Dowling, "An Introduction to Boson-Sampling", in *From Atomic to Mesoscale: The Role of Quantum Coherence in Systems of Various Complexities.* Edited by S. A. Malinovskaya and Novikova, I (World Scientific Publishing Co, June 2015), pp. 167–192 (see p. 2).

[21]C. K. Hong, Z. Y. Ou and L. Mandel, "Measurement of subpicosecond time intervals between two photons by interference", Physical Review Letters **59**, 2044 (1987) (see pp. 2, 18, 93).

[22]M. A. Reed, "Spatial quantization in GaAs-AlGaAs multiple quantum dots", Journal of Vacuum Science & Technology B: Microelectronics and Nanometer Structures **4**, 358 (1986) (see p. 7).

[23]D. Leonard, M. Krishnamurthy, C. M. Reaves, S. P. Denbaars and P. M. Petroff, "Direct formation of quantum-sized dots from uniform coherent islands of InGaAs on GaAs surfaces", Applied Physics Letters **63**, 3203–3205 (1993) (see p. 7).

[24]J. Y. Marzin, J. M. Gerard, a. Izrael, D. Barrier and G. Bastard, "Photoluminescence of Single Inas Quantum Dots Obtained by Self- Organized Growth on Gaas", Physical Review Letters **73**, 716–719 (1994) (see pp. 7, 73).

[25]B. Lounis, H. Bechtel, D. Gerion, P. Alivisatos and W. Moerner, "Photon antibunching in single CdSe/ZnS quantum dot fluorescence", Chemical Physics Letters **329**, 399–404 (2000) (see p. 7).

[26]G. Chen, T. H. Stievater, E. T. Batteh, X. Li, D. G. Steel, D. Gammon, D. S. Katzer, D. Park and L. J. Sham, "Biexciton quantum coherence in a single quantum dot.", Physical review letters **88**, 117901 (2002) (see p. 7).

[27]W. Izumida, O. Sakai and S. Tarucha, "Tunneling through a quantum dot in local spin singlet-triplet crossover region with Kondo effect.", Physical review letters **87**, 216803 (2001) (see p. 7).

[28]Q. Xie, A. Madhukar, P. Chen and N. Kobayashi, "Vertically Self-Organized InAs Quantum Box Islands on GaAs(100)", Physical Review Letters **75**, 2542–2545 (1995) (see p. 7).

[29]K. Sebald, P. Michler, T. Passow, D. Hommel, G. Bacher and a. Forchel, "Single-photon emission of CdSe quantum dots at temperatures up to 200 K", Applied Physics Letters **81**, 2920–2922 (2002) (see p. 7).

[30]F. Tinjod, B. Gilles, S. Moehl, K. Kheng and H. Mariette, "II-VI quantum dot formation induced by surface energy change of a strained layer", Applied Physics Letters **82**, 4340–4342 (2003) (see p. 7).

[31]K. Brunner, "Si/Ge nanostructures", Reports on Progress in Physics **65**, 27 (2002) (see p. 7).

[32]P. Michler, A. Kiraz, C. Becher, W. V. Schoenfeld, P. M. Petroff, L. Zhang, E. Hu and A. İmamoğlu, "A Quantum Dot Single-Photon Turnstile Device", Science **290**, 2282–2285 (2000) (see pp. 7, 73).

[33]V. Zwiller, H. Blom, P. Jonsson, N. Panev, S. Jeppesen, T. Tsegaye, E. Goobar, M.-E. Pistol, L. Samuelson and G. Björk, "Single quantum dots emit single photons at a time: Antibunching experiments", Applied Physics Letters **78**, 2476 (2001) (see p. 7).

[34]Z. Yuan, B. E. Kardynal, R. M. Stevenson, A. J. Shields, C. J. Lobo, K. Cooper, N. S. Beattie, D. A. Ritchie and M. Pepper, "Electrically Driven Single-Photon Source", Science **295**, 102–105 (2002) (see pp. 7, 73).

[35]M. Pelton, C. Santori, J. Vučković, B. Zhang, G. S. Solomon, J. Plant and Y. Yamamoto, "Efficient Source of Single Photons: A Single Quantum Dot in a Micropost Microcavity", Physical Review Letters **89** (2002) 10.1103/PhysRevLett.89.233602 (see pp. 7, 73).

[36]C. Santori, D. Fattal, J. Vuckovic, G. S. Solomon and Y. Yamamoto, "Single-photon generation with InAs quantum dots", New Journal of Physics **6**, 89–89 (2004) (see p. 7).

[37]W.-H. Chang, W.-Y. Chen, H.-S. Chang, T.-P. Hsieh, J.-I. Chyi and T.-M. Hsu, "Efficient Single-Photon Sources Based on Low-Density Quantum Dots in Photonic-Crystal Nanocavities", Physical Review Letters **96** (2006) 10.1103/PhysRevLett.96.117401 (see pp. 7, 73).

[38]S. Strauf, N. G. Stoltz, M. T. Rakher, L. A. Coldren, P. M. Petroff and D. Bouwmeester, "High-frequency single-photon source with polarization control", Nature Photonics **1**, 704–708 (2007) (see pp. 7, 73).

[39]A. P. Alivisatos, "Semiconductor clusters, nanocrystals, and quantum dots", Science **271**, 933 (1996) (see p. 8).

[40]S. Guha, A. Madhukar and K. C. Rajkumar, "Onset of incoherency and defect introduction in the initial stages of molecular beam epitaxical growth of highly strained InxGa1=xAs on GaAs(100)", Applied Physics Letters **57**, 2110 (1990) (see p. 8).

[41]G. A. Narvaez, G. Bester and A. Zunger, "Dependence of the electronic structure of self-assembled (In, Ga)As/GaAs quantum dots on height and composition", Journal of Applied Physics **98**, 043708 (2005) (see p. 8).

[42]W. Sheng and J.-P. Leburton, "Electron-hole alignment in InAs/GaAs self-assembled quantum dots: Effects of chemical composition and dot shape", Physical Review B **63** (2001) 10.1103/PhysRevB.63.161301 (see p. 8).

[43]P. Michler, *Single Quantum Dots: Fundamentals, Applications and New Concepts*, Vol. 90 (Springer Science & Business Media, 2003) (see p. 8).

[44]A. Milnes and A. Polyakov, "Indium arsenide: a semiconductor for high speed and electro-optical devices", Materials Science and Engineering: B **18**, 237–259 (1993) (see p. 9).

[45]A. Zrenner, "A close look on single quantum dots", The journal of chemical physics **112**, 7790–7798 (2000) (see pp. 9, 28).

[46]R. Thompson, R. Stevenson, A. Shields, I. Farrer, C. Lobo, D. Ritchie, M. Leadbeater and M. Pepper, "Single-photon emission from exciton complexes in individual quantum dots", Physical Review B **64**, 201302 (2001) (see pp. 9, 10).

[47]O. Benson, C. Santori, M. Pelton and Y. Yamamoto, "Regulated and entangled photons from a single quantum dot", Physical review letters **84**, 2513 (2000) (see pp. 10, 78).

[48]R. M. Stevenson, R. J. Young, P. Atkinson, K. Cooper, D. A. Ritchie and A. J. Shields, "A semiconductor source of triggered entangled photon pairs", Nature **439**, 179–182 (2006) (see p. 10).

[49]A. J. Hudson, R. M. Stevenson, A. J. Bennett, R. J. Young, C. A. Nicoll, P. Atkinson, K. Cooper, D. A. Ritchie and A. J. Shields, "Coherence of an Entangled Exciton-Photon State", Physical Review Letters **99** (2007) 10.1103/PhysRevLett.99.266802 (see p. 10).

[50]M. Ward, M. Dean, R. Stevenson, A. Bennett, D. Ellis, K. Cooper, I. Farrer, C. Nicoll, D. Ritchie and A. Shields, "Coherent dynamics of a telecom-wavelength entangled photon source", Nature Communications **5** (2014) 10.1038/ncomms4316 (see p. 10).

[51]D. a. B. Miller, D. S. Chemla, T. C. Damen, a. C. Gossard, W. Wiegmann, T. H. Wood and C. a. Burrus, "Band-edge electroabsorption in quantum well structures: The quantum-confined stark effect", Physical Review Letters **53**, 2173–2176 (1984) (see p. 11).

[52]A. J. Bennett, R. B. Patel, J. Skiba-Szymanska, C. A. Nicoll, I. Farrer, D. A. Ritchie and A. J. Shields, "Giant Stark effect in the emission of single semiconductor quantum dots", Applied Physics Letters **97**, 1–4 (2010) (see pp. 11, 60).

[53]R. Patel, A. Bennett, I. Farrer, C. Nicoll, D. A. Ritchie and A. J. Shields, "Two-photon interference of the emission from electrically tunable remote quantum dots", Nature Photonics **4**, 632–635 (2010) (see pp. 11, 118).

[54]P. Lodahl, S. Mahmoodian and S. Stobbe, "Interfacing single photons and single quantum dots with photonic nanostructures", Reviews of Modern Physics **87**, 347 (2015) (see p. 13).

[55]E. M. Purcell, "Spontaneous emission probabilities at radio frequencies", Physical Review B **69**, 681 (1946) (see pp. 13, 64).

[56]E. T. Jaynes and F. W. Cummings, "Comparison of quantum and semiclassical radiation theories with application to the beam maser", Proceedings of the IEEE **51**, 89–109 (1963) (see p. 14).

[57]I. I. Rabi, "Space quantization in a gyrating magnetic field", Physical Review **51**, 652 (1937) (see p. 14).

[58]J. Hopfield, "Theory of the contribution of excitons to the complex dielectric constant of crystals", Physical Review **112**, 1555 (1958) (see p. 14).

[59]G. Cui and M. G. Raymer, "Quantum efficiency of single-photon sources in the cavity-QED strong-coupling regime", Optics express **13**, 9660–9665 (2005) (see p. 14).

[60]D. Press, S. Götzinger, S. Reitzenstein, C. Hofmann, A. Löffler, M. Kamp, A. Forchel and Y. Yamamoto, "Photon antibunching from a single quantum-dot-microcavity system in the strong coupling regime", Physical Review Letters **98**, 117402 (2007) (see p. 14).

[61]A. Kiraz, P. Michler, C. Becher, B. Gayral, A. İmamoğlu, L. Zhang, E. Hu, W. V. Schoenfeld and P. M. Petroff, "Cavity-quantum electrodynamics using a single InAs quantum dot in a microdisk structure", Applied Physics Letters **78**, 3932–3934 (2001) (see pp. 14, 56).

[62]T. Yoshie, A. Scherer, J. Hendrickson, G. Khitrova, H. Gibbs, G. Rupper, C. Ell, O. Shchekin and D. Deppe, "Vacuum Rabi splitting with a single quantum dot in a photonic crystal nanocavity", Nature **432**, 200–203 (2004) (see p. 14).

[63]J. P. Reithmaier, G. Sęk, A. Löffler, C. Hofmann, S. Kuhn, S. Reitzenstein, L. V. Keldysh, V. D. Kulakovskii, T. L. Reinecke and A. Forchel, "Strong coupling in a single quantum dot–semiconductor microcavity system", Nature **432**, 197–200 (2004) (see p. 14).

[64]K. Hennessy, A. Badolato, M. Winger, D. Gerace, M. Atatüre, S. Gulde, S. Fält, E. L. Hu and A. İmamoğlu, "Quantum nature of a strongly coupled single quantum dot–cavity system", Nature **445**, 896–899 (2007) (see pp. 14, 16).

[65]E. Yablonovitch, "Inhibited spontaneous emission in solid-state physics and electronics", Physical review letters **58**, 2059 (1987) (see p. 14).

[66]S. John, "Strong localization of photons in certain disordered dielectric superlattices", Physical review letters **58**, 2486 (1987) (see p. 14).

[67]L. Rayleigh, "XVII. On the maintenance of vibrations by forces of double frequency, and on the propagation of waves through a medium endowed with a periodic structure", The London, Edinburgh, and Dublin Philosophical Magazine and Journal of Science **24**, 145–159 (1887) (see p. 15).

[68]E. Yablonovitch, T. Gmitter, R. Meade, A. Rappe, K. Brommer and J. Joannopoulos, "Donor and acceptor modes in photonic band structure", Physical Review Letters **67**, 3380 (1991) (see p. 16).

[69]H. Sekoguchi, Y. Takahashi, T. Asano and S. Noda, "Photonic crystal nanocavity with a Q-factor of̃ 9 million", Optics express **22**, 916–924 (2014) (see p. 16).

[70]H. Takagi, Y. Ota, N. Kumagai, S. Ishida, S. Iwamoto and Y. Arakawa, "High Q H1 photonic crystal nanocavities with efficient vertical emission", Optics express **20**, 28292–28300 (2012) (see p. 16).

[71] A. Mekis, J. Chen, I. Kurland, S. Fan, P. R. Villeneuve and J. Joannopoulos, "High transmission through sharp bends in photonic crystal waveguides", Physical Review Letters **77**, 3787 (1996) (see p. 17).

[72] S. J. McNab, N. Moll and Y. A. Vlasov, "Ultra-low loss photonic integrated circuit with membrane-type photonic crystal waveguides", Optics express **11**, 2927–2939 (2003) (see p. 17).

[73] Y. A. Vlasov, M. O'Boyle, H. F. Hamann and S. J. McNab, "Active control of slow light on a chip with photonic crystal waveguides", Nature **438**, 65–69 (2005) (see p. 17).

[74] S. McNab and Y. Vlasov, "Coupling into the slow light mode in slab-type photonic crystal waveguides", Optics letters: A publication of the Optical Society of America, 50–52 (2006) (see p. 17).

[75] M. Banaee, A. Pattantyus-Abraham, M. McCutcheon, G. Rieger and J. F. Young, "Efficient coupling of photonic crystal microcavity modes to a ridge waveguide", Applied physics letters **90**, 193106 (2007) (see p. 17).

[76] J.-P. Hugonin, P. Lalanne, T. P. White and T. F. Krauss, "Coupling into slow-mode photonic crystal waveguides", Optics letters **32**, 2638–2640 (2007) (see p. 17).

[77] P. Kok, W. J. Munro, K. Nemoto, T. C. Ralph, J. P. Dowling and G. J. Milburn, "Linear optical quantum computing with photonic qubits", Reviews of Modern Physics **79**, 135–174 (2007) (see p. 17).

[78] A. Taflove, S. C. Hagness et al., "Computational electrodynamics: the finite-difference time-domain method", Norwood, 2nd Edition, MA: Artech House, l995 (1995) (see p. 25).

[79] A. F. Oskooi, D. Roundy, M. Ibanescu, P. Bermel, J. D. Joannopoulos and S. G. Johnson, "Meep: A flexible free-software package for electromagnetic simulations by the FDTD method", Computer Physics Communications **181**, 687–702 (2010) (see pp. 25, 57).

[80] *Lumerical Solutions, Inc. http://www.lumerical.com/tcad-products/fdtd/* (see pp. 25, 79).

[81]S. Johnson and J. D. Joannopoulos, "Block-iterative frequency-domain methods for Maxwell's equations in a planewave basis", Opt. Express **8**, 173–190 (2001) (see p. 25).

[82]*Lumerical Solutions, Inc. http://www.lumerical.com/tcad-products/mode/* (see pp. 25, 95).

[83]R. Nötzel, "Self-organized growth of quantum-dot structures", Semiconductor Science and Technology **11**, 1365 (1996) (see p. 26).

[84]A. Cho and J. Arthur, "Molecular beam epitaxy", Progress in solid state chemistry **10**, 157–191 (1975) (see p. 26).

[85]I. Stranski and L. Krastanow, "Abhandlungen der mathematisch-naturwissenschaftlichen klasse IIb", Akademie der Wissenschaften Wien **146**, 797–810 (1938) (see p. 26).

[86]E. Bauer, "Phänomenologische theorie der kristallabscheidung an oberflächen. II", Zeitschrift für Kristallographie-Crystalline Materials **110**, 395–431 (1958) (see p. 26).

[87]L. Goldstein, F. Glas, J. Y. Marzin, M. N. Charasse and G. Le Roux, "Growth by molecular beam epitaxy and characterization of InAs/GaAs strained-layer superlattices", Applied Physics Letters **47**, 1099 (1985) (see p. 26).

[88]R. Asaro and W. Tiller, "Interface morphology development during stress corrosion cracking: Part I. Via surface diffusion", Metallurgical Transactions **3**, 1789–1796 (1972) (see p. 26).

[89]M. A. Grinfeld, "Instability of the separation boundary between a non-hydrostatically stressed body and a melt", Sov. Phys. Dokl. **31**, 831–834 (1986) (see p. 26).

[90]M. Bayer, G. Ortner, O. Stern, A. Kuther, A. A. Gorbunov, A. Forchel, P. Hawrylak, S. Fafard, K. Hinzer, T. L. Reinecke, S. N. Walck, J. P. Reithmaier, F. Klopf and F. Schäfer, "Fine structure of neutral and charged excitons in self-assembled In(Ga)As/(Al)GaAs quantum dots", Physical Review B **65** (2002) 10.1103/PhysRevB.65.195315 (see p. 28).

[91]S. Golka, C. Pflügl, W. Schrenk and G. Strasser, "Quantum cascade lasers with lateral double-sided distributed feedback grating", Applied Physics Letters **86**, 111103 (2005) (see pp. 30, 31).

[92]R. Shul, G. McClellan, R. Briggs, D. Rieger, S. Pearton, C. Abernathy, J. Lee, C. Constantine and C. Barratt, "High-density plasma etching of compound semiconductors", Journal of Vacuum Science & Technology A **15**, 633–637 (1997) (see p. 31).

[93]R. Braive, L. Le Gratiet, S. Guilet, G. Patriarche, A. Lemaître, A. Beveratos, I. Robert-Philip and I. Sagnes, "Inductively coupled plasma etching of GaAs suspended photonic crystal cavities", Journal of vacuum science & technology B **27**, 1909–1914 (2009) (see p. 31).

[94]M. Balooch, D. Olander and W. Siekhaus, "The thermal and ion-assisted reactions of GaAs (100) with molecular chlorine", Journal of Vacuum Science & Technology B **4**, 794–805 (1986) (see p. 31).

[95]E. Hu and R. Howard, "Reactive ion etching of GaAs in a chlorine plasma", Journal of Vacuum Science & Technology B **2**, 85–88 (1984) (see p. 31).

[96]S. Golka, S. Schartner, W. Schrenk, G. Strasser et al., "Low bias reactive ion etching of GaAs with a SiCl4/N-2/O-2 time-multiplexed process", Journal of Vacuum Science & Technology B **25**, 839–844 (2007) (see p. 31).

[97]S. Golka, M. Arens, M. Reetz, T. Kwapien, S. Bouchoule and G. Patriarche, "Time-multiplexed, inductively coupled plasma process with separate SiCl4 and O2 steps for etching of GaAs with high selectivity", Journal of Vacuum Science & Technology B **27**, 2270–2279 (2009) (see p. 31).

[98]P. Kumar, S. Kanakaraju and D. DeVoe, "Sacrificial etching of AlxGa1-xAs for III–V MEMS surface micromachining", Applied Physics A **88**, 711–714 (2007) (see p. 31).

[99]A. Cohen, "Critical point drying-principles and procedures", Scanning electron microscopy, 303–24 (1979) (see p. 31).

[100]R. Heitz, M. Veit, N. N. Ledentsov, A. Hoffmann, D. Bimberg, V. M. Ustinov, P. S. Kop′ev and Z. I. Alferov, "Energy relaxation by multiphonon processes in InAs/GaAs quantum dots", Physical Review B **56**, 10435 (1997) (see p. 39).

[101]N. H. Bonadeo, J. Erland, D. Gammon, D. Park, D. Katzer and D. Steel, "Coherent optical control of the quantum state of a single quantum dot", Science **282**, 1473–1476 (1998) (see p. 40).

[102]C. Santori, D. Fattal, J. Vučković, G. S. Solomon and Y. Yamamoto, "Indistinguishable photons from a single-photon device", Nature **419**, 594–597 (2002) (see p. 40).

[103]S. Sauvage, P. Boucaud, R. Lobo, F. Bras, G. Fishman, R. Prazeres, F. Glotin, J. Ortega and J.-M. Gérard, "Long polaron lifetime in InAs/GaAs self-assembled quantum dots", Physical review letters **88**, 177402 (2002) (see p. 40).

[104]E. Zibik, L. Wilson, R. Green, G. Bastard, R. Ferreira, P. Phillips, D. Carder, J. R. Wells, M. Skolnick, J. Cockburn et al., "The polaronic nature of intraband relaxation in InAs/GaAs self-assembled quantum dots", Physica E: Low-dimensional Systems and Nanostructures **26**, 408–412 (2005) (see p. 40).

[105]K. Kuroda, T. Kuroda, K. Watanabe, T. Mano, K. Sakoda, G. Kido and N. Koguchi, "Final-state readout of exciton qubits by observing resonantly excited photoluminescence in quantum dots", Applied physics letters **90**, 051909 (2007) (see p. 40).

[106]A. Muller, E. B. Flagg, P. Bianucci, X. Y. Wang, D. G. Deppe, W. Ma, J. Zhang, G. J. Salamo, M. Xiao and C. K. Shih, "Resonance Fluorescence from a Coherently Driven Semiconductor Quantum Dot in a Cavity", Physical Review Letters **99** (2007) 10.1103/PhysRevLett.99.187402 (see p. 40).

[107]E. Siebert, T. Warming, A. Schliwa, E. Stock, M. Winkelnkemper, S. Rodt and D. Bimberg, "Spectroscopic access to single-hole energies in InAs/GaAs quantum dots", Physical Review B **79** (2009) 10.1103/PhysRevB.79.205321 (see p. 40).

[108]T. Warming, E. Siebert, A. Schliwa, E. Stock, R. Zimmermann and D. Bimberg, "Hole-hole and electron-hole exchange interactions in single InAs/GaAs quantum dots", Physical Review B **79** (2009) 10.1103/PhysRevB.79.125316 (see p. 40).

[109]Y. Benny, Y. Kodriano, E. Poem, D. Gershoni, T. A. Truong and P. M. Petroff, "Excitation spectroscopy of single quantum dots at tunable positive, neutral, and negative charge states", Physical Review B **86** (2012) 10.1103/PhysRevB.86.085306 (see p. 40).

[110]H. Nakajima, H. Kumano, H. Iijima, S. Odashima and I. Suemune, "Carrier-transfer dynamics between neutral and charged excitonic states in a single

quantum dot probed with second-order photon correlation measurements", Physical Review B **88** (2013) 10.1103/PhysRevB.88.045324 (see pp. 44, 115).

[111]I. Rech, I. Labanca, M. Ghioni and S. Cova, "Modified single photon counting modules for optimal timing performance", Review of Scientific Instruments **77**, 033104 (2006) (see p. 45).

[112]A. Schwagmann, S. Kalliakos, I. Farrer, J. P. Griffiths, G. A. Jones, D. A. Ritchie and A. J. Shields, "On-chip single photon emission from an integrated semiconductor quantum dot into a photonic crystal waveguide", Applied Physics Letters **99**, 261108 (2011) (see pp. 55, 73).

[113]M. N. Makhonin, J. E. Dixon, R. J. Coles, B. Royall, I. J. Luxmoore, E. Clarke, M. Hugues, M. S. Skolnick and A. M. Fox, "Waveguide Coupled Resonance Fluorescence from On-Chip Quantum Emitter", Nano Letters **14**, 6997–7002 (2014) (see pp. 55, 73).

[114]S. Kalliakos, Y. Brody, A. Schwagmann, A. J. Bennett, M. B. Ward, D. J. P. Ellis, J. Skiba-Szymanska, I. Farrer, J. P. Griffiths, G. A. C. Jones, D. A. Ritchie and A. J. Shields, "In-plane emission of indistinguishable photons generated by an integrated quantum emitter", Applied Physics Letters **104**, 221109 (2014) (see pp. 55, 73).

[115]R. J. Coles, N. Prtljaga, B. Royall, I. J. Luxmoore, a. M. Fox and M. S. Skolnick, "Waveguide-coupled photonic crystal cavity for quantum dot spin readout", Optics Express **22**, 2376–2385 (2014) (see pp. 56, 57).

[116]S. Mosor, J. Hendrickson, B. C. Richards, J. Sweet, G. Khitrova, H. M. Gibbs, T. Yoshie, a. Scherer, O. B. Shchekin and D. G. Deppe, "Scanning a photonic crystal slab nanocavity by condensation of xenon", Applied Physics Letters **87**, 1–3 (2005) (see p. 56).

[117]P. W. Fry, I. E. Itskevich, D. J. Mowbray, M. S. Skolnick, J. J. Finley, J. a Barker, E. P. O'Reilly, L. R. Wilson, I. a Larkin, P. a Maksym, M. Hopkinson, M. Al-Khafaji, J. P. David, a. G. Cullis, G. Hill and J. C. Clark, "Inverted electron-hole alignment in InAs-GaAs self-assembled quantum dots.", Physical review letters **84**, 733–736 (2000) (see p. 56).

[118] A. Laucht, F. Hofbauer, N. Hauke, J. Angele, S. Stobbe, M. Kaniber, G. Böhm, P. Lodahl, M.-C. C. Amann and J. J. Finley, "Electrical control of spontaneous emission and strong coupling for a single quantum dot", New Journal of Physics **11**, 023034 (2009) (see pp. 56, 61, 64).

[119] M. Shirane, S. Kono, J. Ushida, S. Ohkouchi, N. Ikeda, Y. Sugimoto and A. Tomita, "Mode identification of high-quality-factor single-defect nanocavities in quantum dot-embedded photonic crystals", Journal of Applied Physics **101**, 073107–073107–7 (2007) (see p. 57).

[120] V. A. Mandelshtam and H. S. Taylor, "Harmonic inversion of time signals and its applications", The Journal of Chemical Physics **107**, 6756 (1997) (see p. 58).

[121] A. Faraon, E. Waks, D. Englund, I. Fushman and J. Vuckovic, "Efficient photonic crystal cavity-waveguide couplers", Appl. Phys. Lett. **90**, 73102 (2007) (see p. 58).

[122] M. Kaniber, A. Laucht, A. Neumann, J. M. Villas-Bôas, M. Bichler, M. C. Amann and J. J. Finley, "Investigation of the nonresonant dot-cavity coupling in two-dimensional photonic crystal nanocavities", Physical Review B - Condensed Matter and Materials Physics **77**, 1–4 (2008) (see p. 62).

[123] A. Badolato, M. Winger, K. J. Hennessy, E. L. Hu and A. İmamoğlu, "Cavity QED effects with single quantum dots", Comptes Rendus Physique **9**, 850–856 (2008) (see p. 62).

[124] M. Winger, T. Volz, G. Tarel, S. Portolan, A. Badolato, K. J. Hennessy, E. L. Hu, A. Beveratos, J. Finley, V. Savona and A. İmamoğlu, "Explanation of photon correlations in the far-off-resonance optical emission from a quantum-dot-cavity system", Physical Review Letters **103**, 11–14 (2009) (see p. 62).

[125] B. Gayral and J. M. Gérard, "Photoluminescence experiment on quantum dots embedded in a large Purcell-factor microcavity", Physical Review B - Condensed Matter and Materials Physics **78**, 1–7 (2008) (see p. 64).

[126] H. J. Kimble, "The quantum internet", Nature **453**, 1023–1030 (2008) (see p. 73).

[127] N. Gisin, G. Ribordy, W. Tittel and H. Zbinden, "Quantum cryptography", Reviews of modern physics **74**, 145 (2002) (see p. 73).

[128]M. A. Nielsen, "Optical quantum computation using cluster states", Physical Review Letters **93**, 040503 (2004) (see pp. 73, 93).

[129]S. Tanzilli, A. Martin, F. Kaiser, M. De Micheli, O. Alibart and D. Ostrowsky, "On the genesis and evolution of Integrated Quantum Optics", Laser & Photonics Reviews **6**, 115–143 (2012) (see pp. 73, 93).

[130]E. Dekel, D. Gershoni, E. Ehrenfreund, D. Spektor, J. M. Garcia and P. M. Petroff, "Multiexciton spectroscopy of a single self-assembled quantum dot", Physical review letters **80**, 4991 (1998) (see p. 73).

[131]Y. Toda, S. Shinomori, K. Suzuki and Y. Arakawa, "Near-field magneto-optical spectroscopy of single self-assembled InAs quantum dots", Applied Physics Letters **73**, 517 (1998) (see p. 73).

[132]A. Kuther, M. Bayer, A. Forchel, A. Gorbunov, V. B. Timofeev, F. Schäfer and J. P. Reithmaier, "Zeeman splitting of excitons and biexcitons in single $In_{0.60}Ga_{0.40}As$/GaAs self-assembled quantum dots", Phys. Rev. B **58**, R7508–R7511 (1998) (see p. 73).

[133]I. E. Itskevich, S. I. Rybchenko, I. I. Tartakovskii, S. T. Stoddart, A. Levin, P. C. Main, L. Eaves, M. Henini and S. Parnell, "Stark shift in electroluminescence of individual InAs quantum dots", Applied Physics Letters **76**, 3932 (2000) (see p. 73).

[134]N. Prtljaga, R. J. Coles, J. O'Hara, B. Royall, E. Clarke, a. M. Fox and M. S. Skolnick, "Monolithic integration of a quantum emitter with a compact on-chip beam-splitter", Applied Physics Letters **104**, 129–132 (2014) (see pp. 73, 94).

[135]R. B. Patel, A. J. Bennett, K. Cooper, P. Atkinson, C. A. Nicoll, D. A. Ritchie and A. J. Shields, "Postselective Two-Photon Interference from a Continuous Nonclassical Stream of Photons Emitted by a Quantum Dot", Physical Review Letters **100**, 207405 (2008) (see pp. 74, 83).

[136]D. Pinotsi, P. Fallahi, J. Miguel-Sanchez and A. İmamoğlu, "Resonant Spectroscopy on Charge Tunable Quantum Dots in Photonic Crystal Structures", IEEE Journal of Quantum Electronics **47**, 1371–1374 (2011) (see pp. 74, 83).

[137]L. Turyanska, A. Baumgartner, A. Chaggar, A. Patanè, L. Eaves and M. Henini, "Sharp-line electroluminescence from individual quantum dots by resonant tunneling injection of carriers", Applied Physics Letters **89**, 092106 (2006) (see p. 78).

[138]A. Baumgartner, E. Stock, A. Patanè, L. Eaves, M. Henini and D. Bimberg, "Optical Imaging of Electrical Carrier Injection into Individual InAs Quantum Dots", Physical Review Letters **105** (2010) 10.1103/PhysRevLett.105.257401 (see p. 78).

[139]M. J. Conterio, N. Sköld, D. J. P. Ellis, I. Farrer, D. A. Ritchie and A. J. Shields, "A quantum dot single photon source driven by resonant electrical injection", Applied Physics Letters **103**, 162108 (2013) (see p. 78).

[140]A. Faraon, I. Fushman, D. Englund, N. Stoltz, P. Petroff and J. Vučković, "Dipole induced transparency in waveguide coupled photonic crystal cavities", Optics express **16**, 12154–12162 (2008) (see pp. 78, 100).

[141]N. Somaschi, V. Giesz, L. De Santis, J. C. Loredo, M. P. Almeida, G. Hornecker, S. L. Portalupi, T. Grange, C. Antón, J. Demory, C. Gómez, I. Sagnes, N. D. Lanzillotti-Kimura, A. Lemaítre, A. Auffeves, A. G. White, L. Lanco and P. Senellart, "Near-optimal single-photon sources in the solid state", Nature Photonics **10**, 340–345 (2016) (see p. 83).

[142]U. L. Andersen and T. C. Ralph, "High-Fidelity Teleportation of Continuous-Variable Quantum States Using Delocalized Single Photons", Physical Review Letters **111** (2013) 10.1103/PhysRevLett.111.050504 (see p. 93).

[143]K. Azuma, K. Tamaki and H.-K. Lo, "All-photonic quantum repeaters", Nature Communications **6**, 6787 (2015) (see p. 93).

[144]L. Yu, C. M. Natarajan, T. Horikiri, C. Langrock, J. S. Pelc, M. G. Tanner, E. Abe, S. Maier, C. Schneider, S. Höfling, M. Kamp, R. H. Hadfield, M. M. Fejer and Y. Yamamoto, "Two-photon interference at telecom wavelengths for time-bin-encoded single photons from quantum-dot spin qubits", Nature Communications **6**, 8955 (2015) (see p. 93).

[145]A. Aspuru-Guzik and P. Walther, "Photonic quantum simulators", Nature Physics **8**, 285–291 (2012) (see p. 93).

[146]Q. Quan, P. B. Deotare and M. Loncar, "Photonic crystal nanobeam cavity strongly coupled to the feeding waveguide", Applied Physics Letters **96**, 39–42 (2010) (see pp. 94, 134).

[147]J. C. Chen, H. a Haus, P. R. Villeneuve and J. D. Joannopoulos, *Optical filters from photonic band gap air bridges*, Vol. 14, 11 (1996), 2575–2580 (see p. 94).

[148]U. Rengstl, M. Schwartz, T. Herzog, F. Hargart, M. Paul, S. L. Portalupi, M. Jetter and P. Michler, "On-chip beamsplitter operation on single photons from quasi-resonantly excited quantum dots embedded in GaAs rib waveguides", Applied Physics Letters **107**, 021101 (2015) (see p. 94).

[149]K. D. Jöns, U. Rengstl, M. Oster, F. Hargart, M. Heldmaier, S. Bounouar, S. M. Ulrich, M. Jetter and P. Michler, "Monolithic on-chip integration of semiconductor waveguides, beamsplitters and single-photon sources", Journal of Physics D: Applied Physics **48**, 085101 (2015) (see p. 94).

[150]B. E. A. Saleh and M. C. Teich, "Fundamentals of photonics", NASA STI/Recon Technical Report A **92** (1991) (see p. 95).

[151]a. J. Bennett, R. B. Patel, C. a. Nicoll, D. a. Ritchie and a. J. Shields, "Interference of dissimilar photon sources", Nature Physics **5**, 715–717 (2009) (see pp. 95, 96, 118).

[152]E. B. Flagg, S. V. Polyakov, T. Thomay and G. S. Solomon, "Dynamics of Nonclassical Light from a Single Solid-State Quantum Emitter", Physical Review Letters **109** (2012) 10.1103/PhysRevLett.109.163601 (see p. 106).

[153]P. Gold, A. Thoma, S. Maier, S. Reitzenstein, C. Schneider, S. Höfling and M. Kamp, "Two-photon interference from remote quantum dots with inhomogeneously broadened linewidths", Physical Review B **89** (2014) 10.1103/PhysRevB.89.035313 (see pp. 106, 118).

[154]X. Liu, H. Kumano, H. Nakajima, S. Odashima, T. Asano, T. Kuroda and I. Suemune, "Two-photon interference and coherent control of single InAs quantum dot emissions in an Ag-embedded structure", Journal of Applied Physics **116**, 043103 (2014) (see p. 106).

[155]T. Huber, A. Predojević, D. Föger, G. Solomon and G. Weihs, "Reach of Environmental Influences on the Indistinguishability of Single Photons from Quantum Dots", arXiv preprint arXiv:1507.07404 (2015) (see p. 106).

[156]E. B. Flagg, A. Muller, S. V. Polyakov, A. Ling, A. Migdall and G. S. Solomon, "Interference of Single Photons from Two Separate Semiconductor Quantum Dots", Physical Review Letters **104**, 137401 (2010) (see p. 118).

[157]R. H. Hadfield, "Single-photon detectors for optical quantum information applications", Nature photonics **3**, 696–705 (2009) (see p. 133).

[158]M. G. Tanner, C. M. Natarajan, V. K. Pottapenjara, J. A. O'Connor, R. J. Warburton, R. H. Hadfield, B. Baek, S. Nam, S. N. Dorenbos, E. B. Ureña, T. Zijlstra, T. M. Klapwijk and V. Zwiller, "Enhanced telecom wavelength single-photon detection with NbTiN superconducting nanowires on oxidized silicon", Applied Physics Letters **96**, 221109 (2010) (see p. 133).

[159]C. M. Natarajan, M. G. Tanner and R. H. Hadfield, "Superconducting nanowire single-photon detectors: physics and applications", Superconductor Science and Technology **25**, 063001 (2012) (see p. 133).

[160]G. Reithmaier, S. Lichtmannecker, T. Reichert, P. Hasch, K. Müller, M. Bichler, R. Gross and J. J. Finley, "On-chip time resolved detection of quantum dot emission using integrated superconducting single photon detectors", Scientific Reports **3** (2013) 10.1038/srep01901 (see p. 133).

[161]G. Reithmaier, M. Kaniber, F. Flassig, S. Lichtmannecker, K. Müller, A. Andrejew, J. Vučković, R. Gross and J. J. Finley, "On-Chip Generation, Routing, and Detection of Resonance Fluorescence", Nano Letters **15**, 5208–5213 (2015) (see p. 133).

[162]J. S. Foresi, P. R. Villeneuve, J. Ferrera, E. R. Thoen, G. Steinmeyer, S. Fan, J. D. Joannopoulos, L. C. Kimerling, H. I. Smith and E. P. Ippen, "Photonic-bandgap microcavities in optical waveguides", Nature **390**, 143–145 (1997) (see p. 134).

[163]Q. Quan and M. Loncar, "Deterministic design of wavelength scale, ultra-high Q photonic crystal nanobeam cavities", Optics express **19**, 18529–18542 (2011) (see p. 134).

[164]P. B. Deotare, M. W. McCutcheon, I. W. Frank, M. Khan and M. Lončar, "Coupled photonic crystal nanobeam cavities", Applied Physics Letters **95**, 031102 (2009) (see p. 134).

[165]X. Chew, G. Zhou, F. S. Chau, J. Deng, X. Tang and Y. C. Loke, "Dynamic tuning of an optical resonator through MEMS-driven coupled photonic crystal nanocavities", Optics letters **35**, 2517–2519 (2010) (see p. 134).

[166]N. Somaschi, V. Giesz, L. De Santis, J. C. Loredo, M. P. Almeida, G. Hornecker, S. L. Portalupi, T. Grange, C. Anton, J. Demory et al., "Near optimal single photon sources in the solid state", arXiv preprint arXiv:1510.06499 (2015) (see p. 135).

[167]V. Giesz, N. Somaschi, G. Hornecker, T. Grange, B. Reznychenko, L. De Santis, J. Demory, C. Gomez, I. Sagnes, A. Lemaitre et al., "Coherent control of a solid-state quantum bit with few-photon pulses", arXiv preprint arXiv:1512.04725 (2015) (see p. 135).